University of Alberta

AB INITIO SEMICLASSICAL INITIAL VALUE REPRESENTATION: DEVELOPMENT OF NEW METHODS

by

Stephanie Yuen Yee Wong

A thesis submitted to the Faculty of Graduate Studies and Research
in partial fulfillment of the requirements for the degree of

Doctor of Philosophy

Department of Chemistry

Fall 2013
Edmonton, Alberta

Abstract

Between the world of classical and quantum mechanics there lies a region where both are used to provide an accurate (quantum) but computationally tractable (classical) description of motion: semiclassical mechanics. The heart of semiclassical theory is the use of the classical path (or, alternatively, the classical trajectory), in a way to elucidate quantum mechanical properties. At the heart of this theory is the semiclassical expression of the quantum mechanical propagator: $e^{-i\hat{H}t/\hbar}$. By reexpressing the propagator in semiclassical form (specifically, the Herman-Kluk initial value representation), we are able to use classical trajectories to determine the vibrational energies of molecules. We first develop the software tools for *ab initio* molecular dynamics in MMTK. In the process of doing so, we have examined the ground and excited state dynamics of the methyl hypochlorite CH_3OCl molecule. Vertical excitation energies and transition dipole moments are calculated at the complete active space self-consistent field (CASSCF)/6-31+G(d) level of theory. With these proven tools, the semiclassical initial value representation (SC-IVR) method for the calculation of vibrational state energies is implemented into this framework. This is the main focus of the thesis. A thorough analysis of the vibrational energies for some of the fundamental, overtone and combination modes of H_2CO is completed. Then, the time-averaged variant of SC-IVR is implemented on the same molecular system. Through this study, we have discovered many caveats of SC-IVR calculations which we discuss. We have shown that *ab initio* SC-IVR is a useful method to calculate vibrational energies and that its values approach that of quantum mechanical meth-

ods such as vibrational self-consistent field (VSCF) and vibrational configuration interaction (VCI).

Acknowledgements

I would like to thank all the friends and family who have supported me throughout my studies. Your camaraderie, friendship and scientific discussions are greatly appreciated. Much thanks to Bilkiss Issack, whom I am following the footsteps after, who provided me with tremendous guidance at the start of my PhD. Thanks to José-Luis Carreón Macedo who worked with me on this project during its infancy. I would also like to thank the other members of the Brown Group, especially Ryan Zaari, who as my contemporary, went through this graduate school experience alongside me. Of course I must thank my supervisors, Alex Brown and Pierre-Nicholas Roy. P.-N.'s enthusiasm for his work is what led me to research in this field. Alex has always been a constant source of supervisory support. I am indebted to my friends who have kept my optimism strong through these past few years.

AB, PNR and SYYW thank the Natural Sciences and Engineering Research Council of Canada (NSERC) and the University of Alberta for financial support and the Canadian Foundation for Innovation for funding of computational resources. SYYW acknowledges the support of NSERC through the award of an NSERC Canada Graduate Scholarship. AB thanks Chen Liang for performing preliminary calculations for CH_3OCl. This research has been (partially) enabled by the use of computing resources provided by WestGrid and Compute/Calcul Canada. Contributions by DMB was partly supported by a grant ("SFB-569/TP-N1") from the Deutsche Forschungsgemeinschaft (DFG).

Table of Contents

List of Tables

List of Figures

List of Symbols

$\mathbf{A}$	*solution of differential Riccati equation*
a	*acceleration*
α	*Hessian eigenvalue matrix*
C	*survival amplitude (auto-correlation function)*
$\hat{E}, \hat{C}, \hat{\sigma}$	*symmetry operators*
E	*total energy*
E_{ij}	*transition energy*
e	*charge of electron*
ϵ_0	*permittivity of vacuum*
$\mathbf{F}$	*force constant matrix*
F	*force*
f	*oscillator strength*
g	*coherent state (or atomic gradient)*
γ	*coherent-state width*
$\hat{H}$	*Hamiltonian operator*
$\hbar$	*reduced Planck constant*
I	*intensity*
i	*imaginary unit*
$\hat{K}$	*propagator (quantum time-evolution operator)*
K	*kinetic energy*
k	*spring constant*
k_B	*Boltzmann constant*
L	*Hessian eigenvector matrix*

$\mathcal{L}$	*Lagrangian*
λ	*de Broglie wavelength*
m	*mass*
μ	*transition dipole moment (or reduced mass)*
ν	*vibrational mode*
ω	*angular frequency*
p	*momentum (or mass-weighted momentum)*
Φ	*wavefunction*
φ	*basis function*
Ψ	*general wavefunction*
Ψ_{ref}	*reference wavefunction*
Q	*normal mode coordinates*
q	*position (or mass-weighted position or curvilinear coordinates)*
$\tilde{R}$	*Hamilton principal function*
$R_{\mathbf{p}_0,\mathbf{q}_0,t}$	*Herman-Kluk prefactor*
r, R	*position (or bond length)*
S	*classical action*
σ	*absorption cross section*
T	*length of trajectory, temperature*
T_{corr}	*correlation time*
t	*time*
τ	*dihedral angle*
θ	*bond angle*
ϑ	*mean-field potential*
V	*electronic potential*
v	*velocity*
W	*window function*
x, y, z	*Cartesian coordinates*
Z	*nuclear charge*

List of Abbreviations

2MR-QFF	*Two-Mode Coupling Representation – Quartic Force Field*
AIMD	*Ab initio Molecular Dynamics*
AMBER	*Assisted Model Building with Energy Refinement*
CAS	*Complete Active Space*
CASSCF	*Complete Active Space Self Consistent Field*
CCSD	*Coupled Cluster Singles and Doubles*
CCSD(T)	*Coupled Cluster Singles and Doubles with Perturbative Triples*
CCSDT	*Coupled Cluster Singles, Doubles and Triples*
cc-VSCF	*Correlation Corrected Vibrational Self-Consistent Field*
CHARMM	*Chemistry at HARvard Molecular Mechanics*
CISD	*Configuration Interaction Singles and Doubles*
CISDT	*Configuration Interaction Singles, Doubles and Triples*
DFT	*Density Functional Theory*
DL_POLY	*Daresbury Laboratory [Polymer] Package*
DMC	*Diffusion Monte Carlo*
FB-IVR	*Forward-Backward Initial Value Representation*
FT	*Fourier Transform*
GAMESS	*General Atomic and Molecular Electronic Structure System*
GROMACS	*GROningen MAchine for Chemical Simulations*
HF	*Hartree-Fock*
HK	*Herman-Kluk*
HO	*Harmonic Oscillator*
IR	*Infrared*
IVR	*Initial Value Representation*
MCTDH	*Multiconfiguration Time Dependent Hartree*
MD	*Molecular Dynamics*
MMTK	*Molecular Modelling Toolkit*
MO	*Molecular Orbital*

MP2	*2nd order Møller-Plesset perturbation theory*
MRCI	*Multireference Configuration Interaction*
NVE	*[Constant] Number, Volume, Energy*
NVT	*[Constant] Number, Volume, Temperature*
PES	*Potential Energy Surface*
PIMC	*Path Integral Monte Carlo*
PIMD	*Path Integral Molecular Dynamics*
QMC	*Quantum Monte Carlo*
QM/MM	*Quantum Mechanics/Molecular Mechanics*
RPMD	*Ring Polymer Molecular Dynamics*
SA-CASSCF	*State-Averaged Complete Active Space Self Consistent Field*
SC-IVR	*Semiclassical Initial Value Representation*
TA	*Time Averaged*
TIP4P	*Transferable Intermolecular Potential 4 Point*
TISE	*Time-Independent Schrödinger Equation*
VCI	*Vibrational Configuration Interaction*
VCIPSI	*Vibrational Configuration Interaction with Perturbation Selected Interactions – Second Order Perturbation*
VMC	*Variational Monte Carlo*
VSCF	*Vibrational Self-Consistent Field*
WKB	*Wentzel-Kramers-Brillouin*
ZPE	*Zero Point Energy*

Chapter 1

Introduction

1.1 The Big Picture

Since the discovery of the laws of motion by the famed polymath Isaac Newton in the 17^{th} century, humans have been able to use classical mechanics to transform all facets of life. From the development of the tallest buildings and amazingly-complex machines and the mathematical foundation of celestial mechanics, to the launch of a moonbound rocket, classical mechanics had been able to describe almost every then-evident problem. However, when scientists began to probe nature at the atomic and molecular level, including electromagnetic radiation, evidence arose that, in these regimes, classical mechanics breaks down. One of the most famous of these discoveries is the "ultraviolet catastrophe", which results from the failure of the Rayleigh-Jeans Law to describe blackbody radiation at short wavelengths [2, 3]. So, too, was the explanation of the photoelectric effect [4] which demonstrated that light was quantized in what is called a photon. Quantization is a fundamental principle in quantum but not classical physics. Through macroscopic eyes, the world is a continuum, but when one zooms into the microscopic regime, the energy spectrum reveals its multitude of "states". The existing laws were ineffectual at explaining these phenomena. Rapid work in the early 20^{th} century led to the new scientific field of quantum mechanics, whose most widely used and known equation is the

time-independent Schrödinger equation:

$$\hat{H}\Psi = E\Psi. \tag{1.1}$$

The Hamiltonian operator, $\hat{H}$, when acting upon the wavefunction Ψ and giving $E\Psi$, creates an eigenvalue equation. The wavefunction has the property that when acted upon by $\hat{H}$ gives itself multiplied by a scalar. This scalar is the total energy of the system the wavefunction represents. The time-independent Schrödinger equation can be used when $\hat{H}$ is time-independent and when one is not interested in the time-dependence of the wavefunction (it is a phase factor) and only interested in stationary states. When the wavefunction is explicitly time-*dependent* (and possibly the Hamiltonian), the Schrödinger equations becomes

$$i\hbar\frac{\partial}{\partial t}\Psi = \hat{H}\Psi. \tag{1.2}$$

The wavefunction, Ψ, can describe all properties of a system. Using the time-independent form, $\hat{H}$ can be explicitly expressed in Cartesian coordinates for N particles as

$$\hat{H} = -\frac{\hbar^2}{2}\sum_{n=1}^{N}\frac{1}{m_n}\left(\frac{\partial^2}{\partial x_n^2}+\frac{\partial^2}{\partial y_n^2}+\frac{\partial^2}{\partial z_n^2}\right)+V(\mathbf{r}_1,\mathbf{r}_2,\cdots,\mathbf{r}_N), \tag{1.3}$$

where $(\mathbf{r}_1,\mathbf{r}_2,\cdots,\mathbf{r}_N)=(x_1,y_1,z_1,x_2,y_2,z_2,\cdots,x_N,y_N,z_N)$, m_n is the mass of particle n and V is the global potential describing the interaction of all particles. This is a multidimensional second-order partial differential equation. Most often, this equation (or set of equations, as we are realistically dealing with multiple particles and dimensions) is expressed in matrix notation. The Hamiltonian, which is an $N \times N$ matrix, where N is the number of degrees of freedom in the system of interest, requires a diagonalization of order N^3 .

To this point, we have only referred to systems and "particles". As this is chemistry, we would like to treat a system of molecules. Therefore, Ψ is a wavefunction that determines all properties of the chemical system. Solution of the Schrödinger

equation is computationally non-trivial and so, much of theoretical/computational chemistry and molecular physics research has been to find alternate ways to solve this equation approximately. The contents of this thesis cover a specific way to solve this type of equation.

1.2 Quantum Mechanical Simulations

The Schrödinger equation can be specifically applied to a chemical system. A full quantum mechanical description of a molecular system involves all the degrees of freedom of the nuclei and electrons. Each nucleus is in motion and surrounding it is a varying electronic distribution. Even before considering the form of the Hamiltonian, the number of degrees of freedom is already overwhelming. There are $3N$ nuclear degrees of freedom and they are all coupled with one another. In general, they are not separable. One of the first approximations most quantum mechanical simulations begin with is the Born-Oppenheimer approximation. The justification behind it is simple. The masses of the nuclei in a molecule are much larger than those of the electrons. As such, the electrons move much faster than the nuclei. To a very good approximation, the nuclei are stationary with respect to the motion of the electrons. The advantage of this approximation is that the nuclear and electronic problems can be separated. The general Hamiltonian can be expressed as a sum of the electronic (first 3 terms) and nuclear (last 2 terms) Hamiltonians:

$$\begin{aligned}\hat{H} &= \hat{H}_{\text{el}} + \hat{H}_{\text{N}} \\ &= -\frac{\hbar^2}{2m_e}\sum_i \nabla_i^2 + \frac{e^2}{4\pi\varepsilon_0}\sum_{i<j}\frac{1}{|r_j - r_i|} - \frac{e}{4\pi\varepsilon_0}\sum_{i,A}\frac{Z_A}{|r_i - R_A|} \\ &- \sum_A \frac{\hbar^2}{2m_A}\nabla_A^2 + \frac{1}{4\pi\varepsilon_0}\sum_{A<B}\frac{Z_A Z_B}{|R_B - R_A|},\end{aligned} \tag{1.4}$$

where m_e and r_i are electronic mass and positions, respectively, m_A and R_A are nuclear masses and positions, respectively, ε_0 is the permittivity of vacuum, e is the charge of an electron and Z_A is the charge of the nucleus A. The first term

represents the kinetic energy of the electrons, the second term the two-body potential interactions between the electrons, the third term the two-body interactions between the nuclei and electrons, the fourth term the kinetic energy of the nuclei, and the final term the two-body potential interactions between the nuclei. When the nuclei are fixed by assuming the Born-Oppenheimer approximation, the nuclear kinetic term can be ignored and the *electronic* Schrödinger equation can be solved. The nuclear geometry coordinates are now parameters $\vec{R}$. The electronic coordinates, $\vec{r}$, are the only variables. Then, the electronic Schrödinger equation is

$$\hat{H}_{\text{el}}\psi(\vec{r};R) = E_{\text{el}}\psi(\vec{r};\vec{R}), \tag{1.5}$$

where

$$\hat{H}_{\text{el}} = -\frac{\hbar^2}{2m_e}\sum_i\left(\frac{\partial^2}{\partial x_i^2}+\frac{\partial^2}{\partial y_i^2}+\frac{\partial^2}{\partial z_i^2}\right)+V(\{x,y,z\};\vec{R}). \tag{1.6}$$

The electronic Schrödinger equation can be solved separately, and the study of quantum chemistry and electronic structure methods is an entire field in its own right [5, 6]. In a strict "electronic structure program", the positions of the atoms are fixed at a given geometry. There, the electronic Schrödinger equation is solved through various quantum mechanical electronic structure methods (see Appendix B). For instance, the determination of potential energies V for a set of geometries produces a *potential energy surface* (PES). The forces on a fixed configuration of nuclei are governed by this potential field. Provided that the molecular system stays on a single adiabatic electronic quantum state, the Born-Oppenheimer approximation is valid. That is, we assume there is no change in electronic state.

With the electronic solution being (hopefully) obtainable, one can now focus on the nuclear problem. In most cases, a brute force exact solution of the nuclear Schrödinger equation is impractical. While classical molecular methods can be used, especially for more massive particles (beyond He), in some circumstances, there is a necessity for developing *approximate quantum* methods. Despite fundamental

approximations like the Born-Oppenheimer one, almost all problems need to be solved numerically. The Schrödinger equation is not separable. Dimensionality soon becomes an issue because of the diagonalization of the Hamiltonian matrix which is required to solve for the wavefunction. In some situations, expedient diagonalization methods [7] may be used; otherwise, one may rely on other quantum mechanical formulations [8, 9] such as path integrals [10], semiclassical mechanics [11] or quasi-classical mechanics [12].

1.3 Electronic Structure Methods

In Eq. 1.5, the electronic wavefunction was introduced. To describe the electronic distribution in a molecular system, quantum mechanics must be used. Quantum effects dominate *all* cases due to the presence of electrons and their large de Broglie wavelength. The myriad of electronic structure methods used in computational chemistry today span the whole gamut of computational accuracy [5, 6, 13].

Commonly-used are methods such as Hartree-Fock (HF) [14] and Density Functional Theory (DFT) [15, 16]. For expedient and approximate ground state calculations, these are often sufficient. DFT is widely used for many-atom systems and is a satisfactory choice for including electron correlation with advantages over some post-HF methods. High-level electronic structure methods are abundant and, in theory, the exact answer can be approached, although the timescale (infinite) for such a simulation is obviously prohibitive. Among these methods are the perturbation theories (Møller-Plesset second-order perturbation theory [MP2]), configuration interaction (CI singles and doubles [CISD], CI singles, doubles and triples [CISDT]), multireference (complete active space [CAS], multi-reference configuration interaction [MRCI]) and coupled-cluster (CC singles, doubles and perturbative triples [CCSD(T)], CC singles, doubles and triples [CCSDT]) methods. These have all been well-documented in many textbooks [5, 6, 13]. Numerous quantum chem-

istry programs have been developed to calculate energies, spectroscopic values and thermodynamic properties. These programs [17–20] provide the ability to conduct many electronic structure calculations in a somewhat black box fashion, although substantial knowledge of the models/implementation is required for an educated interpretation of most results.

1.4 Quantum Dynamics

Assuming the electronic Schrödinger equation is solved with the tools mentioned above such that the PES (or single *ab initio* points) can be obtained, the focus turns from the static problem with fixed nuclei to nuclear motion. Treatment of the nuclear problem may be classical or quantum mechanical, depending on the system at hand and the dynamical accuracy required. For phenomena that are a result of quantum mechanical effects, such as those involving light atoms (e.g., proton transfer), quantum mechanical treatments are needed. Of course, solution of the full quantum nuclear Schrödinger equation requires solving a multidimensional partial differential equation. While brute force methods exist, there are many other approaches. Whole fields of study have been developed [21,22] to solve this equation. Some are techniques to simplify brute force methods, while others reformulate the original problem.

Richard Feynman developed an exact method of quantum dynamics through classical intuition. He used the concept of polymer beads to represent delocalized atoms, which he called the *path integral* [10]. In this sense, it preserves the uncertainty and delocalization of quantum particles, yet the mathematical implementation through the use of beads is classical. Many flavours of path integrals have been implemented to calculate equilibrium and dynamical properties of molecular systems. The guiding principle is the expression of the partition function in terms of a division of time slices (or beads). The matrix element of the quantum mechanical propagator,

$\left\langle x' \left| e^{-i\hat{H}t/\hbar} \right| x \right\rangle$ is segmented into time slices so that instead of a propagation from x' to x, the propagator is a sum of short-time propagators from $x' \rightarrow x_1$, $x_1 \rightarrow x_2$, ..., $x_{N-1} \rightarrow x_N$, $x_N \rightarrow x$ [22]. The short-time propagator is desired because then, the propagator may be simplified through Trotter factorization, whereby the kinetic and potential terms in the Hamiltonian may separated and factorized.

Quantum Monte Carlo (QMC) techniques [23] have been widely used in molecular simulations. With a scalability on the order of N^3 or less (where N is the number of degrees of freedom) and the intrinsic ability for parallelization, many advances and flavours of QMC have been developed. Variational Monte Carlo (VMC) is based on the variational principle. The expectation value of the Hamiltonian is variationally-obtained after rewriting it in terms of the probability density function, which is randomly sampled. Like any variational method, the choice of trial wavefunction has a large effect on the convergence of the simulation. Another QMC method is Diffusion Monte Carlo (DMC) [24]. This exploits the similarity between the diffusion equation/branching process with the kinetic and potential terms in the Hamiltonian. It is highly successful in calculating ground vibrational states and properties of anharmonic systems and weakly-bound complexes [25]. To go beyond the ground state limitation and calculate excited states, there are other expanded approaches such as fixed-node DMC [26].

There are also other approaches to solving the time-dependent Schrödinger equation; for instance, the Multiconfiguration Time Dependent Hartree (MCTDH) [27] method which often uses an approximate Hamiltonian. It is a variational-type method that expresses the wavefunction in terms of products of single particle functions. MCTDH is computationally efficient for systems from about 4-12 degrees of freedom, although has been used for much larger model problems. The primary limitation, though, is the need to express the Hamiltonian in product form; so, in particular, there needs to be a potential expressible in such a form.

1.5 Why not Classical?

Classical simulations can be used to model macroscopic systems, and to a lesser extent, microscopic systems. The dynamics of a classical system follows the Newtonian equations of motion. Each "particle" is localized in coordinate space and momentum. Being very practical and intuitive, it would be desired to use ideas and methods from classical mechanics to solve the quantum problem. It is possible to bring in some of its concepts (and even equations). The reason is due to the the correspondence principle. In the limit of large quantum numbers, quantum mechanics reduces to classical mechanics. In fact, assuming the limit, Hamilton's principal function (described later) [28, 29] will give rise to the Hamilton-Jacobi equation, which is just another formulation of classical mechanics. So, Newtonian mechanics can, in part, describe well enough some aspects of molecular motion.

The study of molecular motion with classical mechanics is called classical *molecular dynamics* (MD). Its central equation is Newton's Second Law:

$$F = ma, \tag{1.7}$$

which is the famous equation (in 1-D) stating force is proportional to mass and acceleration. Knowing that the acceleration can be expressed as a derivative of potential energy V with respect to position x:

$$a = -\frac{dV}{dx}, \tag{1.8}$$

the equation implies that the acceleration (or force) placed on the nucleus is caused by the *electronic* potential acting on it. That is, the slope on the potential energy surface corresponding to the nuclear coordinates gives the acceleration on the nucleus. The solution of the position and momentum of point particles (or single atoms) can be analytically solved with simple potentials. For more complex (realistic) problems, the solution of these integrals requires using numerical integrators, which

are adaptations of the standard kinematic equations. One of the common integrators is Velocity-Verlet [30]:

$$\begin{aligned} x(t+\Delta t) &= x(t) + v(t)\Delta t + \frac{1}{2}a(t)\Delta t^2 \\ v(t+\Delta t) &= v(t) + \frac{a(t)+a(t+\Delta t)}{2}\Delta t. \end{aligned} \tag{1.9}$$

At time t or an infinitesimal time later $t + \Delta t$, there is a corresponding position x, velocity (momentum) v ($p = mv$) and acceleration a for each Cartesian degree of freedom ($3N$). The acceleration is obtained from the potential as described above while the continual application of this set of equations for every *timestep* will produce a series of positions x and momenta p, forming a MD *trajectory* (momentum is the more practical variable to use in this context). The complexity or time-constraint of the otherwise simple calculation above is the determination of the electronic potential for the acceleration. Once the potential is known – including effects such as periodic boundary conditions (Ewald summation) or solvent effects – the rest of the classical dynamics is straightforward. The need for an accurate PES that can be computed in a reasonable amount of time is the bottleneck for a classical simulation. Therefore, crafting feasible *classical* molecular dynamics simulations usually involves finding ways to calculate the *quantum* electronic forces.

Model analytic potential energy surfaces are abundant and in fact, many molecular dynamics programs (AMBER [31], GROMACS [32], DL_POLY [33]) take advantage of these ready-made surfaces (TIP4P [34], AMBER, Lennard-Jones, CHARMM [35], Morse). A substantial number of potentials are geared towards biological or organic molecules. Also, empirically-derived parameters are limited in scope. While the availability of potentials is growing, in many cases, a "pre-generated" potential energy surface may not be desirable. These include reactions and processes such as non-adiabatic surface hopping and avoided crossings that are not dealt with well on a single energy surface. It is desirable to use an *ab initio* approach, where the potential for the dynamics algorithm is computed "on-the-fly".

This means that *ab initio* points are calculated as needed. No interpolation or approximation from an existing grid (PES) is used. Then, the dynamics may respond to changes in the electronic Hamiltonian in an immediate fashion.

1.5.1 Semiclassical dynamics - the best of both worlds

As alluded to earlier in Sec. 1.5, quantum mechanics has a classical limit. Since the solution of the quantum mechanical wavefunction is "difficult" while classical mechanics is "easy", it would be wise to merge the two to obtain a *semi*classical theory. Then one may conduct quantum dynamics (or at least approach its results) while using classical tools. The heart of semiclassical theory is the use of the classical path (or, alternatively, classical trajectory), from which quantum mechanics can be developed. Rather than dealing with a delocalized wavefunction from the start, semiclassical mechanics begins with the localized classical trajectory. These are computed in classical Newtonian fashion. Then, through valid approximations made to the *quantum mechanical propagator* $e^{-i\hat{H}t/\hbar}$, this *semi*classical propagator readily receives as "inputs" these classical trajectories. The quantum propagator originates from Eq. 1.2, where the general solution is: $\Psi(t) = e^{-i\hat{H}t/\hbar}\Psi(0)$. Therefore, the propagator (also called the time-evolution operator) gives the current state of a system initially in an original state (in this case, $t = 0$). Conceptually, the complexity greatly diminishes because of the localized picture. This is our choice of methodology and the subsequent chapters of this thesis will develop the tools and explore the aspects of a particular type of semiclassical dynamics.

This thesis endeavours to develop tools based on the semiclassical initial variable representation technique to provide accurate stationary and dynamical information of chemical systems, with the goal of boosting the arsenal of quantum dynamics methodologies. Since the specific purpose of the present research is to develop a *methodology* of semiclassical vibrational state calculations rather than reproducing

exact experimental results, the electronic structure methods we use are relatively low-level and the results are only to be compared to other computational results calculated at the same level of theory. The research begins at the classical mechanics stage, developing the specific tools to do our own *ab initio* molecular dynamics simulations. Then, the semiclassical aspect is introduced. Chapter 2 describes all the theory behind the classical and semiclassical simulations. Chapter 3 is about the development of *ab initio* molecular dynamics simulations tools and and applications to the ground and excited dynamics simulations of methyl hypochlorite. Chapter 4 describes the vibrational state energy calculations of formaldehyde with the semiclassical initial value representation method and its comparison to some other techniques. This study is the main aspect of our research. In Chapter 5, an alternate form of this method (time-averaged SC-IVR) is discussed. The vibrational states of formaldehyde are obtained with this method and are compared to the results in Chapter 4. Chapter 6 contains our conclusions and future outlook.

Chapter 2

Theory

The first step in approximating full quantum mechanics is to choose the method of approach. One such method is the semiclassical approximation [36]. The premise of semiclassical theory is to reintroduce localized position and momentum (the concept of a particle) in order to use molecular information obtained classically, namely the classical path (or trajectory). There are a handful of derivations [21, 28, 29] that lead to the same semiclassical expressions. They depend on how classical mechanics is perceived. Classical mechanics may be viewed as its own independent theory (after all, it was discovered first and is essentially correct for macroscopic objects) with an isomorphic quantum equivalent; or, one can consider classical mechanics as just the classical limit of quantum mechanics, with its equations simply resulting from approximations to the quantum ones. Either way, there has to be a criterion that links the two theories [28]. The "classical limit" may be the large quantum number, the Planck constant approaching zero ($\hbar$ does not exist in classical mechanics), the de Broglie wavelength (a classical macroscopic object has a very small wavelength so that it is for all intents and purposes a particle), etc. Semiclassical expressions have been derived using all these criteria and it would be a large (and unnecessary) undertaking to discuss here [21, 28, 29]. Therefore, below will be a brief outline of the basic assumptions of semiclassical theory as it pertains to this thesis.

2.1 The Semiclassical Wavefunction

The Wentzel-Kramers-Brillouin (WKB) approximation is a particularly useful method to solve partial differential equations, and its use in deriving the WKB semiclassical wavefunction will be shown to provide a basis for the later derivation of the semiclassical propagator. We begin with the (1-D) time-independent Schrödinger equation (TISE):

$$-\frac{\hbar^2}{2m}\frac{d^2\Psi(q)}{dq^2} + V(q)\Psi(q) = E\Psi(q). \tag{2.1}$$

At present, q is a one-dimensional position coordinate. It will be generalized later to many dimensions. In terms of wave mechanics, the TISE may be expressed as

$$\hbar^2\frac{d^2\Psi(q)}{dq^2} + p^2(q)\Psi(q) = 0, \tag{2.2}$$

where

$$p(q) = \sqrt{2m(E - V(q))}, \tag{2.3}$$

which comes from the 1-D particle moving in a potential $V(q)$. It is important to note that it is assumed that the potential V is slowly-varying and the de Broglie wavelength is small.

An ansatz to the differential equation in Eq. 2.2 is then

$$\Psi = A(q)e^{\frac{i}{\hbar}S(q)}. \tag{2.4}$$

A and S are real-valued functions and are the amplitude and phase of the wavefunction, respectively. This polar form of the wavefunction is very useful. The WKB approximation is applied in the following subset of partial differential equations. Taking the general wavefunction above (Eq. 2.4) and expanding the exponential part in powers of $\hbar$:

$$S(q) = S_0(q) + \hbar S_1(q) + \hbar^2 S_2(q) + \cdots, \tag{2.5}$$

we notice that since $\hbar$ is small, terms involving higher powers of $\hbar$ are negligible. In fact, in the limit of classical mechanics, $\hbar$ approaches zero. Therefore, the terms involving higher powers of $\hbar$ can be neglected. Inserting this expansion into Eq. 2.2 and equating powers of $\hbar$ gives

$$\frac{d^2S_0(q)}{dq^2} + p^2 = 0 \tag{2.6a}$$

and

$$-2\left(\frac{dS_0(q)}{dq}\right)\left(\frac{dS_1(q)}{dq}\right) \pm i\left(\frac{d^2S_0(q)}{dq^2}\right) = 0. \tag{2.6b}$$

Rearranging, this gives the equation for S_0 and S_1:

$$S_0(q) = \pm \int [2m(E - V(q))]^{1/2} dq \tag{2.7a}$$

$$S_1(q) = \frac{i}{4}\ln[2m(E - V(q))]. \tag{2.7b}$$

The use of the assumption that the potential is slowly-varying and that the de Broglie wavelength ($\lambda = 2\pi\hbar/p$) is small can be more easily exemplified with an alternate, but equivalent derivation. Inserting Eq. 2.4 into Eq. 2.2, we get

$$\left(Ae^{\frac{i}{\hbar}S}\right)'' + k^2 Ae^{\frac{i}{\hbar}S} = 0, \tag{2.8}$$

where $k = p/\hbar$. If the real and imaginary parts are equated separately, the following equations emerge:

$$(S')^2 = p^2 + \hbar^2\frac{A''}{A} \tag{2.9}$$

and

$$S''A + 2S'A' = \frac{1}{A}\frac{d}{dq}(S'A^2) = 0. \tag{2.10}$$

The WKB approximation assumes the amplitude A of the wavefunction varies slowly. This means the curvature (A'') is very small. So, assuming the A''/A term vanishes, we end up with:

$$S' = p \tag{2.11}$$

which can be readily integrated to obtain

$$S = \int_{q_1}^{q_2} p(q)\, dq. \tag{2.12}$$

The integration limit is between q_1 and q_2, meaning $S = S(q_1, q_2)$. Eq. 2.10 may be solved by observing that $\frac{d}{dq}(S'A^2) = 0$ and that when integrated,

$$A(q) = \frac{C}{|p(q)|^{\frac{1}{2}}} = \frac{C}{|\sqrt{2m(E - V(q))}|^{\frac{1}{2}}}. \tag{2.13}$$

The resulting time-independent wavefunction is

$$\Psi_{\text{WKB}} = \frac{C}{|\sqrt{2m(E - V(q))}|^{\frac{1}{2}}} e^{\frac{i}{\hbar}S(q)}. \tag{2.14}$$

However, as is well-known, there is a time-dependent component in the full wavefunction (stemming from the time-dependent part of the Schrödinger equation). So, after adding this "phase" component, $e^{-iEt/\hbar}$, the time-dependent WKB wavefunction is

$$\Psi_{\text{WKB}} = \frac{C}{|\sqrt{2m(E - V(q))}|^{\frac{1}{2}}} e^{\frac{i}{\hbar}[S(q) - Et]}. \tag{2.15}$$

Note that a potential problem with Eq. 2.15 is that there is a division by the momentum (see Eq. 2.3), meaning there are discontinuities at the turning points where $p = 0$. Therefore, to have a valid wavefunction at all points, one must use a Fourier transform between position and momentum representations, which adds a phase factor to wavefunction. Provided that the phase is accounted for, the WKB wavefunction serves as a semiclassical approximation to the exact wavefunction.

What is important to remember from this WKB wavefunction is that S is a critical part in the theory. First, we must note the two terms in the exponential in Eq. 2.15: $S(q) - Et$. In cases where the time-dependent wavefunction is used, the $-Et$ term will be in the exponential and so it is customary to incorporate it into S. This means that S is now time-dependent.[1] This more general S will be used from

[1] In fact, $S(q)$ is sometimes called the abbreviated action and $S(q, t)$ the action. Notation for the action is not consistent.

now on in the following derivations. The relevance of S to classical mechanics may be gleaned from the classical Hamilton-Jacobi equation:

$$H + \frac{dS}{dt} = 0. \tag{2.16}$$

The Hamilton-Jacobi equation is just an alternate formulation of classical mechanics and shows how interrelated the equations for classical mechanics and semiclassical mechanics are. $S(q,t)$ is actually the time-integral of the Lagrangian, $\mathcal{L}$, which is just kinetic energy (K) minus the potential energy (V):

$$S = \int p(t)\dot{q}(t) - H(p(t),q(t))\ dt = \int K(p(t)) - V(q)\ dt = \int \mathcal{L}(p(t),q(t))\ dt \tag{2.17}$$

and is related to Hamilton's Principal Function:

$$\tilde{R}(q,q',(t-t')) = S(q,q',E) - E(t-t'). \tag{2.18}$$

2.2 The Semiclassical Propagator

We now go back to quantum mechanics and begin with the definition of the single-particle propagator (quantum time-evolution operator):

$$\hat{K}(t) = e^{-i\hat{H}t/\hbar}. \tag{2.19}$$

This operator, when it acts on a wavefunction, gives the wavefunction at a later time t:

$$|\Psi_f\rangle = e^{-i\hat{H}t/\hbar}\ |\Psi_i\rangle\,. \tag{2.20}$$

The propagator (also called Green's function) determines the time-evolution of a molecular system. It must be expressed in a particular representation (in this instance, the position $\mathbf{q}$). The propagation from configuration $\mathbf{q}_i$ to $\mathbf{q}_f$ in matrix form is

$$K(\mathbf{q}_i,\mathbf{q}_f,t) = \left\langle \mathbf{q}_f|e^{-i\hat{H}t/\hbar}|\mathbf{q}_i \right\rangle. \tag{2.21}$$

The propagator acting on a state Ψ and overlapped with itself generates the wavefunction auto-*correlation* function:

$$C(t) = \left\langle \Psi | e^{-i\hat{H}t/\hbar} | \Psi \right\rangle . \tag{2.22}$$

Eq. 2.22 is called the quantum mechanical survival amplitude (or correlation function[2]). What this equation gives us is the *overlap* of the current state at time t with a *reference* state Ψ (if the Ψs were different, it would give the transition amplitude[3]). In integral form, the survival amplitude may be expressed as a double integral (for each degree of freedom) over the positions of the system (insertion of $\mathbb{1}$'s):

$$C(t) = \int d\mathbf{q}_f \int d\mathbf{q}_i \left\langle \Psi | \mathbf{q}_f \right\rangle \left\langle \mathbf{q}_f | e^{-i\hat{H}t/\hbar} | \mathbf{q}_i \right\rangle \left\langle \mathbf{q}_i | \Psi \right\rangle . \tag{2.23}$$

The integrals are *paths* joining two spacetime points (i, f) [28].[4] If the current wavefunction state (as it traverses along the path in time) has high overlap with Ψ, then the magnitude of the survival amplitude is large. For a fully harmonic system, the survival amplitude will oscillate and be periodic. In an anharmonic system, there will be loss of correlation and the correlation will approach zero at long time.

Under the assumption that the potential of a quantum system is slowly varying (also assumed in the WKB wavefunction derivation discussed in Sec. 2.1), van Vleck [37] proposed and proved that the propagator may be written semiclassically under two assumptions. The wavefunction is assumed to be of the form in Eq. 2.4 and the propagator is of the form

$$K = A^{1/2} \Delta^{1/2} e^{S/ih}, \tag{2.24}$$

[2]Note: We call this the "correlation function", although this is a misnomer. Real correlation functions will be discussed in Future Outlook in Sec. 6.2.

[3]The propagator acting on a state Ψ_i and overlapped by state Ψ_f generates the transition amplitude between the two states.

[4]Equivalently, the transition amplitude would be

$$C_{fi}(t) = \int d\mathbf{q}_f \int d\mathbf{q}_i \left\langle \Psi_f | \mathbf{q}_f \right\rangle \left\langle \mathbf{q}_f | e^{-i\hat{H}t/\hbar} | \mathbf{q}_i \right\rangle \left\langle \mathbf{q}_i | \Psi_i \right\rangle .$$

where A is a constant, S is the classical action and Δ is a functional stemming from the classical Hamilton-Jacobi equation (Eq. 2.16). In a more explicit form,

$$K(\mathbf{q}_0, \mathbf{q}_t, t) = (2\pi i\hbar)^{-3N/2} \sqrt{\det \frac{\partial^2 S}{\partial \mathbf{q}_t \partial \mathbf{q}_0}} e^{\frac{i}{\hbar} S_t}. \tag{2.25}$$

Gutzwiller [38] rederived the propagator above from a Feynman path integral point of view. He noticed, however, that an extra phase term needed to be added to the exponential. The exponential term is oscillatory and thus, when integrated in Eq. 2.23, $C(t)$ only has significant amplitude when S is stationary ($\delta S = 0$). This only happens in the classical limit. The assumption that S is stationary is called the *stationary phase approximation.*[5]

In Eq. 2.23, the survival amplitude is a double integral incorporating *all* paths from configuration i to f. To determine all paths joining them involves a root search (boundary value) problem. In other words, all classical paths that link point i to point f must be found. This "primitive" semiclassical equation can be solved with the use of the stationary phase approximation, but there is a simpler solution without further approximation. Through the works of many including Herman, Heller, Miller and others [39–42], a transformation from the double-ended boundary condition $(\mathbf{q}_i, \mathbf{q}_f)$ in the integral to an initial phase space $(\mathbf{q}_i, \mathbf{p}_i)$ integral eliminates the path search. This new integral leaves the final coordinates ambiguous and requires, rather, the initial conditions. A classical trajectory is constructed this way, as once the initial conditions are specified, the dynamics according to the potential takes it to the final coordinates (see Fig. 2.1). Therefore, Eq. 2.23 may be now written as

$$C(t) = \int d\mathbf{p}_i \int d\mathbf{q}_i \left\langle \Psi | \mathbf{g}_{p_t,q_t} \right\rangle \left\langle \mathbf{g}_{p_t,q_t} | e^{-i\hat{H}t/\hbar} | \mathbf{g}_{p_i,q_i} \right\rangle \left\langle \mathbf{g}_{p_i,q_i} | \Psi \right\rangle. \tag{2.26}$$

[5]This approximation implies that the path (connecting two coordinate points) of a particle is one that yields a stationary value of the action. Classical paths exist only if S is stationary. Similarly, it implies that the *trajectory* that a particle takes is one that has a stationary phase. Its relevance to quantum mechanics is that the trajectories move along "wavefronts" of constant S (time-independent form). Thus, S serves as a "link" between classical and quantum mechanics.

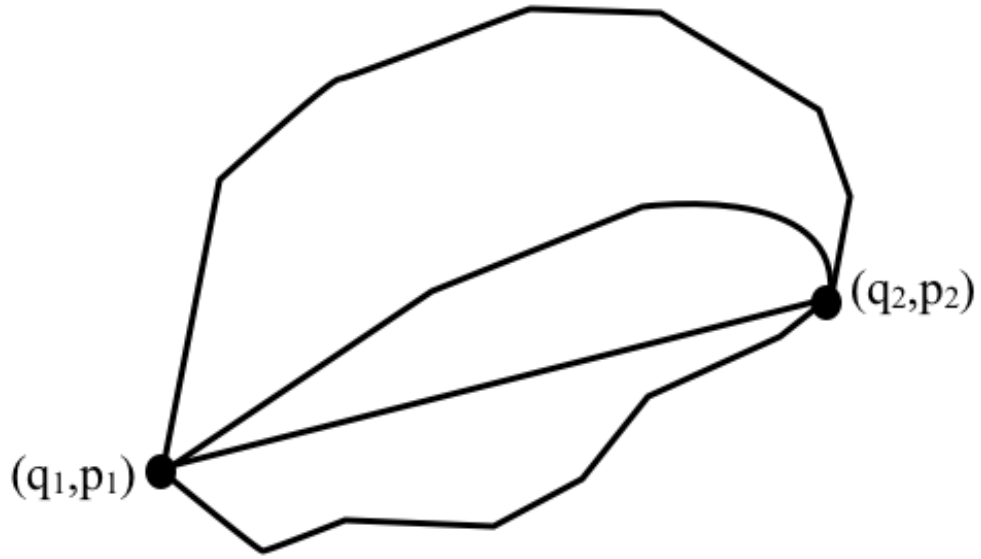

(a)

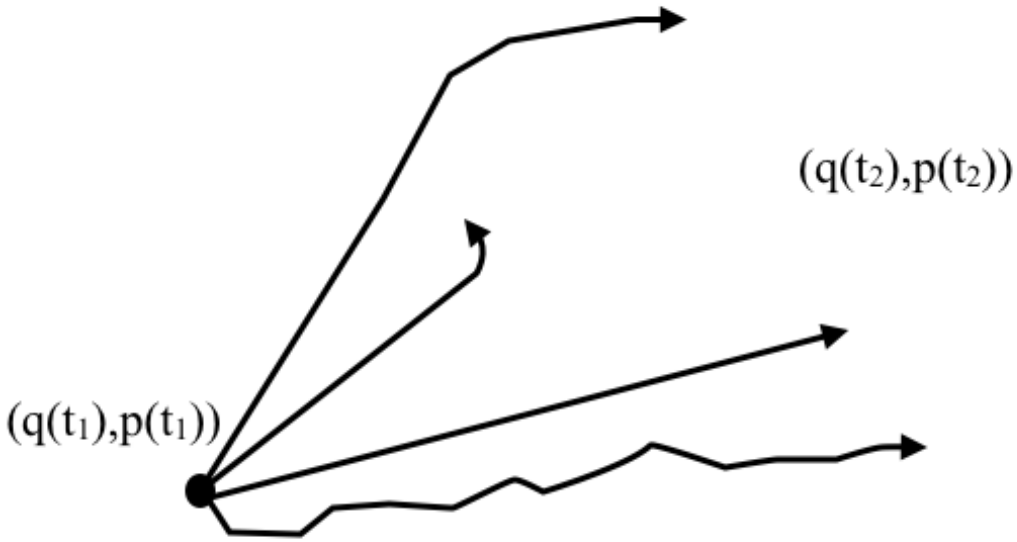

(b)

Figure 2.1: The difference between a path (a) and a trajectory (b).

When using these phase space integrals, it is amenable to use a coherent state representation of the propagator matrix and wavefunction [43, 44]. Coherent states are "hybrid" [45] states between the position and momentum eigenstates and resem-

ble a frozen multidimensional Gaussian wavepacket. They have the property that the centre of the Gaussian evolves according to the classical equations of motion, which makes it easy to implement and conceptually visualize. $|g_{\mathbf{p}_t,\mathbf{q}_t}\rangle$ and $\langle g_{\mathbf{p}_0,\mathbf{q}_0}|$ are coherent state representations of the minimum-uncertainty wavepacket, which is a multivariate Gaussian function of coherent-state width γ [39, 43, 44].

To transform the Hamiltonian operator into a semiclassical form, the quantum propagator can be replaced with the semiclassical Herman-Kluk (HK) propagator [39, 46–48]. Expanding upon the works by van Vleck and others mentioned previously, Herman and Kluk proposed this form of the propagator:

$$e^{-i\hat{H}t/\hbar} = (2\pi\hbar)^{-3N} \int\int d\mathbf{p}_0 d\mathbf{q}_0 R_{\mathbf{p}_0,\mathbf{q}_0,t} e^{iS_{\mathbf{p}_0,\mathbf{q}_0,t}/\hbar} |g_{\mathbf{p}_t,\mathbf{q}_t}\rangle\langle g_{\mathbf{p}_0,\mathbf{q}_0}|. \tag{2.27}$$

The integrals are over the mass-weighted phase space variables, $\mathbf{p}_0$ and $\mathbf{q}_0$, and are determined through Monte Carlo sampling. Since these phase space variables are *initial* conditions, they are so-called *initial value representations* (thus the name SC-*IVR*). Now, similar to the semiclassical WKB wavefunction, the time-dependent classical action (Eq. 2.17) appears in Eq. 2.27. Also, a term $R_{\mathbf{p}_0,\mathbf{q}_0,t}$ manifests itself, called the Herman-Kluk prefactor. The prefactor resolves many of the issues that plagued previous semiclassical propagators (e.g., the root search problem and discontinuities at turning points). The form of the prefactor is

$$R_{\mathbf{p}_0,\mathbf{q}_0,t} = \sqrt{\det\left[\frac{1}{2}\left(\frac{\partial\mathbf{q}_t}{\partial\mathbf{q}_0} + \frac{\partial\mathbf{p}_t}{\partial\mathbf{p}_0} - i\hbar\gamma\frac{\partial\mathbf{q}_t}{\partial\mathbf{p}_0} + \frac{i}{\gamma\hbar}\frac{\partial\mathbf{p}_t}{\partial\mathbf{q}_0}\right)\right]}, \tag{2.28}$$

which is a determinant of monodromy stability matrices, requiring the derivatives of the time-evolved $(\mathbf{p}_t, \mathbf{q}_t)$ variables with respect to the initial variables $(\mathbf{p}_0, \mathbf{q}_0)$. The classical action S, explicitly, is the time-integral of the Lagrangian along the trajectory:

$$S_{\mathbf{p}_0,\mathbf{q}_0,t} = \int_0^t dt' \left(\frac{\mathbf{p}_{t'}^2}{2\mathbf{m}} - V\left(\mathbf{q}_{t'}\right)\right). \tag{2.29}$$

With the propagator now known, adding in the wavefunction results in the initial value representation (IVR) form of the semiclassical survival amplitude:

$$C(t) = (2\pi\hbar)^{-3N} \int\int d\mathbf{p}_0 d\mathbf{q}_0 R_{\mathbf{p}_0,\mathbf{q}_0,t} e^{iS_{\mathbf{p}_0,\mathbf{q}_0,t}/\hbar} \langle \Psi_{\mathrm{ref}} | g_{\mathbf{p}_t,\mathbf{q}_t} \rangle \langle g_{\mathbf{p}_0,\mathbf{q}_0} | \Psi_{\mathrm{ref}} \rangle. \tag{2.30}$$

In the above, the "ref" in Ψ_{ref} is used to clearly denote that this is an arbitrary *reference* state.

Previously, we described the WKB wavefunction (Eq. 2.15). In practice, there are numerous forms [49] of the semiclassical wavepacket possible. These include the above "primitive" form [37], cellular dynamics [41], frozen Gaussians [43], thawed Gaussians [50], etc. The coherent state [51] has been extensively used in SC-IVR applications. In tandem with the HK propagator, which uses the coherent state representation, we represent the wavefunction as a multivariate Gaussian function:

$$\begin{aligned} \langle g_{\mathbf{p},\mathbf{q}} | \Psi_{\mathrm{ref}} \rangle \;=\; & \exp\left[-\frac{1}{4} \left(\mathbf{q}-\mathbf{q}_{\mathrm{ref}}\right)^T \gamma \left(\mathbf{q}-\mathbf{q}_{\mathrm{ref}}\right) \right. \\ & -\frac{1}{4\hbar^2} \left(\mathbf{p}-\mathbf{p}_{\mathrm{ref}}\right)^T \gamma^{-1} \left(\mathbf{p}-\mathbf{p}_{\mathrm{ref}}\right) \\ & \left. +\frac{i}{2\hbar} \left(\mathbf{p}+\mathbf{p}_{\mathrm{ref}}\right)^T \left(\mathbf{q}-\mathbf{q}_{\mathrm{ref}}\right) \right]. \end{aligned} \tag{2.31}$$

$\mathbf{p}_{\mathrm{ref}}$ and $\mathbf{q}_{\mathrm{ref}}$ are the reference state mass-weighted momenta and positions, respectively. The overlaps have a general Gaussian form.

2.3 Molecular dynamics simulations and electronic potentials

As explained in the above section, the quantum dynamical equations are expressed in an approximate semiclassical form which takes in classical inputs. The primary input is the classical trajectory. In the survival amplitude integral (Eq. 2.30), the terms are integrated over multiple trajectories. These trajectories are chosen statistical mechanically. The basics of classical mechanics and molecular dynamics were

explained in Section 1.5. Of greatest import (and computationally demanding) is the calculation of the potential. An accurate depiction of the potential interactions in the molecular system is vital for a correct dynamical description. The advantage of using an *ab initio* trajectory is the fact that it is more flexible than a predefined potential, making it advantageous for cases in which the system is situated far from equilibrium.

Quantum chemistry calculations of the electronic potential are a complete study in itself, and a fully accurate description requires benchmarking over many electronic theories and basis sets. Each method used in this thesis is briefly described in Appendix B.

2.4 Photochemical Studies

In a photochemical study where molecules are excited by light, the molecules may be in various positional configurations prior to excitation. For instance, they can be on the electronic ground state potential surface, possessing any value of kinetic energy. Therefore, it is common to generate an ensemble of configurations which are used as starting points for the excited state dynamics. An ensemble may be generated by Monte Carlo or it may be assumed that all configurations are at the same temperature; thus, in a canonical (NVT) ensemble. An NVT molecular dynamics simulation follows the standard MD (NVE) procedure as given before, but the system is also in contact with an external bath. This bath regulates the average energy of the system after a number of timesteps, maintaining a constant temperature.

After the initial conditions are computed, they may be used for microcanonical (or NVE) dynamics on the excited state surface. In our case, we chose to examine the lowest electronic potential surfaces of CH_3OCl. It is a well-studied system [52, 53] and a good photoexcitation model. Upon photoexcitation, the system is immediately raised to an excited electronic state, without any change in the nuclear positions

(Franck-Condon principle). The state that the system ends up in depends on the energy of excitation, and the intensity of the transition based on the relative overlap of the wavefunctions of the initial and excited state. While on these excited surfaces, the molecule is on a dissociative path. The resultant products of the dissociation are the main interest in such a study.

2.5 Vibrational States

Returning to semiclassical dynamics, the techniques developed to do the above *ab initio* dynamical studies are directly applicable here. Only NVE trajectories on the potential ground state are required as the focus is on the vibrational states (rotational states are not considered). How these trajectories are chosen for the integration will be discussed in Chapter 4. Because of the extensive number of trajectories and the length of each trajectory, it is advantageous to reduce the number of electronic structure calls for the potential and its derivatives. The problematic term in Eq. 2.30 is the Herman-Kluk prefactor, $R_{\mathbf{p}_0,\mathbf{q}_0,t}$, for it involves derivatives at each timestep of $\mathbf{p}_t$ and $\mathbf{q}_t$ with respect to $\mathbf{p}_0$ and $\mathbf{q}_0$ (see Eq. 2.28). While calculable, this is not desirable. The first method of improving the efficiency of this calculation is re-expressing $R_{\mathbf{p}_0,\mathbf{q}_0,t}$ in a log-derivative form [54]:

$$R_{\mathbf{p}_0,\mathbf{q}_0,t} = \sqrt{\det\left[\frac{1}{2}\left(1+\frac{i}{\hbar}\gamma^{-1}\mathbf{A}_t\right)\right]}\exp\left[\frac{1}{2}\int_0^t \mathrm{Tr}(\mathbf{A}_{t'})dt'\right], \tag{2.32}$$

where $\mathbf{A}$ is the solution of the differential Riccati equation:

$$\frac{\partial \mathbf{A}_t}{\partial t} = -\mathbf{F}_t - \mathbf{A}_t^2. \tag{2.33}$$

$\mathbf{F}$ is the force constant matrix. The initial value $\mathbf{A}_0$ is $\hbar\gamma/i$. This form of $R_{\mathbf{p}_0,\mathbf{q}_0,t}$ is exactly equivalent to Eq. 2.28. Since the log-derivative form still requires the solution of a numerical differential equation, an approximation is sought. Johnson's

WKB approximation [54, 55] reduces the prefactor to

$$R_{\mathbf{p}_0,\mathbf{q}_0,t} = \exp\left[-\frac{i}{\hbar}\int_0^t dt' \sum_{j=1}^{3N-6} \frac{\hbar\omega_j(t')}{2}\right], \tag{2.34}$$

where ω_j corresponds to the angular frequency of each vibrational mode j at time t'. This is the *local* harmonic frequency (a frequency calculation not necessarily at a stationary point) of each timestep of the trajectory. It may be calculated at the same time as the dynamics step, reducing the electronic structure calculation overhead. This prefactor has been successfully used in studies of the vibrational states of weakly-bound trimers and the water dimer [56–59].

The reference state constitutes a chosen "trial" wavefunction, which is the desired state of interest. Eq. 2.26 is the correlation of the state of the system with this reference function, meaning the chosen reference function serves as an "extractor" for eigenstates near it. Note that, in practice, $|\Psi_{\mathrm{ref}}\rangle$ is also symmetry-adapted. Therefore, to determine specific vibrational states, reference states are chosen that overlap as much as possible with the real eigenstate. The form of the reference function is of great import and part of ongoing research [60].

The Fourier Transform (FT) of the survival amplitude into energy-space:

$$I(\omega) = \frac{1}{2\pi}\int_{-\infty}^{\infty} dt\; e^{i\omega t} C(t), \tag{2.35}$$

gives the energy spectrum. The peaks of this spectrum are the vibrational state energies. The intensities of the resultant spectra are not quantitative, as they only represent the magnitude of overlap (i.e., based on the reference state). However, a strong and narrow signal allows for precise determination of the energy levels.

2.6 Time-averaged SC-IVR

The double integral over the phase space may span tens of thousands of trajectories. Each of these trajectories are independent, serially-determined computations (the

trajectory and force constant calculations are serial processes, but the actual computation of the integral can be parallelized). The electronic structure bottleneck is huge, even for a computationally efficient method like Hartree-Fock. To correctly interpret experimental results (i.e., requiring the use of the best available high-level accurate quantum chemistry), the solution may become intractable. Since SC-IVR is being developed as an alternative approach to other quantum dynamical methods, it should be at least equally as efficient as these methods. Miller *et al.* [61] introduced a modification to the SC-IVR equation by using the ergodic hypothesis; the particle traversal at the limit of long t equals the traversal in phase space:

$$A_{\text{obs}} = \bar{A}_{\text{phase space}} = \lim_{t_{\text{obs}} \to \infty} \frac{1}{t_{\text{obs}}} \int_0^{t_{\text{obs}}} A(p(t), q(t))\, dt. \tag{2.36}$$

This "time-averaged" SC-IVR method [59, 61, 62] takes advantage of longer, but fewer trajectories. The assumption is that the Monte Carlo initial conditions from the original SC-IVR equation (Eq. 2.26) are equivalent to random points along a very long trajectory (see Fig. 2.2).

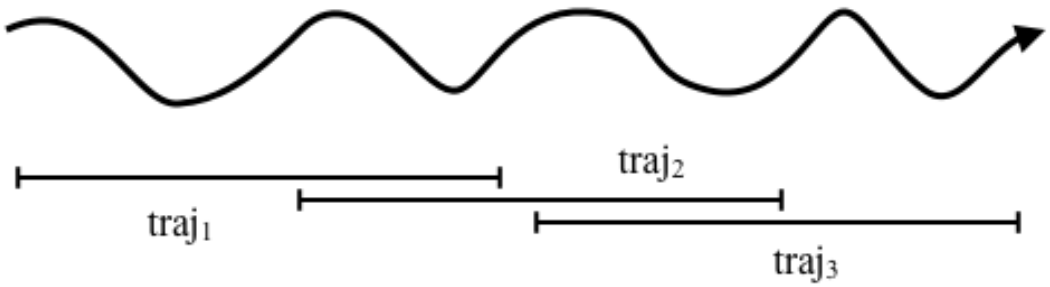

Figure 2.2: A long trajectory (curved arrow) can be split into multiple segments. Each segment can be considered its own trajectory with a different initial condition in phase space.

The survival amplitude includes an extra time-integral term, yet, since significant parts of trajectories are being reused, as long as all trajectory and Hessian (second derivative of the potential) data are saved, total computational time drops. In the extreme case, a single very long trajectory is used and the double phase space integral

vanishes. The time-averaged form of the survival amplitude is

$$\begin{aligned} C_{\mathrm{TA}}(t) &= (2\pi\hbar)^{-3N} \int\int \mathrm{d}\mathbf{p}_0 \mathrm{d}\mathbf{q}_0 \, \frac{1}{T} \int_0^T dt_1 R_{\mathbf{p}_{t_1}\mathbf{q}_{t_1}t_2} \\ &\times \; e^{iS_{\mathbf{p}_{t_1}\mathbf{q}_{t_1}t_2}/\hbar} \langle \Psi | g_{\mathbf{p}_{t_2}\mathbf{q}_{t_2}} \rangle \langle g_{\mathbf{p}_{t_1}\mathbf{q}_{t_1}} | \Psi \rangle. \end{aligned} \tag{2.37}$$

This variant of SC-IVR will be investigated in Chapter 5.

2.7 Vibrational Configuration Interaction technique for calculating vibrational states

[This section is an excerpt reprinted with permission from The Journal of Chemical Physics: S.Y.Y. Wong, D.M. Benoit, M. Lewerenz, A. Brown and P.-N. Roy, *Determination of molecular vibrational state energies using the ab initio semiclassical initial value representation: Application to formaldehyde*, JCP, **134**, 094110 (2011). Copyright 2011, American Institute of Physics. Contribution to this section of the article was provided by D.M. Benoit [63, 64].]

To determine the accuracy of semiclassical SC-IVR vibrational state results, we used a number of computational methods for comparison: correlation-corrected vibrational self-consistent field/two-mode coupling representation of a quartic force field (cc-VSCF/2MR-QFF), direct cc-VSCF, vibrational self-consistent field/vibrational configuration interaction with perturbation selected interactions-second order perturbation (VSCF/VCIPSI-PT2) and curvilinear-VSCF/VCIPSI-PT2.

The vibrational self-consistent field (VSCF) procedure provides a variational solution to the vibrational Schrödinger equation [65, 66]. It uses a separable product of one-coordinate functions to represent the total vibrational wavefunction, such that

$$\Phi_{\mathbf{n}}(\mathbf{Q}) = \prod_{j=1}^{N} \varphi_{n_j}^{(\mathbf{n})}(Q_j), \tag{2.38}$$

where $(\mathbf{n})$ is a collective index representing the vibrational state of interest, be it the ground state or any singly excited state, overtone or combination band. GAMESS-

US [17] implements a correlation-corrected VSCF where the potential energy surface including up to 2-mode couplings can either be computed using a quartic force field (cc-VSCF/2MR-QFF) [67] or by computing the PES on a grid using single-point calculations (direct cc-VSCF) [68].

In the methodology developed by Benoit and co-workers, [63, 64] a variation-perturbative approach, perturbative screening is used to iteratively update the initial VCI active space (VSCF/VCIPSI-PT2). This calculation can be performed for a PES expressed either in rectilinear or curvilinear coordinates (curvilinear-VSCF/VCIPSI-PT2), which lends to more efficient computation. The advantage of using curvilinear coordinates is that it is amenable to systems of multiple local minima and that it reduces mode–mode coupling, leading to a more accurate representation of the vibrational states. Rectilinear coordinates, on the contrary, often expand the wavefunction over a single minimum and can introduce artificially large mode–mode couplings.

In the current implementation (see Ref. [64] for details), the set of curvilinear coordinates $\mathbf{q}$ is transformed into curvilinear normal mode coordinates, $\mathbf{Q}$. The corresponding metric tensor is constant and reduced to an identity operator δ_{ij}. The application of the variational principle to the resulting Hamiltonian:

$$\hat{\mathbf{H}} = -\frac{1}{2}\sum_{j=1}^{N}\frac{\partial^2}{\partial Q_j^2} + \underbrace{\sum_{j=1}^{N} V_j^{(1)}(Q_j) + \sum_{i=1}^{N}\sum_{j>i}^{N} V_{ij}^{(2)}(Q_i, Q_j)}_{V(\mathbf{Q})} \tag{2.39}$$

leads naturally to N one-dimensional equations:

$$\left\{ -\frac{1}{2}\frac{\partial^2}{\partial Q_j^2} + V_j^{(1)}(Q_j) + \vartheta_j^{(\mathbf{n})}(Q_j) \right\} \varphi_{n_j}^{(\mathbf{n})}(Q_j) = \epsilon_{n_j}^{(\mathbf{n})} \varphi_{n_j}^{(\mathbf{n})}(Q_j) \tag{2.40}$$

that are coupled through a mean-field potential:

$$\vartheta_j^{(\mathbf{n})}(Q_j) = \left\langle \varphi_{n_i}^{(\mathbf{n})} \prod_{i\neq j} \middle| \sum_{i\neq j}^{N} V_{ij}^{(2)}(Q_i, Q_j) \middle| \prod_{i\neq j} \varphi_{n_i}^{(\mathbf{n})} \right\rangle . \tag{2.41}$$

The last two terms of the right-hand side of Eq. 2.39 are a representation of the potential energy surface as a hierarchical expansion to second-order in curvilinear

normal modes. Each term of the potential expansion is computed on a grid of points (direct approach), providing a simple and automatic way of generating the PES directly from *ab initio* data without requiring an analytic expression for $V(\mathbf{Q})$. Note that, for a curvilinear coordinate system, an extra potential term may appear in the kinetic energy operator when a non-Euclidian normalization convention is used. We neglect this contribution as it is typically very small compared to the potential energy term.

The set of Eqns. 2.40 are solved self-consistently until convergence of the total VSCF energy. We then compute the correlated vibrational eigenstates by diagonalising the full Hamiltonian of Eq. 2.39 in a virtual VSCF basis, as suggested originally by Bowman *et al.* [69–71] We perform this type of vibrational configuration interaction (VCI) calculation for each VSCF-optimised state and use virtual excitations to construct the VCI matrix in each case:

$$\langle \Phi_{\mathbf{r}} | \, \hat{\mathbf{H}} \, | \Phi_{\mathbf{s}} \rangle = \sum_{i=1}^{N} \epsilon_{r_i} \prod_{k \neq i} \delta_{r_k s_k} + \langle \Phi_{\mathbf{r}} | \, \Delta V^{(\mathbf{n})} \, | \Phi_{\mathbf{s}} \rangle \, , \tag{2.42}$$

where the state-specific vibrational correlation operator, $\Delta V^{(\mathbf{n})}$ is defined as:

$$\Delta V^{(\mathbf{n})} \;\; = \;\; \sum_{i=1}^{N} \sum_{j>i}^{N} V_{ij}^{(2)}(Q_i, Q_j) - \sum_{j=1}^{N} \vartheta_j^{(\mathbf{n})}(Q_j). \tag{2.43}$$

Note that index $(\mathbf{n})$ indicates that the effective potential is computed for optimised VSCF state $|\Phi_{\mathbf{n}}\rangle$. The resulting VCI matrix is diagonalised using our iterative VCIPSI-PT2 procedure based on a Davidson algorithm [72–74] adapted for vibrational calculations by Carter *et al.* [71].

2.8 Goal

We now embark on developing our computational and analysis tools for molecular and semiclassical dynamics. New implementations and results will be discussed. The existing methods in this chapter are critically analyzed. Novel approaches will be discussed and summarized in the final chapter of this thesis.

Chapter 3

Ab initio Molecular Dynamics

This chapter is based upon S.Y.Y. Wong, P.-N. Roy and A. Brown, *Ab initio Electronic Structure and Direct Dynamics Simulations of CH_3OCl.* Reused with permission, Canadian Journal of Chemistry, **87** 1022 (2009). Copyright 2009 NRC Research Press. It has been expanded upon and modified.

3.1 Introduction

The first part of this research work consisted of developing the molecular dynamics tools so that one can later calculate vibrational state energies of small molecules using SC-IVR techniques. The first requirement for an SC-IVR calculation is its classical inputs, which are the molecular dynamics trajectories. The Molecular Modeling software package MMTK [75] has been used in numerous instances,[1] although largely for systems with only pre-existing integrated model potentials or parametrized force fields. At the time, direct dynamics had not been introduced into the program (either internally or as an external add-on). Therefore, it was desirable to develop this tool and to choose a chemically-interesting problem to investigate. A direct dynamics study of an atmospherically-interesting molecule, CH_3OCl, was chosen. The basic dynamics tools were found in MMTK already. However, the potentials found in the software were only models or empirically-derived, and most

[1] http://dirac.cnrs-orleans.fr/MMTK/publications/publications-citing-mmtk/

of those available were for biochemically-relevant molecules. The outset of this research program was to write an interface between the the MMTK package with that of existing electronic structure programs in order to conduct direct dynamics simulations. The advantage is that potentials are calculated "on-the-fly" using *ab initio* electronic structure techniques and, therefore, are more exact and can adapt better to molecular or electronic changes (reactions, surface hopping, etc.). At the time of this research, this had not been implemented before in MMTK. In this particular chapter, we discuss the interface of MMTK with the electronic structure package MOLPRO [18].

In this chapter, we compute the excited state energies, gradients and transition dipole moments for the UV photoexcitation CH_3OCl molecule, determined using computational methods tractable for *ab initio* molecular dynamics. Density functional theory (DFT) for the ground state and CASSCF for the excited states are validated against high-level internally-contracted MRCI results. These lay the groundwork for future studies of the photodissociation of CH_3OCl. This chapter also reports the first implementation of *ab initio* molecular dynamics (AIMD) using MMTK and illustrates its use with both ground and excited state dynamics for CH_3OCl. Sections 3.2 and 3.3.1 detail the previous and present *ab initio* methods used to explore the electronic structure of CH_3OCl. The AIMD techniques are discussed in Sec. 3.3.2. The static electronic structure properties are reported in Sec. 3.4.1 and a comparison is made between those from methods viable for AIMD and high-level benchmark results. Ground electronic state configurational sampling from AIMD for unconstrained and constrained dynamics is discussed in Sec. 3.4.2. Sec. 3.4.2 also contains a brief discussion of AIMD for excited states of CH_3OCl. Finally, some conclusions and an outlook on future uses of AIMD with MMTK are presented in Sec. 3.5.

3.2 Experimental/Theoretical Background

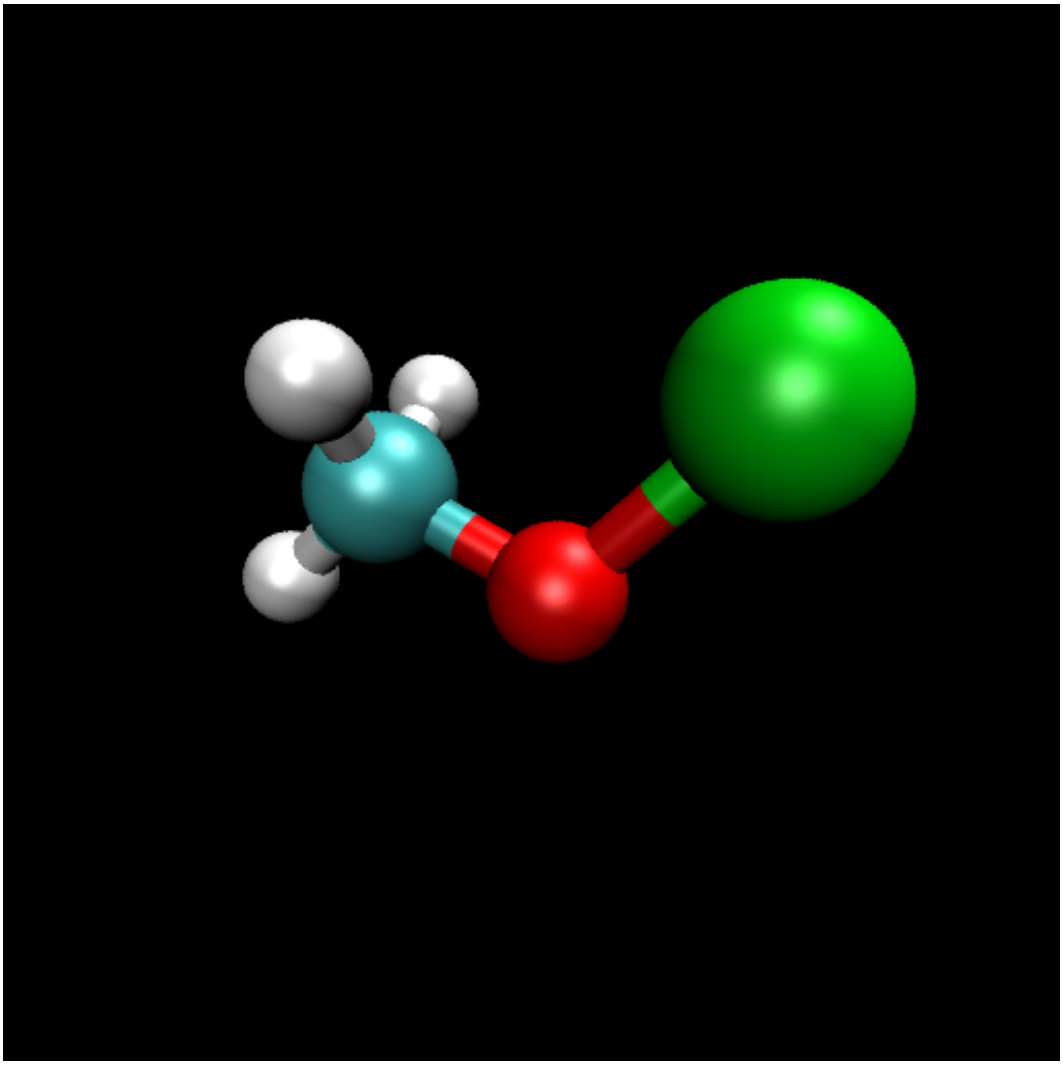

Figure 3.1: The ground state structure of CH_3OCl.

The stratospheric molecule CH_3OCl (see Fig. 3.1) has been shown to be important in ozone chemistry through its role as a reservoir for chlorine [53]. Therefore, it is important to understand the loss mechanisms for CH_3OCl, including its UV absorption and subsequent decomposition. Gas-phase experiments have shown there to be two CH_3OCl absorption peaks between the range of 200-400 nm. The absorption peak at 236 nm is strong and narrow while the one at 310 nm is weaker

and broader.[2] Due to its structural and spectral similarities to HOCl [76, 77], it has been predicted that $CH_3O^{\cdot}$ and $Cl^{\cdot}$ would be the photolysis products [53, 76]. The dominant reaction upon photolysis via either absorption peak was confirmed experimentally [78, 79] as:

$$CH_3OCl + h\nu \rightarrow CH_3O(X^2E) + Cl(^2P), \tag{3.1}$$

where the chlorine atom is produced in either its spin-orbit ground ($^2P_{3/2}$) or excited ($^2P_{1/2}$) state. Theoretical determination of the excited states [52] demonstrated the highly repulsive electronic excited states along the Cl-O coordinate. Butler and co-workers [78] measured the velocity distributions of the photofragments resulting from photodissociation at 248 nm. All their data could be fit assuming $Cl^{\cdot}$ and $CH_3O^{\cdot}$ as the only photoproducts. They determined that the $CH_3O^{\cdot}$ fragments had a narrow range of internal energies (vibration and primarily rotation). Schindler *et al.* [79] used resonantly enhanced multiphoton ionization time-of-flight mass spectrometry to measure the $Cl^{\cdot}$ radical fragments produced following excitation at 308 nm and 235/237 nm - different wavelengths were used to detect $Cl(^2P_{3/2})$ versus $Cl(^2P_{1/2})$. The chlorine atoms were formed with nearly equal probability at both wavelengths. Interestingly, the ratio of spin-orbit excited to ground state chlorine atoms, $Cl(^2P_{1/2})/Cl(^2P_{3/2})$, was strongly wavelength dependent with a value of 0.31 ± 0.02 at 308 nm and 1.45 ± 0.05 at 235 nm. Clearly, the photodissociation dynamics of CH_3OCl is quite rich, and thus, it is a useful model molecule for our study.

Francisco [1] completed an equilibrium structure and vibrational frequency study of CH_3OCl with density functional theory B3LYP/6-31++G(3df,3pd) and coupled-cluster theory CCSD(T)/6-311G(2df,2p) where the results show a structure similar to that of methanol. Li and Francisco [52] have determined energetics for

[2] JPL-97, JPL-2002 and JPL-2005 recommended the mean values of Crowley *et al.* [53] and Jungkamp *et al.* [76].

low-lying singlet and triplet excited electronic states using complete active space self-consistent field (CASSCF) followed by internally-contracted multi-reference configuration interaction (MRCI) with cc-pVTZ and/or cc-pVTZ+sp basis sets. Peyerimhoff and co-workers [80, 81] have examined similar properties for CH_3OCl using CCSD(T)/cc-pVTZ (equilibrium structure and vibrational frequencies) and MRCI/cc-pVTZ+sp (vertical excitation energies). The goal of the present study is not to reproduce these results, but to demonstrate that a computationally efficient method will provide an energetically-correct characterization of CH_3OCl, consistent with the previously reported findings above. The necessity for a merely "sufficient" method is to be able to practically conduct direct dynamics simulations. To this effect, single-point calculations along the O-Cl bond coordinate are demonstrated to provide semi-quantitatively the potential energy surface and energy gradients of the first three singlet states. In the present study, we neglect the roles that low-lying triplet states and spin-orbit coupling play in the dissociation process. In the Franck-Condon region, the singlet ground-to-triplet excited state transitions are essentially forbidden, and, thus, the triplet states play no role in the initial excitation process. As the molecule dissociates, coupling between the singlet and triplet states becomes important as the states approach the asymptote and are energetically similar. The coupling manifests itself in the production of both $Cl(^2P_{3/2})$ and $Cl(^2P_{1/2})$ fragments. Therefore, if one wants to interpret the experimental measurements [79] of the branching ratio for these photoproducts, the spin-orbit coupling will have to be taken into account - this is not the purpose of the present study.

3.3 Computational Methods

3.3.1 Electronic Structure

There have been several previous theoretical studies of the ground state structure and vibrational frequencies of CH_3OCl [1, 81–83]. In particular, there have been

two benchmark studies by Francisco [1] and by Peyerimhoff and co-workers [81] at the CCSD(T)/6-311G(2df,2p) and at the CCSD(T)/cc-pVTZ levels of theory, respectively. Unless otherwise specified, all single-point calculations reported in this article have been carried out at the equilibrium geometry determined by Francisco (see Table 3.1) using C_s symmetry. Since the CCSD(T) methodology is too computationally expensive for dynamics calculations, a B3LYP/6-31G(d) geometry optimization and vibrational frequency analysis were performed to assess the suitability of this level of theory for ground state configurational sampling (see the discussion in Sec. 3.3.2). The B3LYP/6-31G(d) ground state structure (Table 3.1) and vibrational frequencies (Table 3.2) as compared to the benchmark CCSD(T) results indicate that this method and basis set provide a suitable representation for the ground state potential energy surface, including the equilibrium structure, with respect to both bases mentioned above. For example, the bond lengths differ by less than 0.05 Å and the angles by less than 1.3 degrees. Importantly, the frequencies also differ by a maximum of 5% and, in most cases, are within 1% of the benchmark results.

Table 3.1: Equilibrium geometry of CH_3OCl at the B3LYP/6-31G(d) level of theory as compared to previous benchmark results. Bond lengths are given in Å and bond/dihedral angles in degrees. H_a refers to the H-atom lying on the same plane as C-O-Cl, while $\mathrm{H}_{b,c}$ are the two out-of-plane hydrogen atoms.

Parameter	This work B3LYP/ 6-31G(d)	Ref. [1] CCSD(T)/ 6-311G(2df,2p)	Ref. [81] CCSD(T)/ cc-pVTZ	Ref. [84] Expt.
r_{CO}	1.425	1.425	1.425	1.389
r_{OCl}	1.736	1.709	1.689	1.674
r_{CH_a}	1.096	1.089	1.089	1.068
$r_{\mathrm{CH}_{b,c}}$	1.097	1.091	1.089	1.111
θ_{COCl}	110.4	109.2	109.3	112.8
$\theta_{\mathrm{H}_a\mathrm{CO}}$	103.3	104.4	—	—
$\theta_{\mathrm{H}_{b,c}\mathrm{CO}}$	111.9	111.4	—	—
$\tau_{\mathrm{H}_{b,c}\mathrm{COCl}}$	62.0	61.5	—	—

Table 3.2: Vibrational frequencies and assignments (cm^{-1}) at the B3LYP/6-31G(d) level of theory compared to experimental results and previous benchmark calculations.

Assignment	This work B3LYP/ 6-31G(d)	Ref. [76] Experiment	Ref. [1] CCSD(T)/ 6-311G(2df,2p)	Ref. [81] CCSD(T)/ cc-pVTZ
CH_3 Torsion	260	—	254	261
C-O-Cl Bend	365	—	373	365
O-Cl Stretch	659	680	692	661
C-O Stretch	1023	1002	1046	1020
$H_{b,c}$-C-O Rock	1183	1150	1180	1181
H_a-C-O Rock	1206	1170	1201	1284
CH_3 Umbrella	1477	1424	1467	1475
C-H Asymm. Bend	1487	1456	1479	1488
H_b-C-H_c Scissor	1538	1471	1516	1537
CH_3 Symm. Stretch	3035	2820	3040	3038
H_b-C-H_c Asymm. Stretch	3109	2904	3117	3113
H_a-C-H_b Asymm. Stretch	3131	2920	3144	3133

There have only been two theoretical studies focused on surveying the lowest-lying singlet and triplet excited states for CH_3OCl [52, 80]. In these studies, the authors have determined the energies for the lowest six singlet and triplet states (three A' and three A'' for each spin multiplicity). From these works, the two lowest energy absorptions observed experimentally at 310 nm and 236 nm [76] are identified with excitation to the $1^1A''$ and $2^1A'$ states, respectively. These two low-lying electronic states are the focus of this work. Benchmark calculations of both vertical excitation energies and transition dipole moments have been carried out using the augmented correlation consistent family of basis sets (aug-cc-pV*X*Z, *X* = D, T, and Q) [85–87]. In order to determine the energies and transition dipole moments, state-averaged complete active space self-consistent field (SA-CASSCF) calculations [88–90] were carried out including two A' and one A'' states. Following the work of Li and Francisco [52], the active space consisted of fourteen electrons in ten active orbitals (7 and 3 active MO's in A' and A'' symmetry, respectively). The CASSCF method is briefly explained in Sec. B.4. Essentially, a 20-orbital region is chosen to represent

the occupied and potentially occupied orbitals. The lower (closed) orbitals are, of course, fully occupied in all states of excitation in the study; the rest (virtual) are available for potential electron occupation (see Fig. 3.2).

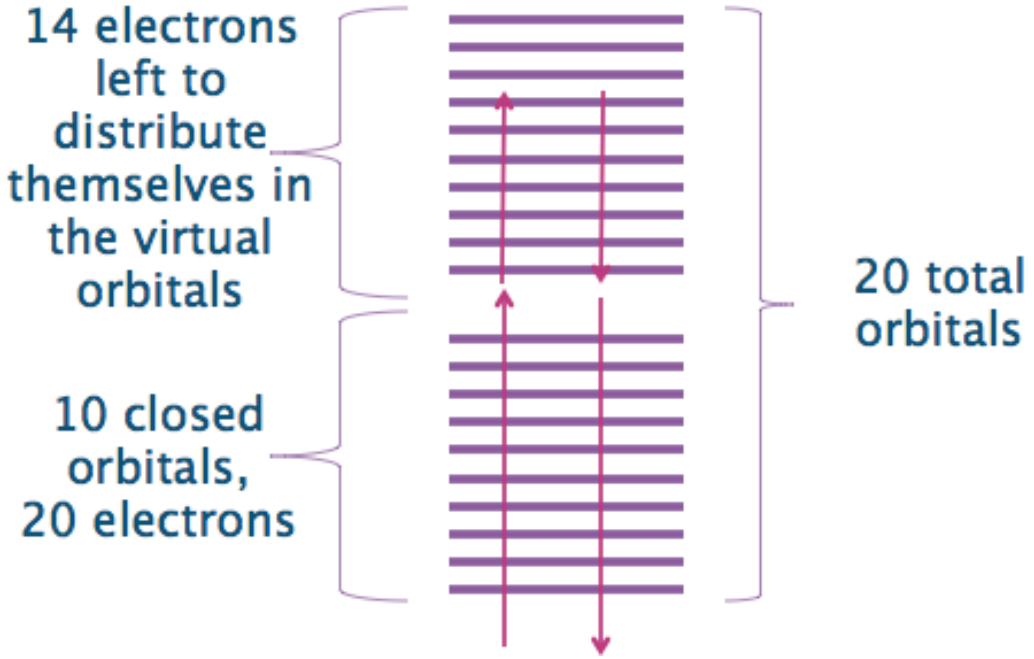

Figure 3.2: The CASSCF study consisted of 34 electrons and 20 orbitals. Of the 20 orbitals, 10 are active and the remaining 14 electrons can distribute within them.

The resulting CASSCF orbitals and wavefunctions were then used for internally-contracted multi-reference configuration interaction (MRCI) [91, 92] calculations. For the MRCI calculations, the effect of higher-order excitations on the energies was estimated using the Davidson correction [93]. All electronic structure calculations reported in this article were carried out using the MOLPRO *ab initio* electronic structure program [18].

The MRCI method is suitable for single-point calculations (or even potential energy scans) but it is far too computationally intensive to be utilized for a direct dynamics study. The benchmark calculations used were used to gauge the accuracy of SA-CASSCF calculations using the same (14,10) active space as described above but with the much more modest 6-31+G(d) basis set [94–97]. The major difference

was that these calculations were carried out with C_1 symmetry as they will form the basis for future excited state dynamical studies, where the planar symmetry of the molecule will be broken. We would like to use a moderate level of theory since efficiency (speed) is of critical importance for dynamics but we would like to retain a quantitative description of the excited states. In order to do this, the vertical excitation energies were determined, as they provide information on the energetic accessibility of the two excited states. The transition dipoles were used to gather information about the relative probability of accessing either state. Finally, and perhaps most importantly, the energy gradients must be determined since they govern the classical dynamics. In order to assess the accuracy of the SA-CASSCF/6-31+G(d) gradients, they are compared with numerical MRCI gradients at a small number of geometries – note that analytic MRCI gradients are not available in MOLPRO. The comparison of the gradients we make involves a projection onto the O-Cl bond vector, i.e., the primary "reaction" channel, defined by

$$g_{\mathrm{OCl}} = \frac{(\vec{g}_{\mathrm{O}} - \vec{g}_{\mathrm{Cl}}) \cdot (\vec{r}_{\mathrm{O}} - \vec{r}_{\mathrm{Cl}})}{\|\vec{r}_{\mathrm{OCl}}\|}, \tag{3.2}$$

where $\vec{g}_i$ and $\vec{r}_i$ are Cartesian vectors of the atomic gradients and positions, respectively. The numerical MRCI gradients are computed by four-point finite difference using a displacement length of 0.01 bohr along the r_{OCl} bond coordinate.

3.3.2 Molecular Dynamics

Ab initio molecular dynamics simulations on the ground electronic state were carried out using MMTK [75]. MMTK is a simulation and modelling program library written in Python and C which has been proven to be useful for atomic systems to large bio-molecules. Most of the procedures needed in conducting the dynamics is self-contained in program classes which can be called from a main code. Significantly for us, MMTK allows the ready implementation of constrained dynamics, where the bond lengths can be fixed. A proper choice of constraints can "freeze out" high-

frequency vibrations, permitting the use of larger integration timesteps. In order to perform AIMD using MMTK, an *ab initio* force field class that obtains energies and gradients directly from electronic structure calculations was implemented. The electronic structure calculations were performed using the MOLPRO package [18]. The present implementation allows the use of Hartree-Fock (HF), Møller-Plesset second-order perturbation theory, density functional theory (DFT) and CASSCF classical trajectories – methods where analytic gradients are available in MOLPRO. An *ab initio* force field determined using GAMESS [17] has also been developed for HF and DFT trajectories (results not presented here). The computer code for interfacing these *ab initio* electronic structure packages with MMTK is available upon request from the authors.

To generate initial conditions for examining the excited state dynamics (see Fig. 3.3), one requires a sampling of geometries and initial velocities from the ground electronic state. One can do this through Monte Carlo sampling or by running a canonical NVT classical trajectory on the ground state potential energy surface to sample both positions and momenta. In this paper, we chose the latter in order to demonstrate our implementation of AIMD in MMTK. A single long NVT ground state trajectory was generated at the B3LYP/6-31G(d) level of theory and can serve as a sampling of initial conditions of the molecule prior to photoabsorption. The initial conditions of the trajectory consisted of the equilibrium geometry determined at the B3LYP/6-31G(d) level of theory (see Table 3.1) and velocities obtained from a Boltzmann distribution at 300 K. Dynamics were conducted using the Velocity-Verlet integrator [30]. To maintain the constant temperature, a Nosé thermostat [98] with a time constant of 0.2 ps was used. The proper timestep was determined from NVE dynamics and the length of simulation determined from proper phase space coverage. These NVT trajectories were determined for both unconstrained and constrained systems. In the constrained dynamics, the r_{CH} distances were fixed at

their equilibrium values. The excited state dynamics at the CASSCF/6-31+G(d) level is briefly discussed.

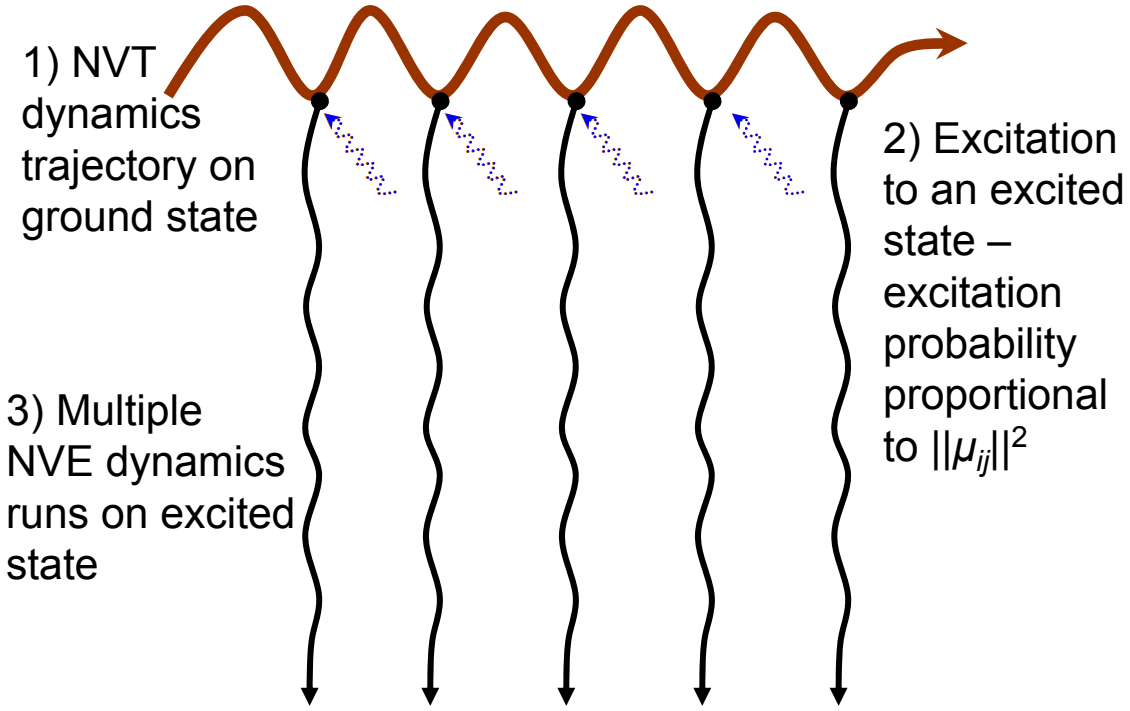

Figure 3.3: The ground state trajectory represents the ground state configurations of the molecule. When a configuration is photoexcited, the molecule is raised to the electronic excited state, keeping its original configuration. Then, excited state dynamics on the new electronic potential surface may be completed.

3.4 Results and Discussion

3.4.1 Static electronic structure

The important properties for photodissociation are the vertical excitation energies from the ground ($1^1A'$) state to the low-lying excited states ($1^1A''$ and $2^1A'$) and the corresponding transition dipole moments. Our results (CASSCF and MRCI), along with previous calculations for CH_3OCl [52, 80] are presented in Table 3.3. All the present results are determined at the CCSD(T)/6-311G(2df,2p) equilibrium geometry [1]. Examining the MRCI vertical excitation energies as a function of increasing basis set size (aug-cc-pVXZ, X = D,T,Q), it is clear that they are

converging to the values of 4.13 eV and 5.27 eV for the $1^1A'' \leftarrow X^1A'$ and $2^1A' \leftarrow X^1A'$ excitations, respectively. The present CASSCF and MRCI excitation energies are consistent with those determined previously [52, 80] and with the experimentally-determined absorption spectra [53, 76] that exhibit maxima at 4.00 eV (310 nm) and 5.25 eV (236 nm). Importantly, the CASSCF/6-31+G(d) energies, upon which we plan to base the direct dynamics, are within 0.180 eV and 0.513 eV of the MRCI/aug-cc-pVQZ results. The comparison between these two differing methods/bases is necessary as the desired dynamics method (CASSCF/ 6-31+G(d)) must be consistent with the benchmark (MRCI/aug-cc-pVQZ).

Table 3.3: Vertical excitation energies (eV) and, when determined, transition dipole moments (Debye) from the ground (X^1A') to the first ($1^1A''$) and second ($2^1A'$) excited states. Present results determined at the CCSD(T)/6-311G(2df,2p) equilibrium geometry [1].

			Transition Energy (transition dipole moment)	
Reference	Basis	Method	$1^1A'' \leftarrow X^1A'$	$2^1A' \leftarrow X^1A'$
Present work	aug-cc-pVDZ	CASSCF	4.826 (0.262)	5.957 (0.430)
		MRCI	4.136 (0.052)	5.317 (0.257)
	aug-cc-pVTZ	CASSCF	4.364 (0.283)	5.804 (0.338)
		MRCI	4.132 (0.079)	5.268 (0.264)
	aug-cc-pVQZ	CASSCF	4.371 (0.324)	5.802 (0.417)
		MRCI	4.133 (0.089)	5.269 (0.270)
	6-31+G(d)	CASSCF[a]	4.313 (0.282)	5.782 (0.331)
		CASSCF[b]	4.373 (0.317)	5.867 (0.388)
Ref. [52]	cc-pVTZ	CASSCF	4.19	5.90
		MRCI	4.17	5.65
	cc-pVTZ+sp	CASSCF	4.53	6.00
		MRCI	4.24	5.58
Ref. [80]	cc-pVTZ+sp[c]	MRCI	4.13 (0.07)[d]	5.50 (0.12)[d]

[a] CASSCF(14,10)
[b] Full valence, i.e., CASSCF(20,15)
[c] Both the basis set and active space used differ from that in Ref. [52].
[d] Converted from oscillator strengths, f, using $\mu = \sqrt{\frac{3f}{2E_{10}}}$

The square of the magnitudes of the transition dipole moments can be used to determine the probability of a transition to each excited state – presently, the transition dipole moments are treated as scalars rather than as vectors. Examining

the CASSCF versus MRCI transition dipole moments for a given basis set (see Table 3.3), it is clear that the inclusion of dynamic correlation plays a significant role in determining their magnitudes. For example, the CASSCF/6-31+G(d) transition dipoles as compared to the MRCI/aug-cc-pVQZ results are reduced from 0.282 D ($1^1A'' \leftarrow X^1A'$) and 0.331 D ($2^1A' \leftarrow X^1A'$) to 0.089 D and 0.270 D, respectively. More importantly, the ratio of the square of the dipole moments, which is proportional to the absorption cross section, changes significantly, e.g., for the aug-cc-pVQZ basis set, $(\mu_2/\mu_1)^2$ = 1.38 for CASSCF and 9.30 for MRCI. In order to assess the reliability of the computed transition dipole moments, we can compare as a first-order approximation to the ratio of the experimentally-determined maximum absorption cross sections [53, 76], where $\sigma_{236}/\sigma_{310} = 9.99$. Clearly, the ratios predicted by the CASSCF calculations are incorrect while the MRCI results for the triple- and quadruple-zeta basis sets agree fairly well with experiment. For future excited state direct dynamics work, the CASSCF results will be unable to predict correctly the relative populations of the $1^1A''$ and $2^1A'$ states. Therefore, a geometry-independent dipole will be assumed and the populations in the states will be weighted 1:9 if both states are energetically accessible.

The CASSCF/6-31+G(d) energies also need to be considered away from the ground state equilibrium geometry as the eventual goal of the research is to examine the photodissociation dynamics, where the molecule will access geometries far from equilibrium. Figure 3.4 shows the potential energy curves for the first three singlet states of CH_3OCl as determined using the CASSCF/6-31+G(d) level of theory. As expected from previous investigations [52, 80], the excited states are highly repulsive in the r_{OCl} coordinate. Since the dynamics will break the C_s symmetry of the molecule, the CASSCF calculations have been performed using C_1 symmetry, i.e., no symmetry. One difficulty with carrying out the calculations in C_1 symmetry is that root-flipping problems can occur in the asymptotic region of the potentials.

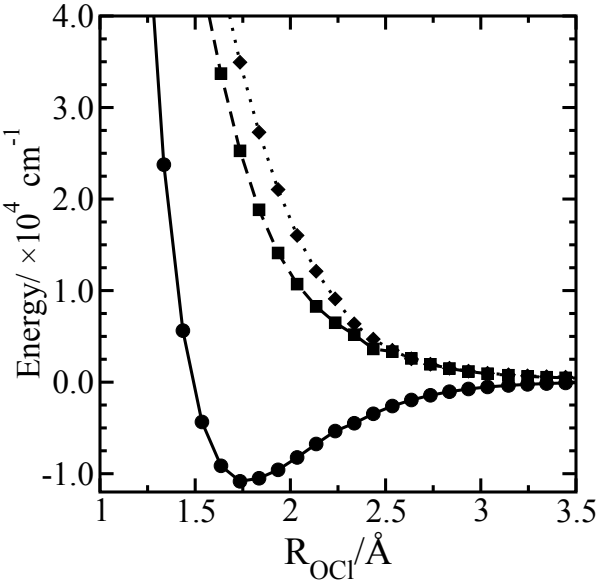

Figure 3.4: Energies at the CASSCF/6-31+G(d) level of the first three singlet states of CH_3OCl as a function of the R_{OCl} bond length. All other bond parameters fixed at those of the B3LYP/6-31G(d) ground state equilibrium geometry. Calculations are carried out in C_1 symmetry and, therefore, the states (along with their C_s symmetries) illustrated are 1^1A = X^{1}A′ (solid line + circles), 2^1A = 1^1A″ (dashed line + squares), and 3^1A = 2^1A′ (dotted line + diamonds).

Gradients serve the purpose of providing the acceleration term in the Velocity-Verlet integration scheme used for molecular dynamics. Therefore, obtaining accurate forces is more important than the potential energy curves (relative energetics) – although they are, of course, intimately related. The gradients for the first excited state (1^1A″ in C_s symmetry = 2^1A in C_1 symmetry) as a function of the r_{OCl} bond length (all other coordinates are fixed at the B3LYP/6-31G(d) optimized geometry) are shown in Fig. 3.5. The CASSCF/6-31+G(d) gradients are compared to those from MRCI/aug-cc-pVDZ and MRCI/aug-cc-pVTZ determinations at four bond lengths (r_{OCl} = 1.536, 1.736, 1.936, and 2.136 Å). The MRCI results are noticeably smaller in magnitude than the corresponding CASSCF results – the ratio of the MRCI/aug-cc-pVTZ to the CASSCF results is approximately 0.4 for all four r_{OCl}

bond lengths considered. The gradients for the second excited state ([2^1A$'$ in C_s symmetry = 3^1A in C_1 symmetry], see Fig. 3.6) are qualitatively similar to those of Fig. 3.5, where now the MRCI/aug-cc-pVTZ to CASSCF ratio is approximately 0.5. Hence, we conclude that the CASSCF/6-31+G(d) gradients provide a qualitative picture for guiding the excited state dynamics – a semi-quantitative picture could be obtained through simple scaling of the CASSCF/6-31+G(d) gradients. Importantly, the CASSCF/6-31+G(d) energy and analytic gradient calculations are reasonable in computational time (approximately 2 minutes per geometry) for performing AIMD while those using MRCI/aug-cc-pV*X*Z are prohibitive. Note that for $r_{\mathrm{OCl}} > 2.5$ Å, there is a problem with root-flippping as the 2^1A$'$ (3^1A) state becomes lower in energy than ^{1}A$''$ (2^1A); this is obvious due to the observation of a discontinuity in the original gradient calculations. Therefore, the potentials, Fig. 3.4, and gradients, Figs. 3.5 and 3.6, present results where the root-flipping has been accounted for "by hand". When AIMD is determined in the excited states, the root-flipping must be accounted for automatically or trajectories must be terminated before $r_{\mathrm{OCl}} > 2.5$ Å.

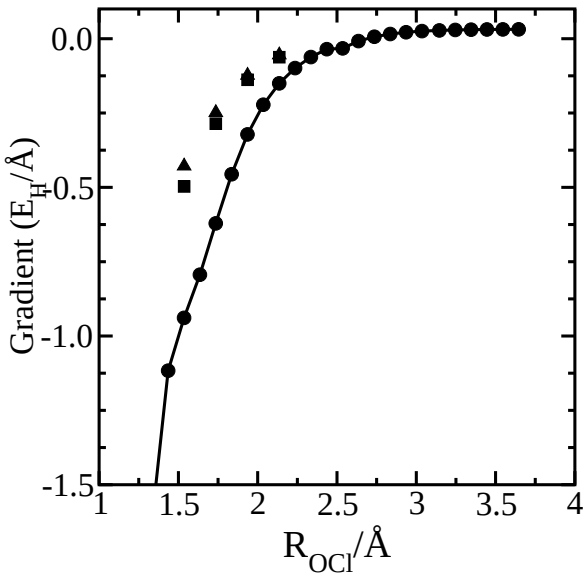

Figure 3.5: Gradient projections of the first excited state (2^1A = 1^1A″) onto the O-Cl bond vector as a function of the R_{OCl} bond length: CASSCF/6-31+G(d) (circles), MRCI/aug-cc-pVDZ (squares), and MRCI/aug-cc-pVTZ (triangles). Other coordinates are fixed at the B3LYP/6-31G(d) optimized geometry.

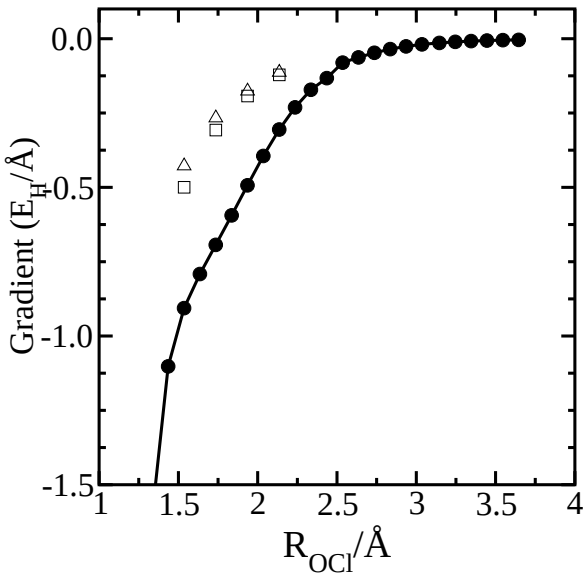

Figure 3.6: Gradient projections of the second excited state (3^1A = 2^1A′) onto the O-Cl bond vector as a function of the R_{OCl} bond length: CASSCF/6-31+G(d) (circles), MRCI/aug-cc-pVDZ (squares), and MRCI/aug-cc-pVQZ (triangles). Other coordinates are fixed at the B3LYP/6-31G(d) optimized geometry.

3.4.2 Ground and Excited State Dynamics

Presented here are NVT ground state trajectories at the B3LYP/6-31G(d) level. In the first case, motion in all $3N-6$ internal degrees of freedom is allowed. In the second case, to remove high frequency vibrational motions, all three C-H bonds are fixed at their equilibrium bond lengths. To determine an appropriate timestep, equivalent NVE simulations with various timesteps (dt) are run. Equilibration occurs within a few femtoseconds. By applying constraints, we are able to increase the timestep about three-fold (from $\sim$2 fs in unconstrained dynamics to $\sim$5 fs with constrained dynamics) before energy conservation is violated or SCF non-convergence occurs in the electronic structure calculation, when large timesteps lead to significant geometric and, hence, electronic, changes. The latter point is of particular importance in AIMD simulations. Therefore, the energy convergence tests are merely to show the general

upper limit on dt for the unconstrained and constrained systems. As a prescription, we suggest that actual production runs should be performed at smaller timesteps.

Figs. 3.7-3.10 present histograms of the R_{CO} and R_{OCl} bond lengths, the COCl bond angle, θ_{COCl}, and the torsional angle, $\tau_{\mathrm{H}_a\mathrm{COCl}}$, respectively, from 9.6 ps unconstrained and constrained NVT trajectories ($dt = 2$ fs and $dt = 4$ fs, respectively). As expected, in the ground state at this temperature, the harmonic-like C-O bond exhibits a Gaussian distribution centred about the equilibrium bond length. Similarly, the O-Cl bond, COCl bond angle and torsional angle exhibit canonical behaviour. The Cl fragment neither diverges too far from its equilibrium distance to the O nor changes exceedingly from its orientation with respect to the C-O. For the constrained simulation, note that the methyl group isomerizes and H_a occupies equivalent minima at 60°, 180° and 300°. Taking all the above into consideration, the use of a canonical NVT trajectory to sample initial ground state distributions is certainly feasible, although it should be implemented with care. A small enough timestep needs to be taken to prevent integrator problems that can adversely affect *ab initio* calculations. Yet, the simulation must be long enough for all modes to reach the canonical limit. The use of a Monte Carlo sampling scheme may allow us to circumvent such difficulties.

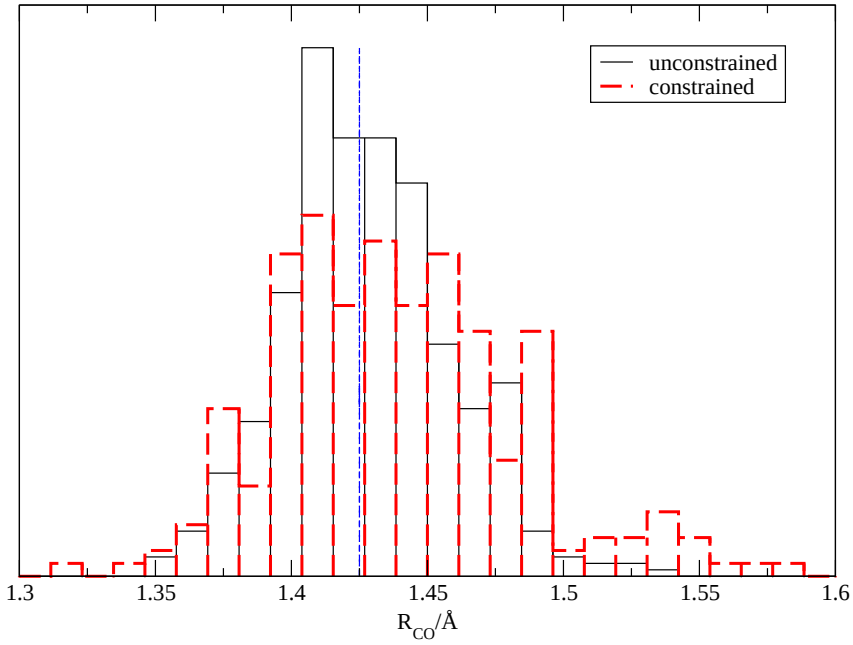

Figure 3.7: The canonical distribution of C-O bond lengths (R_{CO}) for unconstrained and constrained (with C-H bond lengths fixed at their equilibrium values) dynamics. Both trajectories are at the B3LYP/6-31G(d) level of theory. Trajectory length is 9.6 ps for both unconstrained ($dt = 2$ fs) and constrained ($dt = 4$ fs) dynamics. The vertical line represents the equilibrium value.

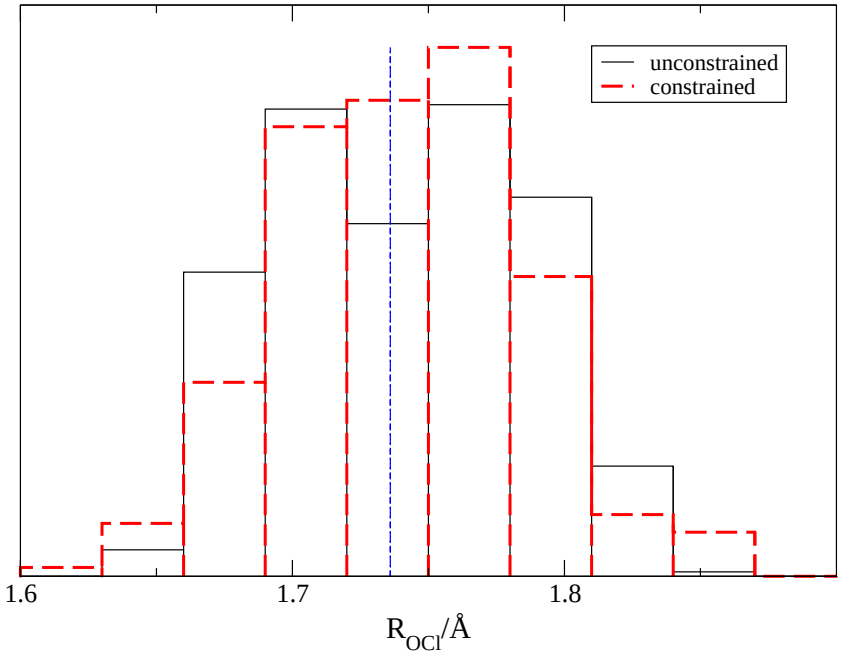

Figure 3.8: The canonical distribution of O-Cl bond lengths (R_{OCl}) for unconstrained and constrained (with C-H bond lengths fixed at their equilibrium values) dynamics. Both trajectories are at the B3LYP/6-31G(d) level of theory. Trajectory length is 9.6 ps for both unconstrained ($dt = 2$ fs) and constrained ($dt = 4$ fs) dynamics. The vertical line represents the equilibrium value.

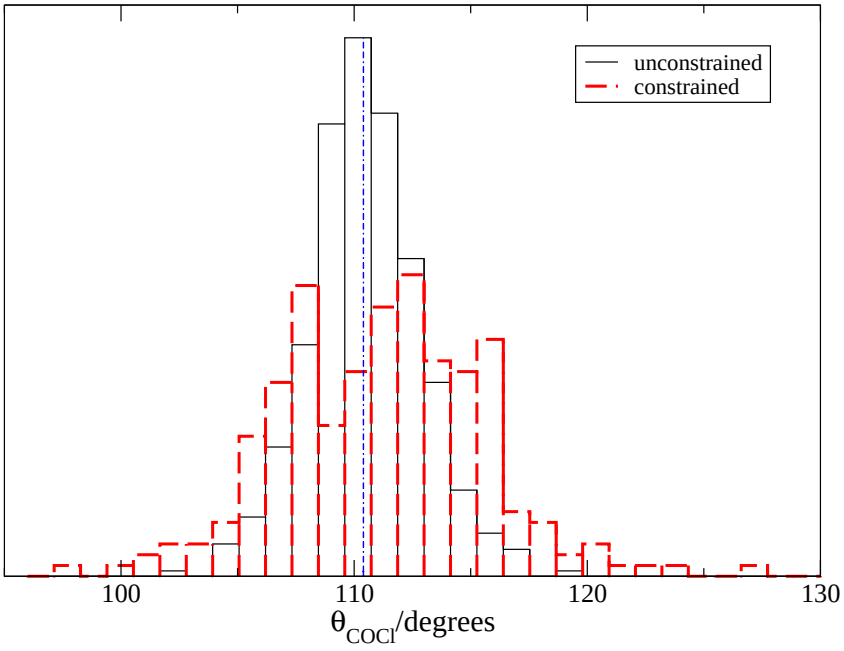

Figure 3.9: The canonical distribution of the C-O-Cl bond angle (θ_{COCl}) for unconstrained and constrained (with C-H bond lengths fixed at their equilibrium values) dynamics. Both trajectories are at the B3LYP/6-31G(d) level of theory. Trajectory length is 9.6 ps for both unconstrained ($dt = 2$ fs) and constrained ($dt = 4$ fs) dynamics. The vertical line represents the equilibrium value.

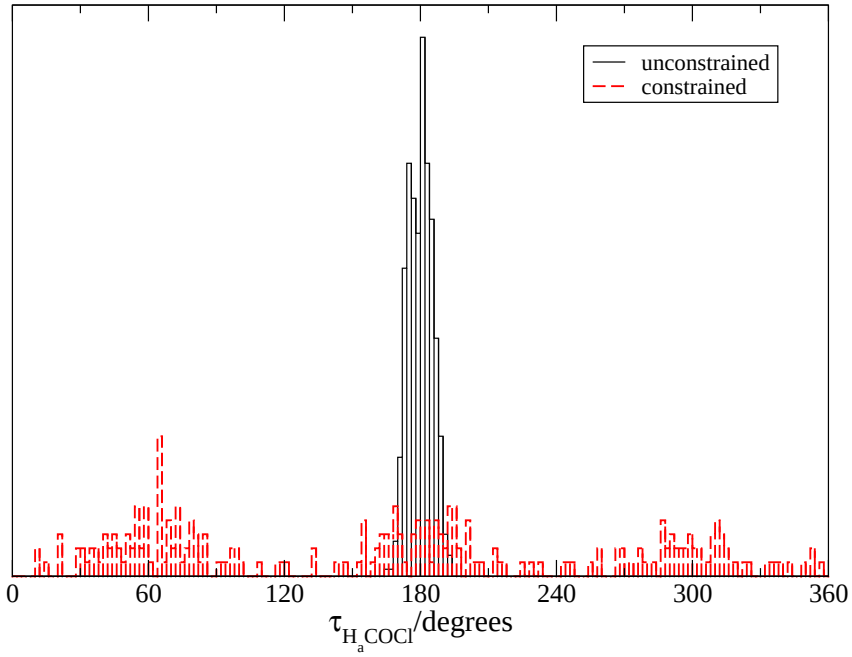

Figure 3.10: The canonical distribution of the H_a-C-O-Cl dihedral angle ($\tau_{\mathrm{H}_a\mathrm{COCl}}$) for unconstrained and constrained (with C-H bond lengths fixed at their equilibrium values) dynamics. Both trajectories are at the B3LYP/6-31G(d) level of theory. Trajectory length is 9.6 ps for both unconstrained ($dt = 2$ fs) and constrained ($dt = 4$ fs) dynamics.

Positions and momenta sampled from the constrained ground state trajectory will serve as initial conditions for future excited state dynamics studies. To test AIMD for excited electronic states, a short 20 fs constant energy excited state trajectory is determined on the first excited electronic state (2^1A in C_1 symmetry) at the CASSCF/6-31+G(d) level of theory. The trajectory starts at the ground state equilibrium geometry with no initial kinetic energy (in practice, NVT ground state initial conditions would be used). The molecule quickly reaches the asymptotic dissociation limit ($R_{\mathrm{OCl}} > 2.5$ Å) in about 100 timesteps ($dt = 0.2$ fs). Thus, a single trajectory would take only (approximately) 300 minutes with the present

technology, pointing to the computational feasibility of exploring ensembles of trajectories on the excited electronic states. The entire ensemble of excited state trajectories can then be easily parallelized.

3.5 Conclusions

The three lowest-lying singlet states of methyl hypochlorite have been examined using electronic structure methods for which direct dynamics studies would be computationally feasible, i.e., B3LYP/6-31G(d) for the ground state and CASSCF/6-31+G(d) for the excited states. From this, potential energy scans and energy gradients along the O-Cl bond were obtained with an accuracy comparable to that of MRCI with the aug-cc-pV*X*Z (*X* = D,T,Q) family of basis sets. In particular, the CASSCF gradients are related to the MRCI gradients by only a factor, allowing for appropriate dynamics. Thus, this moderate method is capable of semi-quantitatively representing the benchmark calculations of the CH_3OCl system at a fraction of the computational cost. We have successfully implemented direct dynamics into MMTK using the electronic structure packages MOLPRO (results presented here) and also GAMESS (results not presented here). The power of using an *ab initio* on-the-fly method is that any system – provided electronic structure calculations are computationally feasible – can be studied. Implementing this method with a modular molecular dynamics package lends to portability, generalization and great potential. Note, however, careful analysis of the single-point calculations must be done. In our case, we encountered root-flipping problems and the potential for electronic structure non-convergence of systems far from equilibrium. We have also shown that constrained dynamics can markedly decrease simulation time.

A full dynamical study of CH_3OCl dissociation is the direct next step. In theory, a large set of trajectories generated from a Boltzmann distribution of initial states can be used to produce the sampling pool of ground state configurations from

which photoexcitation (vertical excitation) can occur. However, a Monte Carlo sampling approach may be more practical. One could for instance sample the ground state NVT distribution in the harmonic approximation yielding a Monte Carlo sampling scheme where no rejection step is required. In this case, the Monte Carlo sampling would be more efficient than the MD sampling. The dissociative nature of CH_3OCl in its excited states was demonstrated with our AIMD algorithm, and for this type of process, is highly computationally practical at this level of theory. Further investigations will involve calculating ensemble averages and other structural properties. Quantum dynamical properties are also currently being investigated based on the present tool along with semiclassical initial value representation (SC-IVR) techniques [8, 99–101]. The present work opens the door to the development of semiclassical dynamics with constraints using *ab initio* force fields. This is an advancement over earlier work where the quantum dynamics of rigid water clusters [58, 59] was studied using model potentials. Very recent work has shown the practicality of on-the-fly AIMD-based semiclassical calculations [60, 102–105] and the aforementioned inclusion of constraints is therefore quite timely.

Chapter 4

Vibrational States of H_2CO using the Semiclassical Initial Value Representation

This chapter is based upon S.Y.Y. Wong, D.M. Benoit, M. Lewerenz, A. Brown and P.-N. Roy, *Determination of molecular vibrational state energies using the ab initio semiclassical initial value representation: Application to formaldehyde*. Reprinted with permission from The Journal of Chemical Physics, **134**, 094110 (2011). Copyright 2011, American Institute of Physics. It has been expanded upon and modified.

In the previous chapter, the basis of our molecular dynamics recipe was developed. Molecular dynamics is purely classical (other than the potential, of course) in nature. Here, we introduce semiclassical dynamics, which is a form of simulation to approximately reflect quantum dynamics. The semiclassical (not to be confused with "quasiclassical" [9]) techniques will build upon the tools in Chapter 3. In this chapter, we will demonstrate the use of *ab initio* molecular dynamics (AIMD) trajectories to compute the vibrational energy levels of molecular systems in the context of the semiclassical initial value representation (SC-IVR).

4.1 Introduction

Classical MD simulations are successful in many situations where quantum effects are negligible or not of interest. However, when quantum effects are important, standard MD fails. Properties such as quantized molecular energy states, interference and coherence are non-classical phenomena and are computed from quantum mechanical equations or their isomorphic equivalent, the path integral. The difficulty with solving quantum mechanical equations directly is that of exponential scaling. Therefore, a variety of different approaches have been suggested to circumvent this scaling problem. Depending on the method, certain properties are more easily attainable (or accurate) than others. For example, one may use the multiconfiguration time-dependent Hartree (MCTDH) [27, 106, 107] approach to approximate the full quantum mechanical solution. While a very powerful approach, the MCTDH method in general necessitates a full-dimensional PES fit to product form and, hence, has only been used for modest-sized systems of 3-7 atoms. MULTIMODE [107, 108] is another software code that can calculate ro-vibrational energies of polyatomic molecules by using vibrational self-consistent field (VSCF) and vibrational configuration interaction (VCI). From the path integral formulation, the diffusion Monte Carlo (DMC) method [24] can obtain ground state properties to very good accuracy. Its basis is the expression of the solution to the Schrödinger equation as a sum of exponentials in imaginary time. Unfortunately, DMC works only when the wavefunction is positive, meaning any wavefunction that has nodes (i.e., excited states) will not work. To deal with node-crossing in DMC, one has to apply a fixed-node approach where each region of the wavefunction is treated separately [26] (node-release DMC [109] is a variant). Ring polymer molecular dynamics (RPMD) is another method which can compute dynamical properties. One can then obtain real-time Kubo-transformed time-correlation functions [110]. In practice, however, as system size increases, these methods may become intractable, as either basis set,

dimensionality or convergence issues multiply. For example, we are often limited to using pair potentials for DMC and RPMD or require a full-dimensional PES.

Semiclassical dynamics is another method for obtaining quantum-mechanical properties by representing the system in terms of definite positions and momenta [40]. The framework of computation is then classical. The semiclassical propagator developed by van Vleck [37] has been the basis of many practical advancements in semiclassical theory [11, 43, 111] and has been recently reviewed by Thoss and Wang [99] and by Kay [100]. In particular, a semiclassical initial value representation (SC-IVR) propagator was developed in 1984 by Herman and Kluk [39, 46, 47] which expresses the quantum time-propagation correlation function as a semiclassical expression in terms of coherent states. Unlike its predecessors, [37, 111] an initial value representation eliminates root search and singularity problems. Instead of finding all possible *paths* between two coordinate-space points, one only needs initial value information. This means the use of classical molecular dynamics *trajectories* is possible. The only other information required in addition to the classical trajectory itself is Hessian information from the dynamics.

In the last decade many developments in the SC-IVR method have been undertaken [45, 56–61, 102–105, 112–118]. Among them have been prescriptions for the calculation of vibrational states [56–62, 119], vibronic absorption spectra [102], reactive processes [112], quantum coherence [116], response functions [120] and internal conversion rates [121]. Over the past few years, research groups have investigated *ab initio* SC-IVR, where the trajectories are calculated on-the-fly. Tatchen and Pollak [102] computed the absorption spectrum of the $S_0 \rightarrow S_1$ transition of formaldehyde using the time-dependent density functional theory (TD-DFT) [122] method with the Perdew-Burke-Ernzerhof (PBE) [123] functional. They used a unity-valued Herman-Kluk prefactor to calculate the Herzberg-Teller correlation function. In 2009, Aspuru-Guzik and co-workers [60, 103] employed AIMD in the

study of the vibrational states of CO_2, which can be computed from the survival amplitude function. Here, they used the time-averaged variant of SC-IVR, which utilizes a significantly-reduced number of trajectories. Comparisons were made to states determined from fitted potential surfaces and the accuracy of state energies was examined. In a later study, they also calculated the eigenfunctions of CO_2 [104]. Since the Hessian is a vital part of an AIMD-SC-IVR study, effort have also been developed to reduce the number of Hessian evaluations, as shown by Hase *et al.* [105]. There have also been a number of other studies based on fitted PESs using SC-IVR to examine molecular vibrational states. Kaledin and Miller [61, 62] have obtained the vibrational states of H_2, H_2O, NH_3, CH_4, CH_2D_2 and H_2CO with SC-IVR as well as time-averaged SC-IVR [61]. Roy and co-workers [56–59, 114] developed a reduced-dimensionality approach through Cartesian geometric constraints [applying it to Ar_3 and $(H_2O)_2$], which is amenable for the computation of larger systems. The focus of this chapter is to determine accurate molecular vibrational states through a semiclassical approach.

Determination of vibrational state energies within the harmonic approximation is trivial for even very large systems. However, when anharmonic corrections are introduced, the computational effort is much more considerable. What is possible to do — through the use of classical-based dynamics — is to use spectral densities from *ab initio* SC-IVR to compute vibrational state energies. By incorporating terms accounting for probability amplitudes, SC-IVR reintroduces the quantum contribution into the classical simulation. Here, we provide further insight into *ab initio*-based SC-IVR using H_2CO as a model system and address several points that have not been considered in previous studies [56–58, 60–62, 103]. As opposed to time-averaged SC-IVR [61], we use standard SC-IVR (i.e., full phase space averaging) and an approximation of the Herman-Kluk prefactor. Previous work [62] has utilized reference wavefunctions chosen on the basis of symmetry, but here, we

separate them on a normal-mode basis. Careful analysis of the results as a function of the chosen reference wavefunction is done. We also demonstrate a practical tool for performing *ab initio* SC-IVR within the Molecular Modelling Toolkit (MMTK) [75], a molecular dynamics software package. The low-lying vibrational states of H_2CO are determined and compared to harmonic, quartic force field correlation-corrected vibrational self consistent field (cc-VSCF) [67], direct cc-VSCF [68, 124, 125], direct rectilinear-vibrational self-consistent field/vibrational configuration interaction with perturbation selected interactions-second order perturbation theory (VSCF/VCIPSI-PT2) as well as reference direct *curvilinear*-VSCF/VCIPSI-PT2 method results [63, 64].

Sec. 4.2 presents a brief review of the mathematical formulation of SC-IVR. Sec. 4.3 covers the details regarding the computation of the spectral density of H_2CO. In Sec. 4.3.1, we introduce the electronic structure methods used to produce the *ab initio* energies and frequencies. The most important component of the method is the phase space integral, which is obtained from the classical dynamics trajectories, as detailed in Sec. 4.3.2. The final spectral density depends largely on the reference wavefunction and so the prescription for determining the reference wavefunction and its overlaps are discussed in Sec. 4.3.3. Results and discussion of the obtained vibrational states follow in Sec. 4.4. Sec. 4.5 presents our final conclusions.

4.2 Theory

The quantum mechanical survival amplitude, $C(t)$, was introduced in Chapter 2:

$$C(t) = \left\langle \Psi | e^{-i\hat{H}t/\hbar} | \Psi \right\rangle . \tag{4.1}$$

This autocorrelation function has largest amplitude when $H - E = 0$. The Fourier transform of $C(t)$ generates the vibrational state energy peaks. That is, in ket

notation, its Fourier transform is

$$I(E) = \left\langle \Psi | \delta(\hat{H} - E) | \Psi \right\rangle, \tag{4.2}$$

which clearly indicates that peaks should occur at quantized states E_n. To solve this equation, the propagator is rewritten in Herman and Kluk's semiclassical formulation [39–42] mentioned previously in Sec. 2.2:

$$e^{-i\hat{H}t/\hbar} = (2\pi\hbar)^{-3N} \int\int d\mathbf{p}_0 d\mathbf{q}_0 R_{\mathbf{p}_0,\mathbf{q}_0,t} e^{iS_{\mathbf{p}_0,\mathbf{q}_0,t}/\hbar} |g_{\mathbf{p}_t,\mathbf{q}_t}\rangle\langle g_{\mathbf{p}_0,\mathbf{q}_0}|. \tag{4.3}$$

The integrals run over $\mathbf{p}_0$ and $\mathbf{q}_0$, which are the phase space variables. $R_{\mathbf{p}_0,\mathbf{q}_0,t}$ is the so-called Herman-Kluk (HK) prefactor stability matrix, $S_{\mathbf{p}_0,\mathbf{q}_0,t}/\hbar$ the classical action specifying the phase of the Gaussian wavepacket and the gs are coherent states. The prefactor (Eq. 2.28) contains numerous terms involving derivatives of the phase space variables. To numerically solve this with finite difference would require a very small timestep. The Johnson approximation (Eq. 2.34) avoids this by requiring only the local frequencies at each timestep along the trajectory. The coherent state representation of the minimum-uncertainty wavepacket ($|g_{\mathbf{p}_t,\mathbf{q}_t}\rangle$ and $\langle g_{\mathbf{p}_0,\mathbf{q}_0}|$) is a multivariate Gaussian function of coherent state width [39, 43, 44]

$$\gamma = 2L\alpha L^T, \tag{4.4}$$

where L is the eigenvector matrix and α the eigenvalue matrix from the Hessian. Coherent states have the property that the centre of the Gaussian evolves according to the classical equations of motion. Both the coherent states at the initial (0) and current (t) times are required. The coherent state may be expressed in terms of various representations (such as the position representation). Our form of the coherent state wavepacket is

$$\langle \mathbf{x} | g_{\mathbf{p}_t,\mathbf{q}_t} \rangle = \left(\frac{\gamma}{\pi}\right)^{3N/4} \exp\left[-\frac{\gamma}{2}(q_\mathrm{c} - q)^2 + \frac{i}{\hbar} p(q_\mathrm{c} - q)\right], \tag{4.5}$$

where c indicates the coherent state Gaussian is centered. The phase term, $e^{iS_{\mathbf{p}_0,\mathbf{q}_0,t}/\hbar}$, comes from the Lagrangian equations of motion. Combining Eqs. 4.1 and 4.3, we

obtain a semiclassical expression for the survival amplitude, i.e.,

$$C(t) = (2\pi\hbar)^{-3N} \int\int d\mathbf{p}_0 d\mathbf{q}_0 R_{\mathbf{p}_0,\mathbf{q}_0,t} e^{iS_{\mathbf{p}_0,\mathbf{q}_0,t}/\hbar} \langle \Psi_{\text{ref}} | g_{\mathbf{p}_t,\mathbf{q}_t} \rangle \langle g_{\mathbf{p}_0,\mathbf{q}_0} | \Psi_{\text{ref}} \rangle, \quad (4.6)$$

where the overlap of Ψ_{ref} with the coherent state produces:

$$\langle g_{\mathbf{p},\mathbf{q}} | \Psi_{\text{ref}} \rangle = \exp\left[-\frac{1}{4} (\mathbf{q} - \mathbf{q}_{\text{ref}})^T \gamma (\mathbf{q} - \mathbf{q}_{\text{ref}}) - \frac{1}{4\hbar^2} (\mathbf{p} - \mathbf{p}_{\text{ref}})^T \gamma^{-1} (\mathbf{p} - \mathbf{p}_{\text{ref}}) \right.$$
$$\left. + \frac{i}{2\hbar} (\mathbf{p} + \mathbf{p}_{\text{ref}})^T (\mathbf{q} - \mathbf{q}_{\text{ref}}) \right]. \quad (4.7)$$

$\mathbf{p}_{\text{ref}}$ and $\mathbf{q}_{\text{ref}}$ are the reference state mass-weighted momenta and positions, respectively. The overlaps have a general Gaussian form. The reference state constitutes a chosen "trial" wavefunction, which is the desired state of interest. $C(t)$ is the correlation of the state of the system with this reference function, meaning the chosen reference function serves as an "extractor" for eigenstates near it. Note that in practice, the above overlap is also symmetry-adapted, which will be explained in Sec. 4.3.3.

Now, the Fourier transform of this semiclassical survival amplitude gives the resultant power spectrum. That is,

$$I(\omega) = \frac{1}{2\pi} \int_{-\infty}^{\infty} dt \; e^{i\omega t} C(t) \quad (4.8)$$

produces the energy eigenvalues of the Hamiltonian $\hat{H}$. The intensities of the peaks are directly related to the choice of reference wavefunction.

4.3 Computational Methods

4.3.1 Electronic Structure and Harmonic Frequencies

In order to benchmark our SC-IVR approach, the *ab initio* electronic structure calculations were carried out at the HF/3-21G level of theory [14, 126] for ease of production. The equilibrium geometry of H_2CO is given in Table 4.1. Energies at which the simulation was run are far below that of the HF transition state (37,700

cm^{-1}) [127]. The availability of *analytic* gradients and Hessians, for the classical dynamics and HK prefactor evaluation, respectively, is a major asset and guided, along with its computational efficiency, the choice of the Hartree-Fock level of theory. In principle, any electronic structure theory methodology for which analytic gradients and Hessians are available can be utilized. Our calculations made use of the GAMESS-US 2007 and 2009 quantum chemistry packages [17].

Table 4.1: Equilibrium geometry of H_2CO at the HF/3-21G level of theory. Bond lengths are given in Å and the bond angle in degrees.

Parameter	Value
r_{CO}	1.207
r_{CH}	1.083
θ_{HCO}	122.5

4.3.2 Trajectories for Phase Space Average

To determine the initial conditions for the ensemble of trajectories, a Monte Carlo sampling of $M = 20{,}000$ sets of initial geometric configurations and momenta was produced, corresponding to a coherent state Gaussian wavepacket centered at the HF/3-21G equilibrium geometry and with zero momentum. The phase space sampled represents $|\langle g_{\mathbf{p}_0,\mathbf{q}_0}|\Psi_{\mathrm{eq}}\rangle|^2$, whose form is identical to that of Eq. 2.31.

The coordinate and momentum widths of Eq. 2.31 are $\sqrt{2/\gamma}$ and $\hbar\sqrt{2\gamma}$, respectively. Of these initial conditions, only motion in the $3N-6$ internal degrees of freedom is allowed, and so the original values are adjusted, fixing the molecule's centre of mass and spatial orientation. Note that only one set of initial conditions is used for the various reference wavefunctions and therefore, a re-weighting procedure is required (in other words, the integral over phase space isn't uniform). Eq. 4.6 can

be rewritten with the insertion of unity $\mathbb{1} = |\langle g_{\mathbf{p}_0,\mathbf{q}_0}|\Psi_{\mathrm{eq}}\rangle|^2/|\langle g_{\mathbf{p}_0,\mathbf{q}_0}|\Psi_{\mathrm{eq}}\rangle|^2$ as

$$C(t) = (2\pi\hbar)^{-3N} \int\int d\mathbf{p}_0 d\mathbf{q}_0 R_{\mathbf{p}_0,\mathbf{q}_0,t} e^{iS_{\mathbf{p}_0,\mathbf{q}_0,t}/\hbar} \times \langle \Psi_{\mathrm{ref}}|g_{\mathbf{p}_t,\mathbf{q}_t}\rangle\langle g_{\mathbf{p}_0,\mathbf{q}_0}|\Psi_{\mathrm{ref}}\rangle \frac{|\langle g_{\mathbf{p}_0,\mathbf{q}_0}|\Psi_{\mathrm{eq}}\rangle|^2}{|\langle g_{\mathbf{p}_0,\mathbf{q}_0}|\Psi_{\mathrm{eq}}\rangle|^2}. \tag{4.9}$$

The initial conditions essentially impose a bias of $|\langle g_{\mathbf{p}_0,\mathbf{q}_0}|\Psi_{\mathrm{eq}}\rangle|^2$ (the numerator in $\mathbb{1}$) in the phase space distribution which must be accounted for by division of the bias. The Monte Carlo estimate is therefore

$$C(t) = \frac{1}{M}\sum_{m=1}^{M}\left[R_{\mathbf{p}_0,\mathbf{q}_0,t} e^{iS_{\mathbf{p}_0,\mathbf{q}_0,t}/\hbar} \frac{\langle \Psi_{\mathrm{ref}}|g_{\mathbf{p}_t,\mathbf{q}_t}\rangle\langle g_{\mathbf{p}_0,\mathbf{q}_0}|\Psi_{\mathrm{ref}}\rangle}{\langle \Psi_{\mathrm{eq}}|g_{\mathbf{p}_0,\mathbf{q}_0}\rangle\langle g_{\mathbf{p}_0,\mathbf{q}_0}|\Psi_{\mathrm{eq}}\rangle}\right]_m. \tag{4.10}$$

This choice of sampling greatly reduces the computational cost as only one set of *ab initio* trajectories is required instead of a full phase space distribution.

Approximately 38% of the 20,000 generated initial geometries and momenta had a total energy less than 300 kJ/mol ($\sim$25,000 cm^{-1}). Initial conditions with energies above 300 kJ/mol were discarded. Energies below 300 kJ/mol place the molecule well below the transition state, which is important in the numerical stability of the Herman-Kluk prefactor. Additionally, the semiclassical survival amplitude, $C(t)$, was computed only when $|\langle g_{\mathbf{p}_0,\mathbf{q}_0}|\Psi_{\mathrm{eq}}\rangle|^2 > 10^{-10}$ (low overlap leads to negligible contribution to the average of the survival amplitude). From each of these initial conditions, a 244 fs constant energy molecular dynamics trajectory was determined using MMTK. These trajectories constitute the phase space average, which is the multidimensional integral in $C(t)$. The equations of motion were computed with Velocity-Verlet integration [30]. During the dynamics, the Hessian at each timestep (0.5 fs) was saved and diagonalized. The resultant eigenvalues are necessary for the calculation of the HK prefactor which requires the local harmonic zero point energy (ZPE) (see Eq. 2.34).

4.3.3 Reference Wavefunctions and Overlaps

The coherent state overlaps are functions of mass-weighted geometry and momentum. A choice of reference wavefunction where $\mathbf{q}_{\text{ref}}$ is located at the equilibrium geometry and $\mathbf{p}_{\text{ref}} = 0$, will produce the highest overlap with the lowest vibrational state (zero point energy). In all cases we choose $\mathbf{p}_{\text{ref}}$ to be zero, for simplicity, and we vary only $\mathbf{q}_{\text{ref}}$. The width is chosen to be γ as previously defined, meaning that Ψ_{ref} is the exact harmonic ground state wavefunction, and there is no appreciable overlap with any state other than the ground state. When another reference wavefunction is chosen, it will be those coherent states (i.e., phase space points along the trajectory) that have highest overlap with this wavefunction which will contribute the most to the survival amplitude. Fig. 4.1 demonstrates this graphically. One way to vary the wavefunction in order to obtain additional states is to apply a technique where the atoms are spatially displaced along a normal mode coordinate. As a result, it is easy to interpret the magnitude of displacement (c) with the energy put "into" a mode ν_j (in this work, we use ν to denote the mode itself). For instance, by letting $c = \sqrt{\hbar/\omega_j}$ displacement of mode ν_j, this means that the molecule has been displaced from equilibrium along ν_j and has $\frac{1}{2}\hbar\omega_j$ of potential energy (assuming the motion is perfectly harmonic). Essentially, this provides a vibrational excited state reference wavefunction. The normal modes are as assigned in Table 4.2. By allowing just single normal mode displacements, this should effectively produce a spectrum with peaks only at the fundamental frequencies and overtones, i.e., $(n_1 \cdots n_j \cdots n_N)$: $n_{j\neq k} = 0, n_k \in \mathbb{Z}_{>0}$.

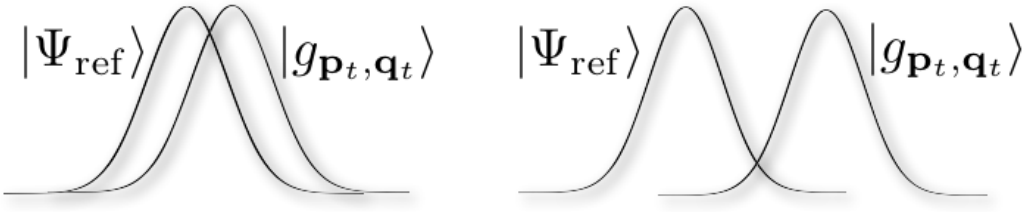

Figure 4.1: Correlation is highest when the coherent state (state at time t) is most similar to that of the reference state.

Table 4.2: Harmonic normal mode labelling and frequencies (cm^{-1}). Frequencies are determined at the HF/3-21G level of theory.

Mode	Assignment	Frequency
$\nu_1(A_1)$	CH_2 Symmetric Stretch	3162
$\nu_2(A_1)$	CO Stretch	1916
$\nu_3(A_1)$	CH_2 Scissor	1693
$\nu_4(B_1)$	CH_2 Wag	1337
$\nu_5(B_2)$	CH_2 Asymmetric Stretch	3233
$\nu_6(B_2)$	CH_2 Rock	1378

A Monte Carlo procedure is used to estimate the phase space integrals and therefore, all eigenstates can contribute to the survival amplitudes. The normal mode displacements in the reference wavefunction are also not pure symmetry states. To remedy this problem, we explicitly symmetrize the reference wavefunction. To do so, we project out specific symmetries by constructing a projection operator corresponding to a specific irreducible representation of the C_{2v} group. For the case of symmetric A_1 states, an unsymmetrized reference wavefunction, $|\Psi_{\rm ref}\rangle$, becomes,

$$|\Psi_{\rm ref}^{A_1}\rangle = \frac{1}{4}\left[\hat{E}|\Psi_{\rm ref}\rangle + \hat{C}_2|\Psi_{\rm ref}\rangle + \hat{\sigma}_v|\Psi_{\rm ref}\rangle + \hat{\sigma}'_v|\Psi_{\rm ref}\rangle\right]. \tag{4.11}$$

The use of the above wavefunction will ensure that energy levels of a specific symmetry are extracted (cf. Ref. [62], where a product of coherent states is used instead, with a symmetrizer to extract states of particular molecular symmetry).

Because the width γ (see Eq. 4.4) is identical to that of the ground state wavefunction, one may visualize the displaced reference wavefunction (prior to sym-

metrization) as simply a shift of the ground state wavefunction along a single normal mode coordinate. For a given mode j, the new atom positions in Cartesian coordinates is represented as the vector $\vec{x}^j$ (we call this x to differentiate this from the mass-weighted coordinate q). For each individual coordinate α, the elements of the vector $\vec{x}^j$ are:

$$x_\alpha^j = X_\alpha - c_j \frac{L_{\alpha j}}{\mu_\alpha}, \tag{4.12}$$

where X_α is an element of the Cartesian equilibrium geometry vector, μ_α is the square root of the mass of the atom associated with Cartesian component α, and $L_{\alpha j}$ is the eigenvector element associated with displaced mode ν_j. In this work, c_j is varied by a factor d to adjust the magnitude of the normal mode displacement ($c_j = d \cdot \sqrt{\hbar/\omega_j}$).

4.4 Results and Discussion

Here, we present the results of the calculation of the spectral density of H_2CO as determined by SC-IVR. The SC-IVR solution of $C(t)$ by Eq. 4.10 leads to a signal which decays rapidly (see Fig. 4.2 for an example). This shows that the the total simulation length, T, is satisfactory. The peaks of the spectral density are the low-lying vibrational eigenstates. It is possible for SC-IVR to determine more states, albeit at a substantial cost of more trajectories. The survival amplitude would improve. In this particular case, since the correlation function decays to a great extent within the timespan of the simulation, a longer trajectory would make minimal difference in the spectra. The symmetry-adapted reference wavefunction of Eq. 4.11 is used for all the SC-IVR results. The SC-IVR values are compared to the harmonic approximation, cc-VSCF/2MR-QFF, direct-cc-VSCF, (rectilinear) VSCF/VCIPSI-PT2 and curvilinear-VSCF/VCIPSI-PT2 methods[1] described earlier

[1]The main contribution by D.M. Benoit to the current study were the calculations with the VSCF/VCI methods.

in Chapter 2 (Sec. 2.7). While vibrational states in the harmonic approximation are trivially obtained to the n^{th} state, anharmonic terms are increasingly difficult to compute. In all four VSCF implementations, only two-mode couplings were utilized and three-mode (and higher) couplings were neglected. To make sure that the VSCF results used in the the VSCF/VCIPSI-PT2 methods are fully converged, we include up to 4-mode excitations in the VCI basis and allow up to 8-quanta excitation per mode. This leads to a large vibrational basis (about 70,000 states) that is more appropriate for describing combination bands and overtones. Given the large size of the basis, we performed the calculations with a slightly different technique than VCI called vibrational configuration interaction with perturbation selected interactions-second-order perturbation (VCIPSI-PT2). It has been shown [64] that this method gives virtually the same results as a standard VCI/VSCF calculation. Of the four reference calculation types being considered, the curvilinear approach is the most accurate.

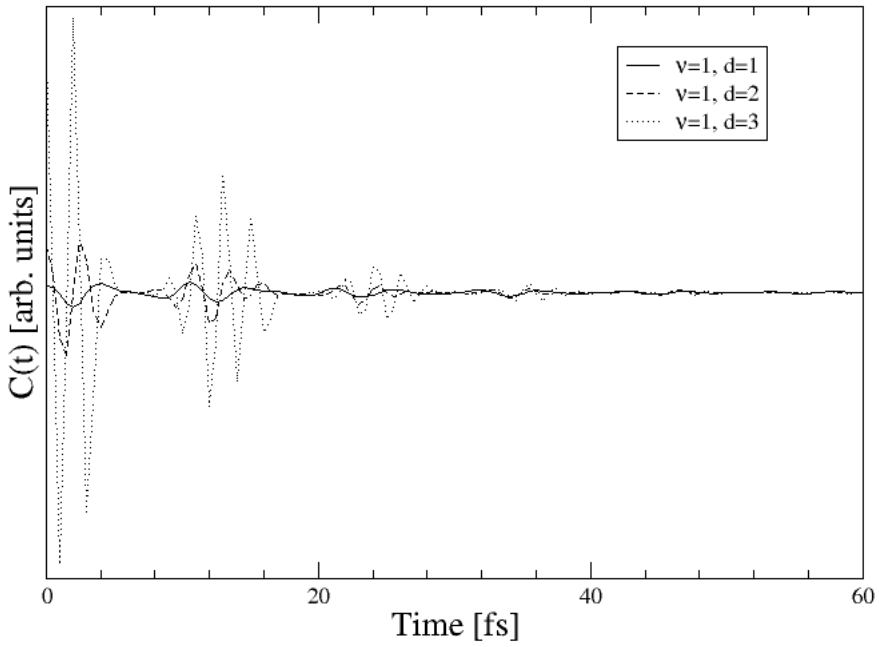

Figure 4.2: Correlation functions where the ν_1 mode is displaced by various amounts d when constructing the reference wavefunction. The signal decays after very short time.

As detailed in Sec. 4.2, we use an alternate form of the Herman-Kluk prefactor. Johnson's approximation [54] has been shown to be effective for weakly-bound systems [56–59]. This approximation eliminates branch cut problems as well as the need to calculate phase space derivatives. Instead, one only needs to calculate the Hessian matrix at each geometry along the trajectories. Diagonalization of the Hessian matrix gives the eigenvalues, whose square roots are the *local* harmonic frequencies. These ω_js are similar to frequencies calculated at stationary points (i.e., at the equilibrium or transition state geometries). Since the frequencies are calculated at any point on the potential energy surface, they are naturally complex-valued. The consequence is a highly-oscillatory exponential term that increases noise in the survival amplitude function. In Fig. 4.3, we present results comparing spectra

obtained with Johnson's WKB approach along with several further approximations. Issack and Roy [56–59] took the approach of taking the absolute value of all the frequencies ($|\omega|$) to eliminate the oscillating phase. This simplification results in a larger magnitude term in the exponential of Eq. 2.34 since it is taking a sum over additional positive real numbers. The HK prefactor, $R_{\mathbf{p}_0,\mathbf{q}_0,t}$, becomes a larger negative complex exponent. This appears to lead to overestimating the energy of the vibrational states (see Fig. 4.3). As well, the decay of the survival amplitude is much slower. Alternatively, if one encounters an imaginary frequency, one can simply neglect it, so that only the real frequencies are taken into account ($\omega \in \mathbb{R}$). The different summations do provide minor differences in the spectral density, with the peak positions between $\omega \in \mathbb{R}$ and a complex ω being negligible. In fact, $\omega \in \mathbb{C}$ appears to reduce signal noise. However, the signal intensity of the peaks is slightly diminished compared to $\omega \in \mathbb{R}$. The difference between the use of complex-, real- or absolute-valued frequencies can be in the tens of wavenumbers, which may be significant for the accuracy of SC-IVR, although the width of the spectral peaks is comparable to the shift due to the type of prefactor. In the present work, we see no reason not to use the complex-valued frequencies, since there appears to be no benefit in simplifying the WKB approximation further (whether it is more difficult to converge the prefactor in other systems, such as weakly-bound complexes, warrants further investigation). In all the following calculations we maintain the complex value of the frequencies ($\omega \in \mathbb{C}$). Note that all 12 eigenvalues of the Hessian are non-zero, including the rotational and translational modes. As seen in Eq. 2.34, the summation is only over $3N - 6$ modes (cf. previous literature), so the extraneous non-vibrational frequencies must be removed in the prefactor evaluation — we do so in the present work by neglecting the 6 lowest magnitude frequencies.

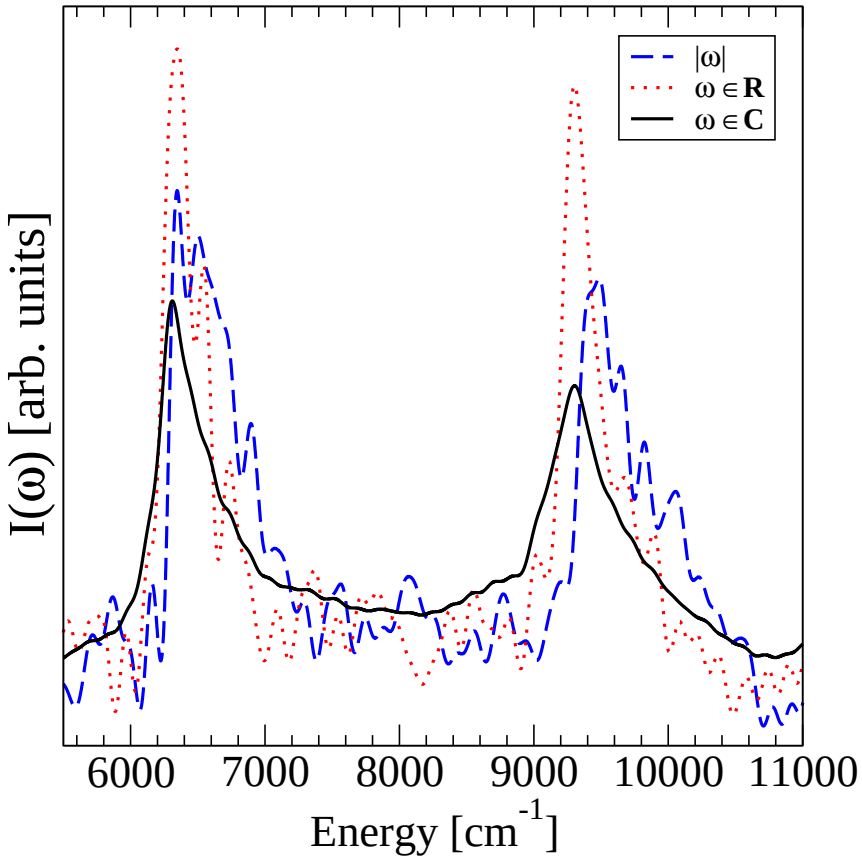

Figure 4.3: Variation of the spectral density (displaced in ν_1) with respect to the type of HK prefactor used. The dashed (blue) line indicates use of the absolute value of ω, the dotted (red) line sums only the positive frequencies and the solid (black) line has a complex-valued ω (no further approximations).

Following Sec. 4.3.3, we examine the spectral density as a function of the reference state chosen. We show the results of simulations with normal mode displacements along the A_1 modes of vibration, ν_1, ν_2 and ν_3. Since the wavefunction is symmetry-adapted for A_1, in theory, all A_1 vibrational states should be obtained. Yet, as solely the A_1 normal modes are excited, we only expect to obtain their fundamentals, overtones and, to a certain extent, their combination bands, the others being of negligible amplitude.

The spectral density as determined by SC-IVR is shown in Fig. 4.4. Three values of configurational displacement along the normal mode (magnitude specified by d), are shown. As can be seen, the further the reference wavefunction is displaced from the equilibrium geometry, the larger the overlap with higher energy states. Therefore, increasing the reference wavefunction displacement is a systematic way to determine vibrational states of increasing energy. The ground state (000000) is resolved in all figures. Each of the curves in Figs. 4.4(a), (b) and (c) resolves one set of vibrational states ($\cdots n \cdots$) due the overlap with a single normal mode (in the harmonic limit). The benefit of such "filtering" is that a cleaner spectrum is obtained, so that close-lying eigenstates are unequivocally differentiated. Spectral noise and uncertainty are major issues for many-dimensional systems and states of higher excitation. The intensities in Fig. 4.4(a) have the broadest peaks because the reference wavefunction energy (i.e., displacement) is largest, since it is proportional to ω_1. It is more difficult to extract states higher in energy (phase space coverage decreases, meaning the overlap term is often zero and therefore has no contribution to the overall survival amplitude integral). Table 4.3 lists the A_1 fundamental and overtone vibrational state peak positions up to 4-quanta excitation and also the mean absolute errors and root mean square deviations as compared to curvilinear-VSCF/VCIPSI-PT2. The assignments are quite close to the curvilinear bound state calculations (vertical lines) for low excitation, and, in general, are well within 100 cm^{-1}. As expected, errors and deviations become larger as one goes higher in energy. The results show that the SC-IVR results are systematically more accurate than the cc-VSCF/2MR-QFF (i.e., a VSCF-type method), direct cc-VSCF and the rectilinear-VSCF/VCIPSI-PT2 (i.e., a VSCF/VCI method) results when compared to the more accurate curvilinear-VSCF/VCIPSI-PT2 reference calculations.

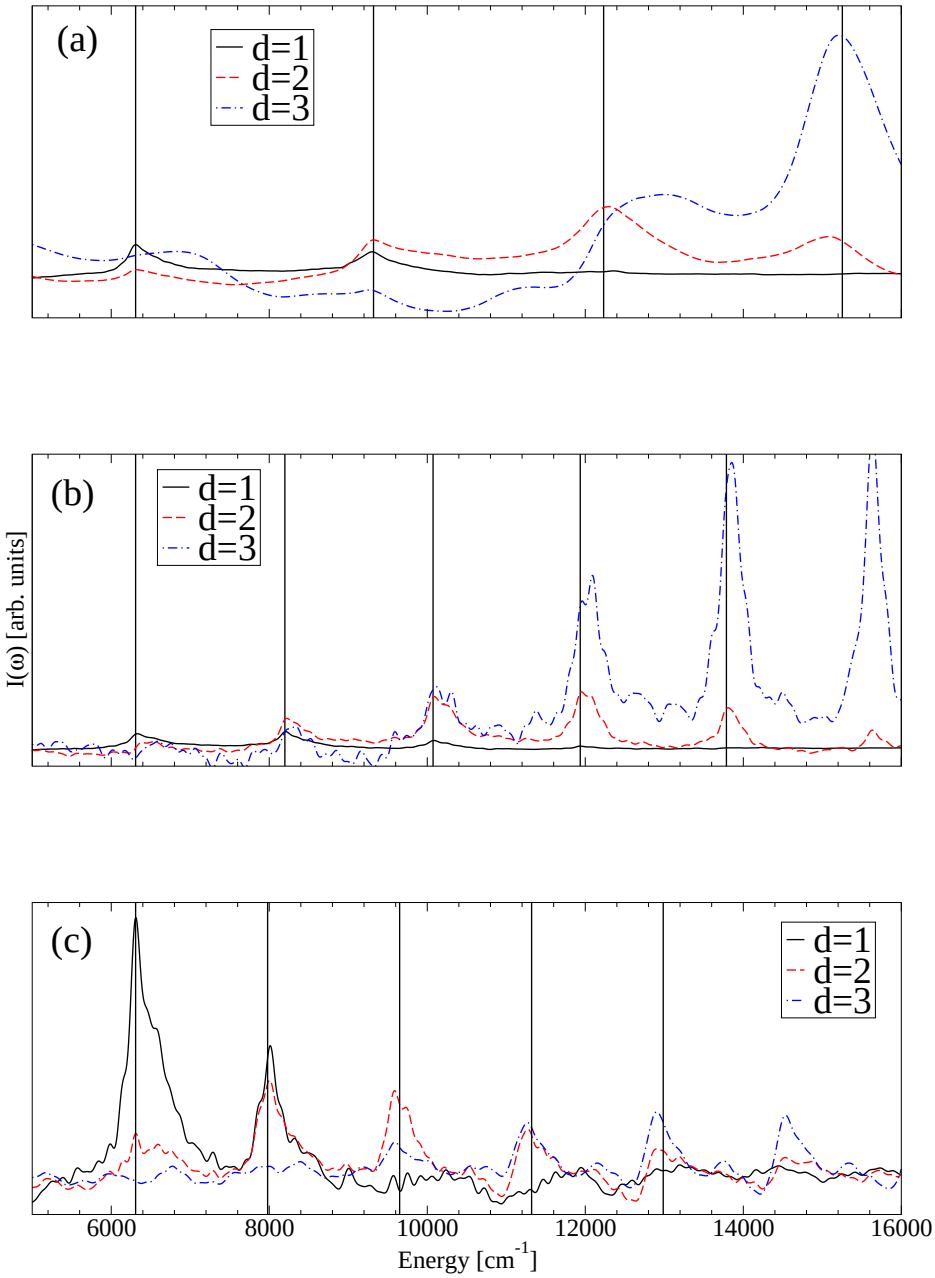

Figure 4.4: Intensity (spectral density) plots from SC-IVR given symmetry-adapted reference state overlaps with displacements along the three A_1 normal modes, (a) ν_1, (b) ν_2 and (c) ν_3, respectively. The curves are the SC-IVR results. d represents the magnitude of displacement (energy $\propto d^2$) of each mode (see text for details). The vertical lines represent the curvilinear-VSCF/VCIPSI-PT2 reference bound state calculation. In each panel, the leftmost vertical line represents the ground vibrational state (000000), and in the case of the first panel, the subsequent lines are the (100000), (200000), (300000) and (400000) vibrational states. The other two panels are similarly labelled.

Table 4.3: Fundamental vibrational states involving the A_1 normal modes of H_2CO at the HF/3-21G level as determined using various computational methods. Units are in cm^{-1}. The SC-IVR values were determined by the location of the point of the highest intensity peak of one or more spectra (average), where each point was separated by < 0.5 cm^{-1}. The mean absolute error (MAE) and root mean square deviation (RMSD) with respect to the curvilinear-VSCF/VCIPSI-PT2 method are shown for the fundamental overtones.

State	Harmonic	cc-VSCF/2MR-QFF	direct cc-VSCF	VSCF/VCIPSI-PT2	curvi-VSCF/VCIPSI-PT2	SC-IVR
(000000)	6360	6271	6268	6268	6309	6311
(100000)	9522	9265	9254	9251	9320	9303
(010000)	8276	8155	8152	8152	8198	8208
(001000)	8053	7924	7922	7921	7980	8013
(200000)	12685	12183	12136	12259	12232	12297
(020000)	10191	10029	10024	10023	10074	10089
(002000)	9745	9574	9571	9571	9650	9587
(300000)	15847	15071	14955	15103	15254	15209
(030000)	12107	11893	11885	11881	11936	11961
(003000)	11438	11164	11216	11216	11321	11269
(400000)	19010	—	17721	17938	17996	17848
(040000)	14022	—	13735	13727	13787	13853
(004000)	13131	—	12851	12851	12986	12904
MAE	257	74	104	72	—	48
RMSD	370	89	133	80	—	61

Figs. 4.5, 4.6 and 4.7 show spectral densities consisting of reference state displacements of two modes simultaneously. That is, they are a linear combination of single mode displacements. Like those of Fig. 4.4, the fundamental bands are obtained, although with somewhat less accuracy. Many combination bands are also visible, although given the width of the peaks and that they are often near other states, assignments can be made with less certainty. In most cases, the location of the highest peak was the value tabulated in Table 4.4 and if the peaks were clearly defined or equally ambiguous in more than one spectrum, the average of these locations were chosen. This uncertainty may be rectified with a more detailed procedure of displacing the reference wavefunction (here, we place a single quanta of energy into each normal mode) and potentially increasing the number of trajectories involved in the calculation.

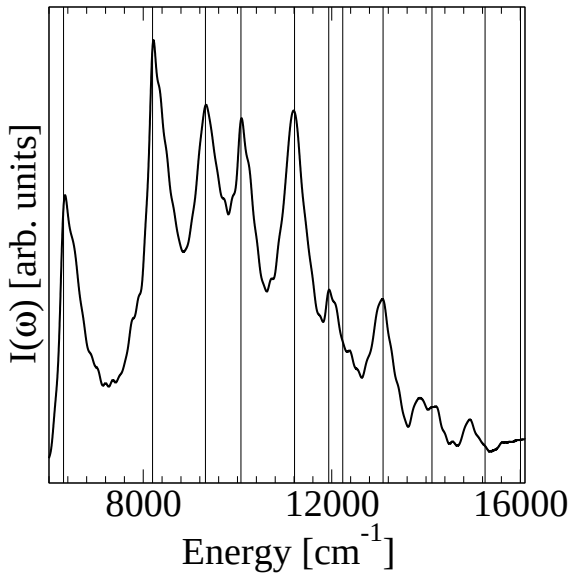

(a)

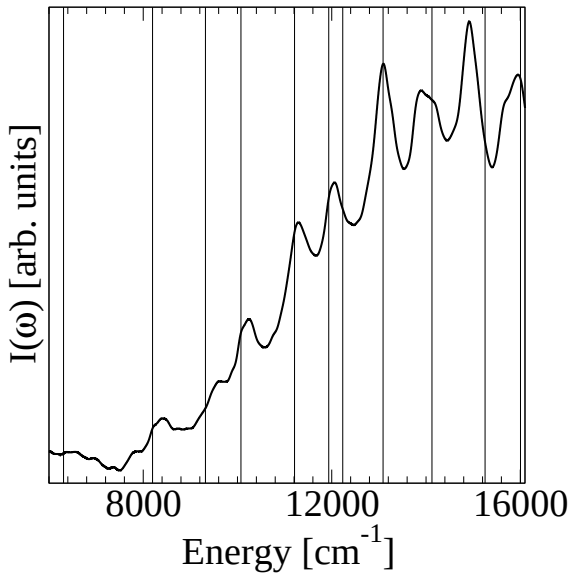

(b)

Figure 4.5: Spectral density plots where the ν_1 and ν_2 A_1 modes are displaced simultaneously when constructing the reference wavefunction. The vertical lines represent the reference curvilinear-VSCF/VCIPSI-PT2 values (see Table 4.3 for labelling.) (a) $d = 1$, (b) $d = 2$

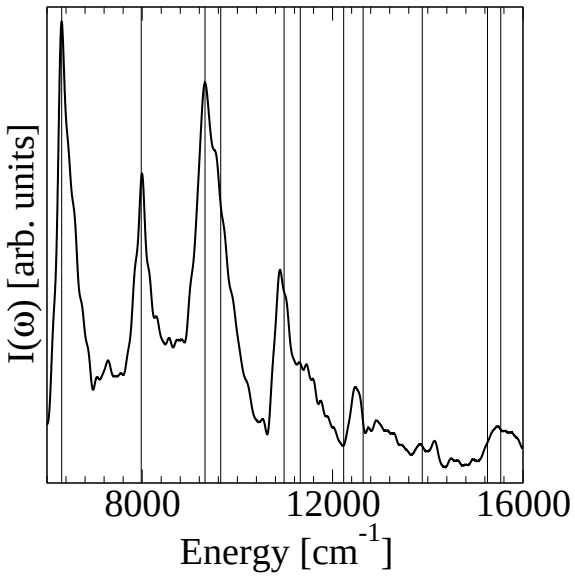

(a)

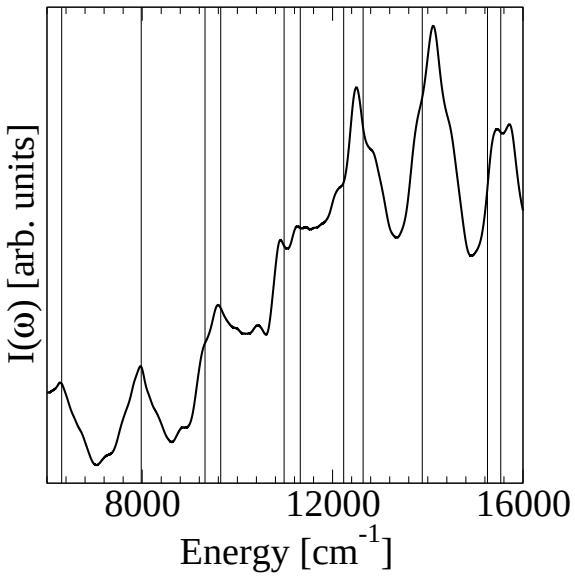

(b)

Figure 4.6: Spectral density plots where the ν_1 and ν_3 A_1 modes are displaced simultaneously when constructing the reference wavefunction. The vertical lines represent the reference curvilinear-VSCF/VCIPSI-PT2 values (see Table 4.3 for labelling.) (a) $d = 1$, (b) $d = 2$

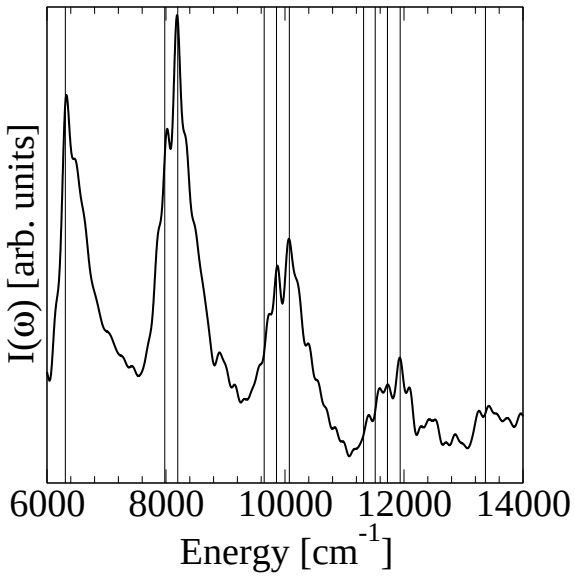

(a)

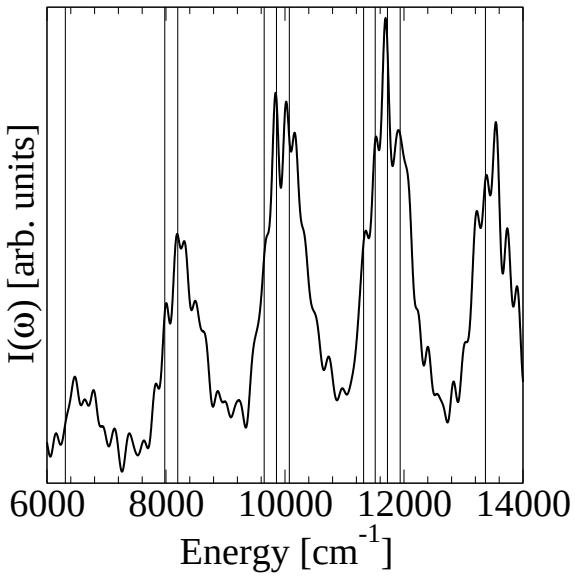

(b)

Figure 4.7: Spectral density plots where the ν_2 and ν_3 A_1 modes are displaced simultaneously when constructing the reference wavefunction. The vertical lines represent the reference curvilinear-VSCF/VCIPSI-PT2 values (see Table 4.3 for labelling.) (a) $d = 1$, (b) $d = 2$

Table 4.4: Vibrational combination states involving the A_1 normal modes of H_2CO at the HF/3-21G level as determined using various computational methods. Units are in cm^{-1}. The SC-IVR values were determined by the location of the point of the highest intensity peak of one or more spectra (average), where each point was separated by $< 0.5\ cm^{-1}$. Values with a (*) indicate that the assignment is uncertain.

State	Harmonic	cc-VSCF-2MR-QFF	cc-VSCF	VSCF/VCIPSI-PT2	curvi-VSCF/VCIPSI-PT2	SC-IVR
(110000)	11438	11164	11133	11126	11211	11191
(210000)	14600	14072	14006	14120	14126	14055*
(120000)	13354	13025	12997	12987	13088	13086
(220000)	16516	—	15860	15967	16004	15952
(101000)	11215	10913	10885	10876	10981	10896
(201000)	14377	13795	13735	13844	13884	14115
(102000)	12908	12525	12511	12498	12642	12488*
(202000)	16070	—	15329	15430	15533	15591*
(011000)	9968	9801	9805	9794	9858	9858
(021000)	11884	11665	11672	11653	11722	11690
(012000)	11661	11439	11453	11432	11517	11562
(022000)	13576	—	13316	13279	13370	13544*

4.5 Concluding remarks

We have shown, using *ab initio* trajectory data, that the vibrational eigenstates of H_2CO can be determined with reasonable accuracy through the use of SC-IVR and that it is systematically more accurate than VSCF and VSCF/VCI methods. The curvilinear-VSCF/VCIPSI-PT2 bound state approach is used as our exact reference. Our semiclassical description comes at an acceptable computational cost, but does have limitations. The vibrational states determined are highly sensitive to the reference wavefunction chosen. As such, for a complete description of a range of eigenstates, multiple carefully-constructed reference wavefunctions are required to extract them. In this work, we chose symmetry-adapted reference wavefunctions that had excitations along 1 and 2 normal modes only. This prescription allows us to independently and accurately determine fundamental states and some two-state combination bands of A_1 symmetry. This symmetrizing enables easier assignment of states. The major bottleneck in these simulations is the trajectory and Hessian computation. However, once done, the phase space average for the survival amplitude is readily calculated. An important outcome of the present study is that in utilizing our newly proposed phase space re-weighting procedure, only a *single* set of *ab initio* trajectories is required to obtain several power spectra.

In addition, we have examined the various implementations of Johnson's WKB approximation for the calculation of the HK prefactor. We have concluded that the local harmonic frequencies require no further simplification (i.e., can remain complex) since, at least in the case of H_2CO, it is not computationally advantageous. SC-IVR is an effective method for determining energy levels beyond the harmonic limit. However, it remains to be seen whether results would be as accurate for a more anharmonic system: at low energy, H_2CO is very harmonic. Therefore, the resolution of the data is a significant factor if the anharmonic correction for the eigenstates lies within the width of the spectral peaks. As anharmonicity increases,

it may also be more difficult to obtain accurate results due to the nature of the method (especially with the harmonic WKB approximation). However, previous results on the strongly anharmonic water dimer suggest that the approximation is reasonable [58, 59]. The challenge in obtaining higher excitations is another limitation, yet the solution might be simply increasing the number of trajectories. How many more remains to be investigated. *Ab initio* SC-IVR appears promising for extracting some quantum effects in molecular systems and its practicality will be important for larger molecules where full quantum simulations are not currently possible.

Chapter 5

Time-Averaged Semiclassical Initial Value Representation

5.1 Introduction

In the previous chapter, the survival amplitude was in the form of a phase space integral over the semiclassical propagator. The phase space integral allows for a delocalized view of the wavepacket in terms of an ensemble of localized trajectories. The grid of this integral must be fine enough for convergence. As indicated in Eq. 4.10, the initial conditions of the trajectories are obtained through Monte Carlo sampling. In the SC-IVR approach, for each timestep of each trajectory, we are required to compute the potential energy and Hessian matrix (and in our case, followed by diagonalization). Given that thousands of trajectories are needed for convergence for each degree of freedom [105], an improvement whereby some of those values are reused is highly desired. In Sec. 2.6, the *time-averaged* SC-IVR technique was introduced [61, 128].

The Liouville theorem states that along a trajectory, the phase space distribution function is uniform. The ergodic principle, coming from this, states that given enough time, a system will occupy all possible configurations. That is, a long time average will equal a (uniform) phase space average. A time average will cover all of

phase space that is energetically accessible. Mathematically, this is

$$\int\int d\mathbf{p}_0 d\mathbf{q}_0 \rightarrow \lim_{T\rightarrow\infty} \frac{1}{T}\int_0^T dt. \tag{5.1}$$

The integrals over phase space $(\mathbf{p}_0, \mathbf{q}_0)$ are eliminated and replaced by a time integral. This is valid provided that T is long enough to sample well phase space.

Kaledin and Miller [61, 62] previously drew the same conclusion by explicitly realizing that $(\mathbf{p}_0, \mathbf{q}_0) \rightarrow (\mathbf{p}_t, \mathbf{q}_t)$. They show that the correlation function (spectral density) now becomes

$$\begin{aligned} C_{\text{TA}} &= \int\int d\mathbf{p}_0 d\mathbf{q}_0 \, \frac{1}{T}\int_0^T dt A(\mathbf{p}_t, \mathbf{q}_t) \\ &= \frac{1}{T}\int_0^T dt \, \int\int d\mathbf{p}_0 d\mathbf{q}_0 A(\mathbf{p}_t, \mathbf{q}_t), \end{aligned} \tag{5.2}$$

where A is the integrand. Liouville's theorem then makes the following substitution:

$$C_{\text{TA}} = \frac{1}{T}\int_0^T dt \, \int\int d\mathbf{p}_t d\mathbf{q}_t A(\mathbf{p}_t, \mathbf{q}_t). \tag{5.3}$$

But, the double integral is equivalent to the standard full phase space SC-IVR equation. So,

$$\begin{aligned} C_{\text{TA}} &= C\frac{1}{T}\int_0^T dt \\ &= C. \end{aligned} \tag{5.4}$$

If Liouville's substitution applies for this equation, then time-averaged SC-IVR is equivalent to SC-IVR. One may note, however, that the Liouville theorem applies to a uniform phase space average. In practice, a uniform phase space average is not the case. The first time-averaged expression of the IVR equation is due to Kay *et al.* [128]. Specifically, they took the full SC-IVR equation:

$$\begin{aligned} C(t_2) = (2\pi\hbar)^{-3N}\int\int d\mathbf{p}_0 d\mathbf{q}_0 \frac{1}{T_{\text{corr}}}\int_0^{T_{\text{corr}}} dt_1 R_{\mathbf{p}_{t_1},\mathbf{q}_{t_1},t_2} \\ \times e^{iS_{\mathbf{p}_{t_1},\mathbf{q}_{t_1},t_2}/\hbar}\langle\Psi_{\text{ref}}|g_{\mathbf{p}_{t_2},\mathbf{q}_{t_2}}\rangle\langle g_{\mathbf{p}_{t_1},\mathbf{q}_{t_1}}|\Psi_{\text{ref}}\rangle, \end{aligned} \tag{5.5}$$

where N is the number of atoms, T_{corr} the correlation time of each segment, $R_{\mathbf{p}_{t_1},\mathbf{q}_{t_1},t_2}$ the Herman-Kluk prefactor in Eq. 2.28, $S_{\mathbf{p}_{t_1},\mathbf{q}_{t_1},t_2}/\hbar$ the classical action in Eq. 2.29, Ψ_{ref} the reference wavefunction, and $|g_{\mathbf{p},\mathbf{q}}\rangle$ the coherent states. The time variables are now t_1 and t_2, denoting the beginning and current time, respectively. Here, the problem seems to be more complicated with the extra time integral, but it is, in fact, easier (faster) to compute. Looking back at Fig. 2.2 as reference, the above equation implies that fewer trajectories are computed (fewer points of $\mathbf{p}_0$ and $\mathbf{q}_0$). Each trajectory is divided up into correlation *segments* whereby for each segment, a correlation function is obtained. Therefore, there are still many correlation functions to average over, but, since each segment overlaps with adjacent segments, there is an improved signal with less overhead. It has been stated that spectra up to 1 cm^{-1} in precision can be achieved [129].

In the limiting case where only *one* trajectory is used, the integral over phase space completely disappears. The phase space average is replaced by a very long trajectory which can be divided into many segments. The attractiveness of the single-trajectory approach is that it dramatically reduces the total number of dynamics steps needed to be computed. An additional benefit to single-trajectory SC-IVR is reported in Ref. [62]; the averaging over multiple segments smooths out the correlation function, leading to considerably sharper spectral peaks. The reason why the correlation function is smoother is because of the numerical stability of the HK prefactor.

As with a standard full SC-IVR calculation, the Herman-Kluk prefactor may be rewritten in a more concise form or approximated (discussion in Sec. 2.5). To restate, the form of the HK prefactor we use is the Johnson WKB approximation:

$$R_{\mathbf{p}_{t_1},\mathbf{q}_{t_1},t_2} = \exp\left[-\frac{i}{\hbar}\int_{t_1}^{t_2} dt' \sum_{j=1}^{3N-6} \frac{\hbar\omega_j(t')}{2}\right], \tag{5.6}$$

The following section is an analysis of the single-trajectory time-averaged SC-

IVR methods, using the H_2CO system, which can be compared directly with the results of the previous chapter.

5.2 Single-Trajectory Simulations on H_2CO

In a single-trajectory SC-IVR calculation, much thought should be taken into choosing the trajectory (after all, the assumption is that time-averaged SC-IVR is equivalent to a full phase space average), meaning the trajectory should cover a similar or equivalent phase space area. Analogous to the work of the previous chapter, energy is imparted into one of the normal mode coordinates. We give each trajectory an initial displacement along a single normal mode. The initial momentum for all atoms is set to zero. The trajectory coherent state is thus

$$|\mathbf{p}_0, \mathbf{q}_0\rangle = |\mathbf{p} = 0, \mathbf{q} = \text{normal mode displacement}\rangle. \tag{5.7}$$

The range of energies go from zero to a little over the total zero point energy. To examine the area of the potential sampled with such a trajectory, one examines the PES along 1-D cuts of the potential. Figs. 5.1-5.6 show the potential energy cuts (HF/3-21G) along all six vibrational modes, ν_i, while keeping the other coordinates fixed at equilibrium. The horizontal red line represents the zero point energy. The other lines are various vibrational states and includes the transition state [127]. These vibrational state values come from the curvilinear-VSCF/VCIPSI-PT2 results from Table 4.3. A subset of that table is shown below:

Table 5.1: Fundamental vibrational states involving the A_1 normal modes of H_2CO at the HF/3-21G level. Units are in cm^{-1}.

State	Harmonic	Curvilinear-VSCF/VCIPSI-PT2 [130]	Full SC-IVR [130]
(000000)	6360	6309	6311
(100000)	9522	9320	9303
(010000)	8276	8198	8208
(001000)	8053	7980	8013
(200000)	12685	12232	12297
(020000)	10191	10074	10089
(002000)	9745	9650	9587
(300000)	15847	15254	15209
(030000)	12107	11936	11961
(003000)	11438	11321	11269
(400000)	19010	17996	17848
(040000)	14022	13787	13853
(004000)	13131	12986	12904

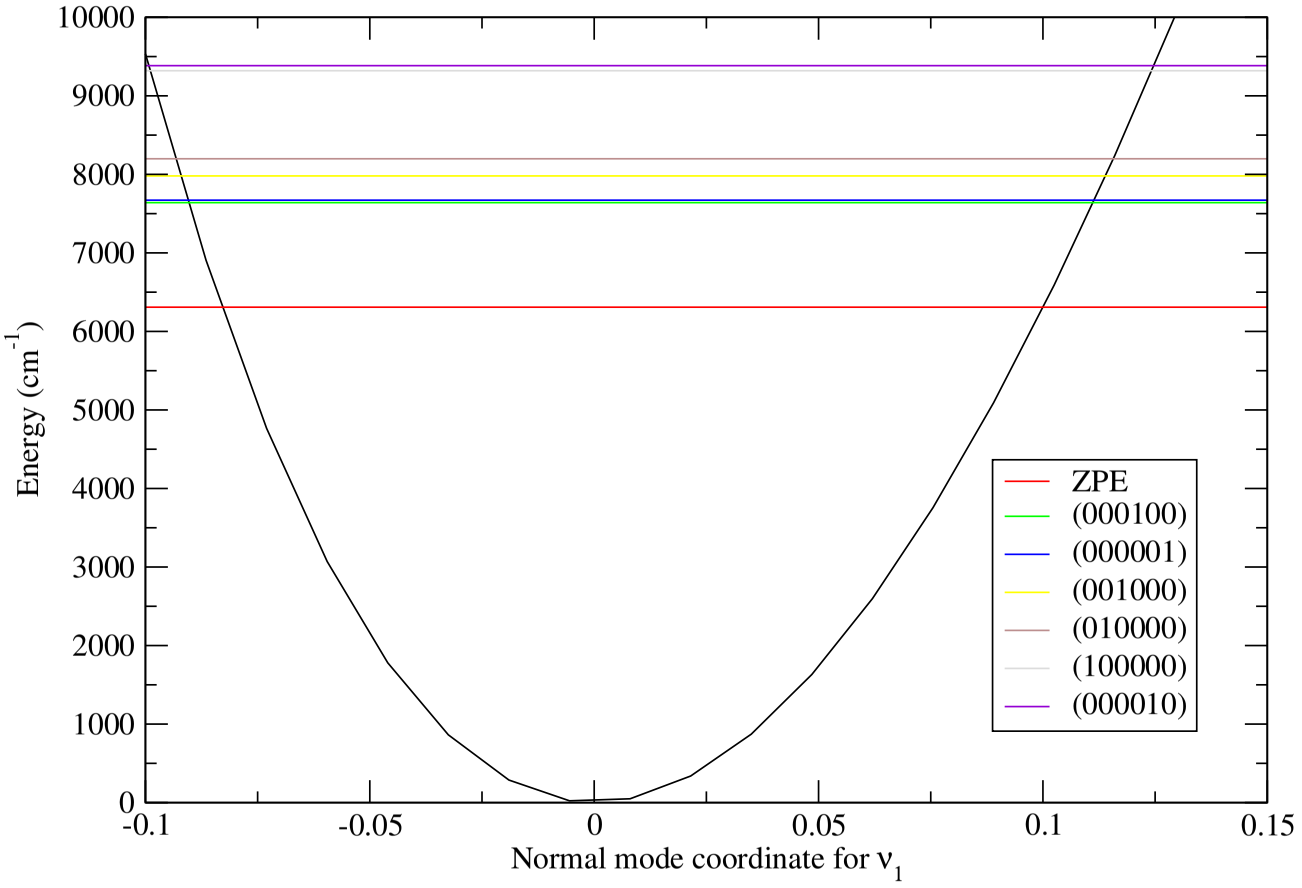

Figure 5.1: PES cut along the normal mode coordinate ν_1 of H_2CO. The horizontal lines represent the first few vibrational states calculated with VSCF/VCIPSI-PT2.

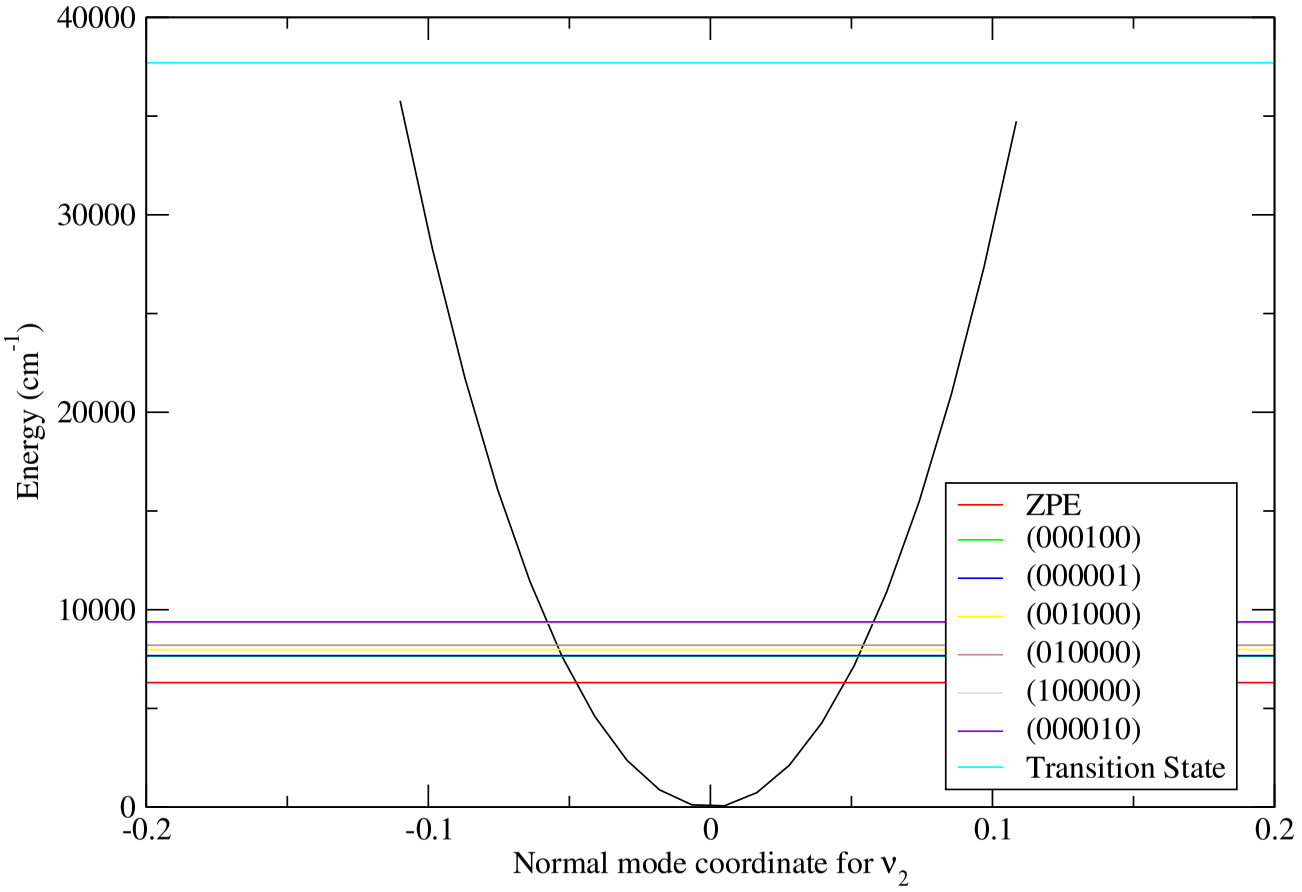

Figure 5.2: PES cut along the normal mode coordinate ν_2 of H_2CO. The horizontal lines represent the first few vibrational states calculated with VSCF/VCIPSI-PT2.

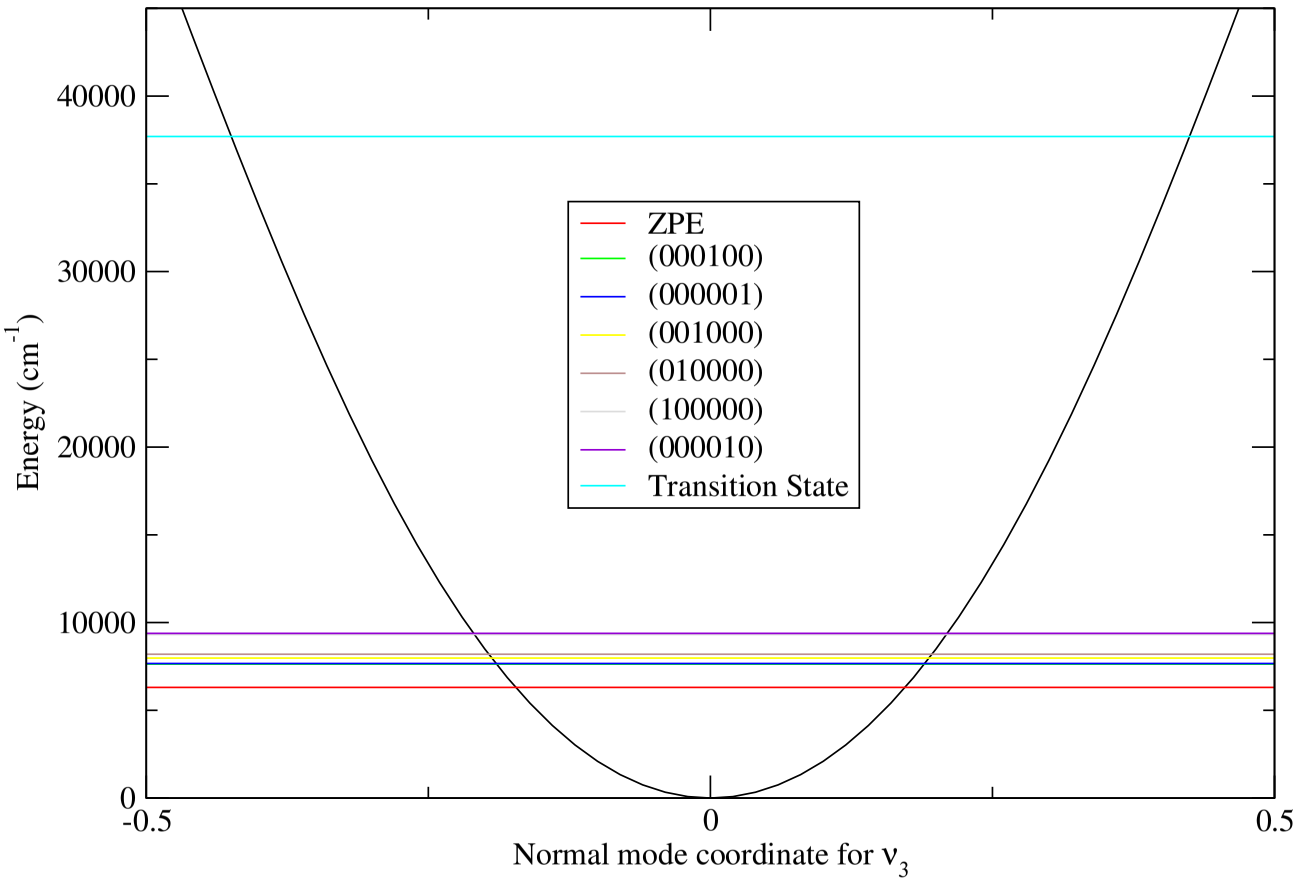

Figure 5.3: PES cut along the normal mode coordinate ν_3 of H_2CO. The horizontal lines represent the first few vibrational states calculated with VSCF/VCIPSI-PT2.

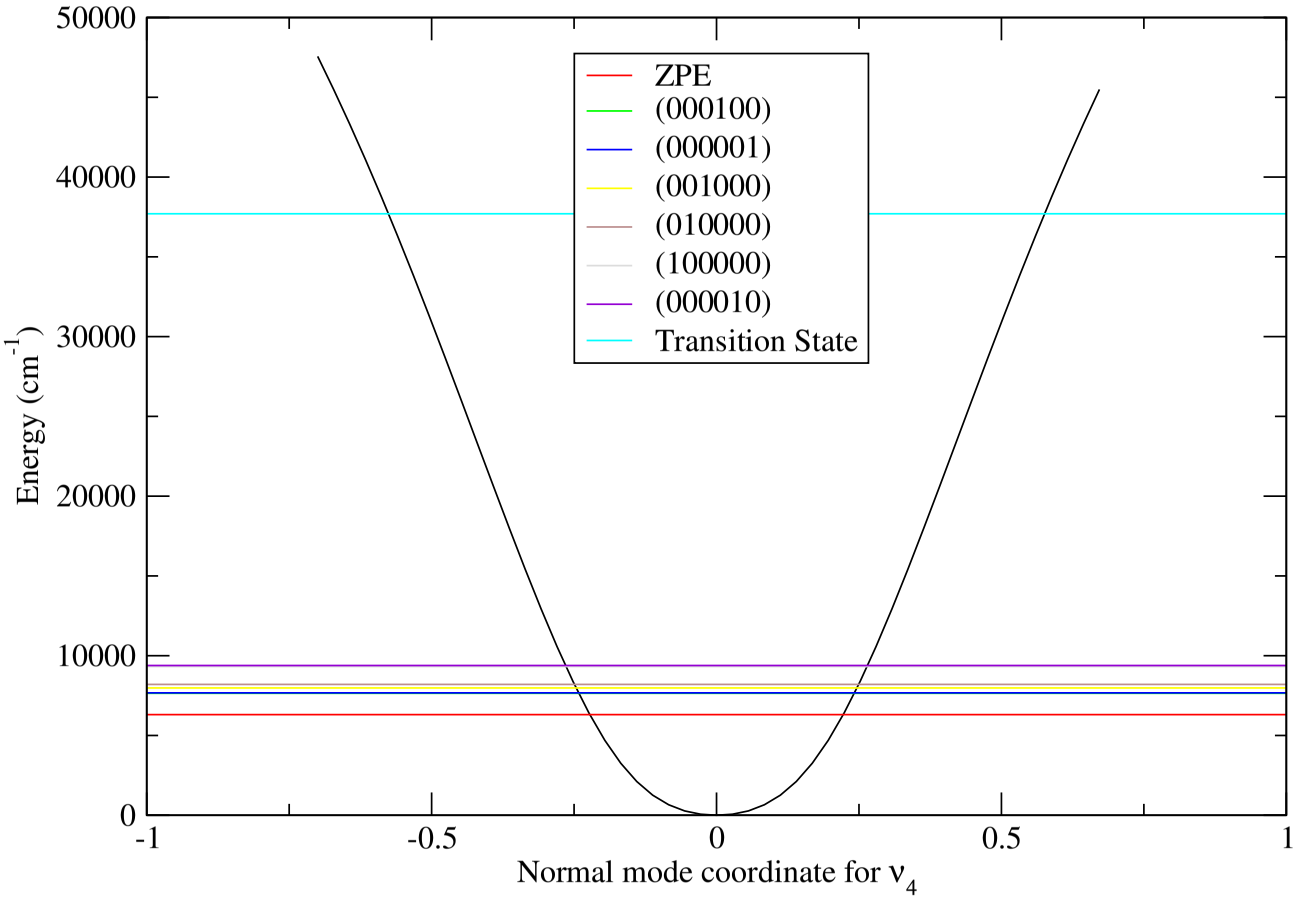

Figure 5.4: PES cut along the normal mode coordinate ν_4 of H_2CO. The horizontal lines represent the first few vibrational states calculated with VSCF/VCIPSI-PT2.

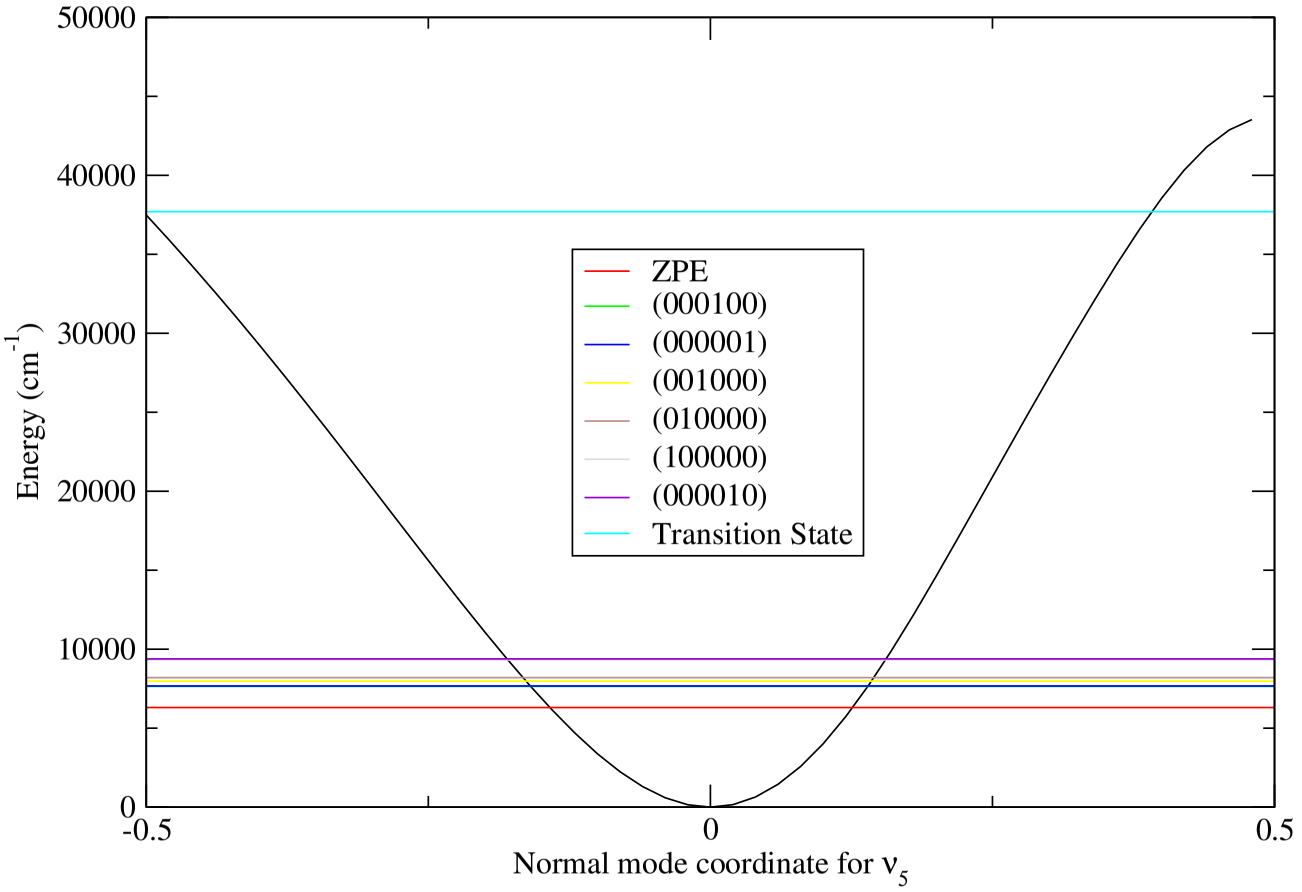

Figure 5.5: PES cut along the normal mode coordinate ν_5 of H_2CO. The horizontal lines represent the first few vibrational states calculated with VSCF/VCIPSI-PT2.

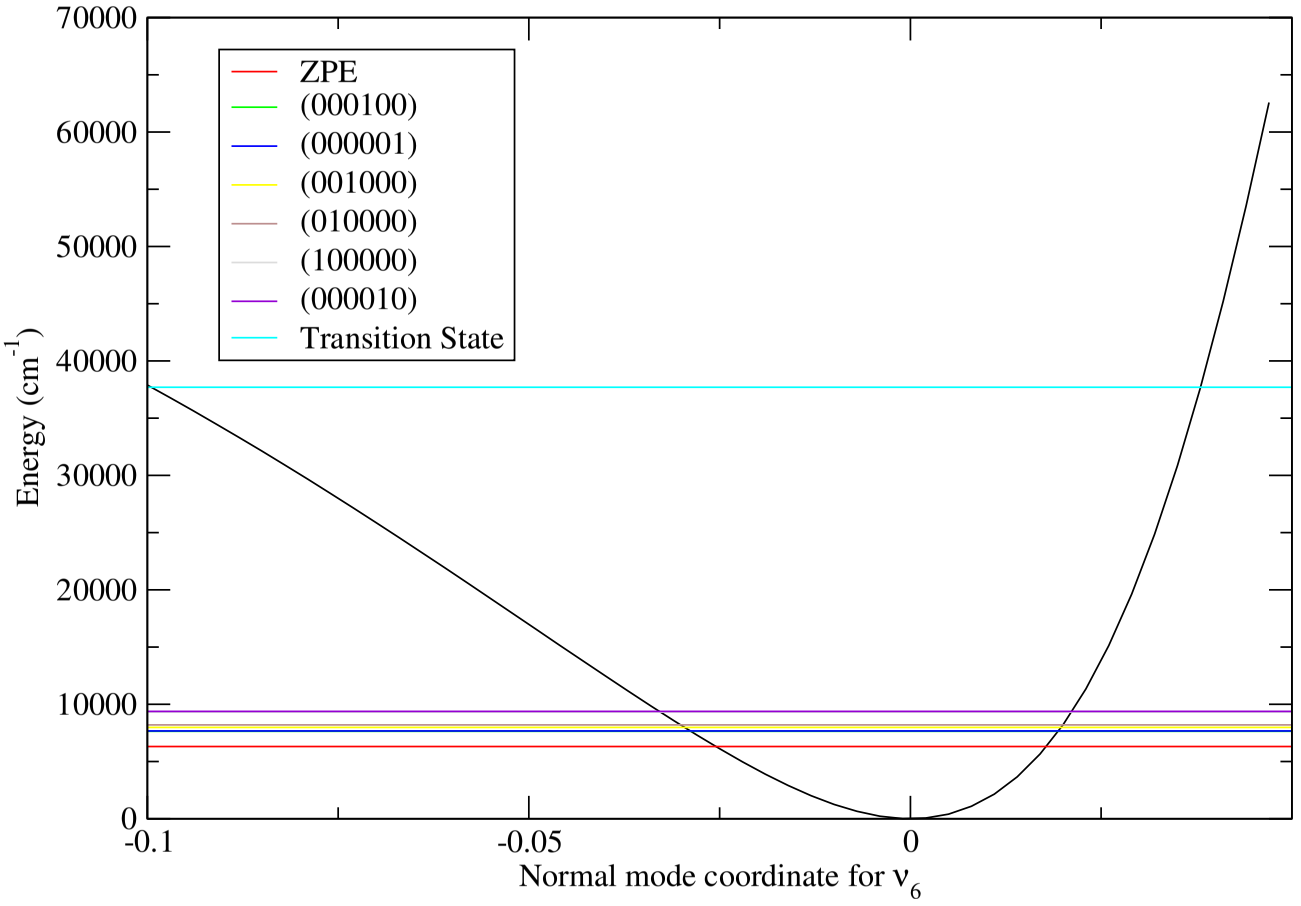

Figure 5.6: PES cut along the normal mode coordinate ν_6 of H_2CO. The horizontal lines represent the first few vibrational states calculated with VSCF/VCIPSI-PT2.

VSCF/VCIPSI-PT2 [64] is a variational quantum method for determining vibrational eigenstates of molecules. Similar to *electronic* variational methods (e.g., SCF and CI), these solve the vibrational Schrödinger equation. They have been shown to be successful in calculating eigenstates of molecules of 4 or more atoms (generally, the computational bottleneck begins here). Therefore, we consider their vibrational energies "exact" for our purposes. Clearly, the trajectories sample regions around these lowest vibrational states or very near the bottom of the potential. Sampling above this region where the curvature of the potential changes would lead to instabilities in the Herman-Kluk prefactor (Eq. 5.6). This is because the prefactor, which is imaginary, would be highly variable as the local frequencies along a curvature change region of the PES will change sign and/or become complex.

In Chapter 4, with a trajectory length of 244 fs and timestep of 0.5 fs, a total number of 488 gradient and Hessian calculations must be done. About 10,000 trajectories were used to calculate the correlation function. That amounts to about 5 million gradient and Hessian calculations. In these single-trajectory calculations, the trajectory length is 2.4 ps, with the same timestep size of 0.5 fs. So, while the trajectory is an order of magnitude longer, it is only a single calculation on a single processor (only 4880 gradients and Hessians). This is a drastic reduction of computational resources, taking about a day's worth of computational time on a single processor compared to a few weeks on a hundred processors. For each trajectory, we divide it into "segments" of correlation time (T_{corr}) of 0.3 ps length, which is a little over the period of the slowest vibrational mode. From this, we get the correlation function and determine the zero point energy, an equivalent procedure as done in Chapter 4 with full SC-IVR. For the strongest zero point signal, the reference wavefunction is kept at:

$$\Psi_{\text{ref}} = |\mathbf{p} = 0, \mathbf{q} = \mathbf{q}_{\text{eq}}\rangle, \tag{5.8}$$

which is the Gaussian approximation of the ground state. Fig. 5.7 shows results for

the zero point energy calculated with various single trajectories. Each trajectory was displaced by compressing along a normal mode coordinate ν_i, the amount corresponding to a desired total energy. Clearly, when the trajectory is stationary (total energy is zero), the ω_js in the HK prefactor are just the harmonic vibrational frequencies. Eq. 2.34 is the only contributing factor. The classical action is 1. The overlap is always 1, so the result is a correlation of a single frequency, namely the harmonic ZPE of exactly 6360 cm^{-1}. The next set of displacements considered were those where each mode is given the zero point energy of a single mode ($E = \frac{1}{2}\hbar\omega_j$). Fig. 5.7 shows these and also displacements up to the vibrational state energy (001000). To our knowledge, TA-SC-IVR simulations are completed at fairly low energy [131]. It can be seen in the HK prefactor (it contains a summation over the local vibrational frequencies) that staying low in the potential well is important. As an example, Fig. 5.8 shows a trajectory where $E = \frac{1}{2}\hbar\omega_4$ of potential energy was added along mode ν_4. All the frequencies (the six largest are assumed to be vibrational) are real. If one were to be near a transition state or saddle point, one or more frequencies would be imaginary and the Herman-Kluk prefactor would be highly unstable.

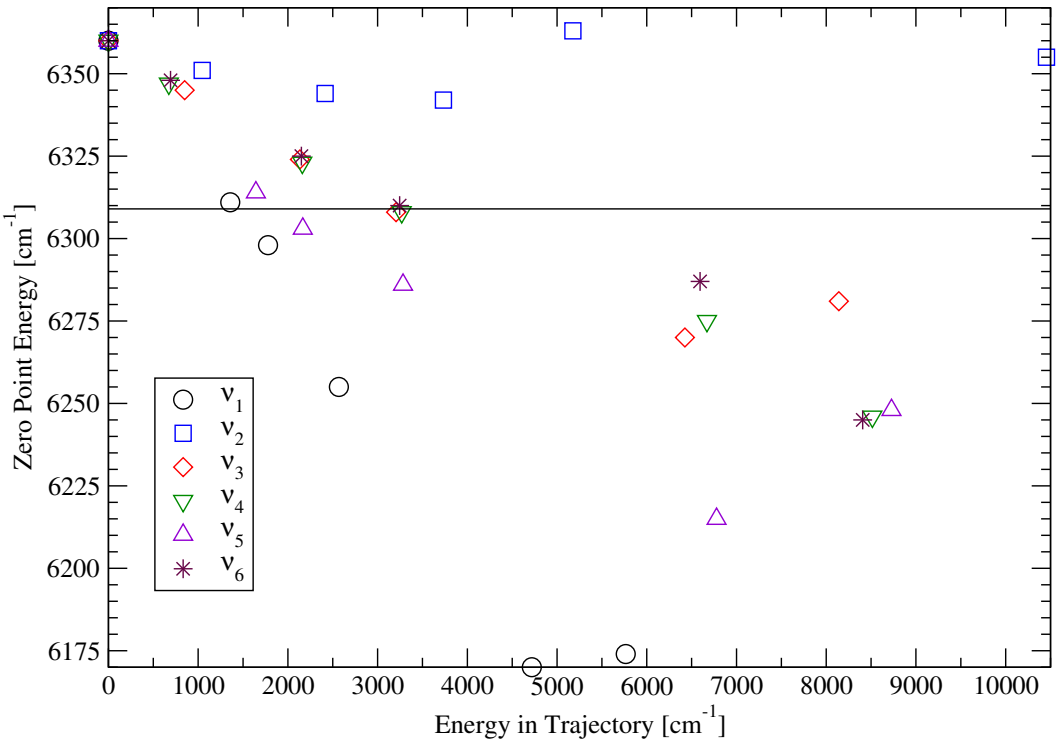

Figure 5.7: The zero point energy calculated with various single trajectories. Each trajectory was displaced along a particular normal mode coordinate equivalent to the energy on the x-axis. The horizontal line is the "exact" curvilinear-VSCF/VCIPSI-PT2 zero point energy.

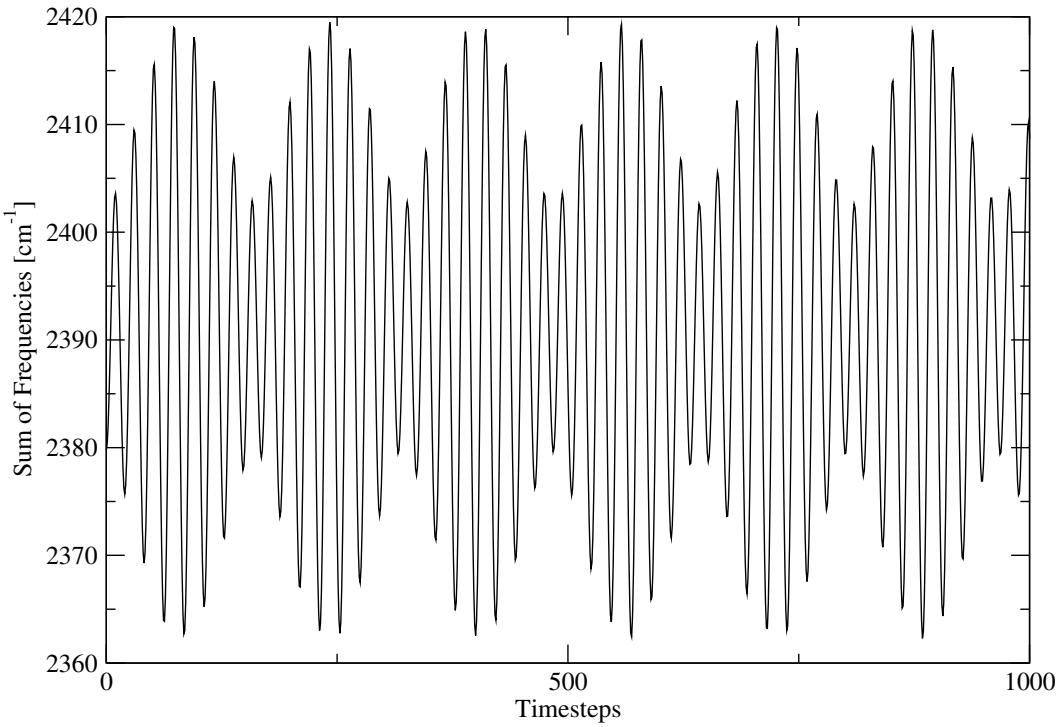

Figure 5.8: The summation of the local frequencies for a trajectory with $\frac{1}{2}\hbar\omega_4$ of energy in mode ν_4. In this case, all of the frequencies are real.

Going into more detail, the correlation function that is used in the Fourier transform consists of an average of 600 segments of 0.3 ps correlation length. This is similar to the averaging done in a multi-trajectory SC-IVR simulation. In this case, instead of separate trajectories, the segments come from the same single trajectory. The correlation function has both a real and imaginary part, and the two parts are shown in Fig. 5.9. The correlation function of this trajectory (same as that in Fig. 5.8) is highly periodic and of a single frequency. There is no loss of correlation, meaning there is little coupling of this mode, at least for this simulation length. The single frequency is due to the the coherent state of the trajectory strongly overlapping with the coherent state at the equilibrium geometry and no other states.

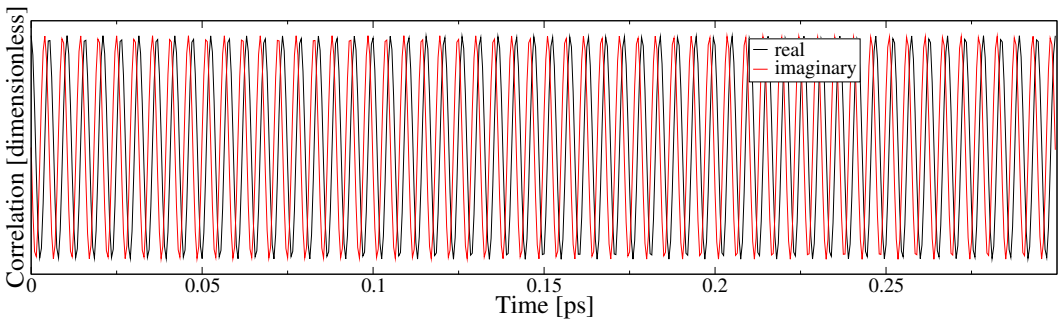

Figure 5.9: Correlation function of a single-trajectory SC-IVR calculation with a single quanta displacement in mode ν_4 and a reference wavefunction $|\mathbf{p} = 0, \mathbf{q} = \text{eq}\rangle$.

The power spectrum is obtained by a Fourier transform of the correlation function. Since the signal here does not decay, an exponential window function is applied:

$$W = \exp\left[-C\left(\frac{t}{T}\right)^2\right], \tag{5.9}$$

where C is a constant, t is time and T is the total length of the correlation function. This is because a Fourier transform by definition is an integration over the interval $(-\infty, \infty)$ so the signal needs to decay to zero by the integration limits. In cases where the trajectory is less harmonic and the reference wavefunction is not at equilibrium, the correlation does decay quite rapidly. The power spectrum of the above correlation function is shown in Fig. 5.10. It is highly-resolved and characteristic of time-averaged spectra. A similar result is found in the H_2CO simulations by Kaledin and Miller [62]. In their findings, the single-trajectory spectra are highly-peaked and narrow, while their full phase space spectra are relatively broad. This is due to - in their words - the "quenching" of the IVR integrand. However, they report the relative errors between the two methods and single time-averaged SC-IVR has a slightly higher error, with it increasing for higher vibrational states. It would seem logical that noise is quenched with repetitive data, yet because there are less data, results may not be as accurate.

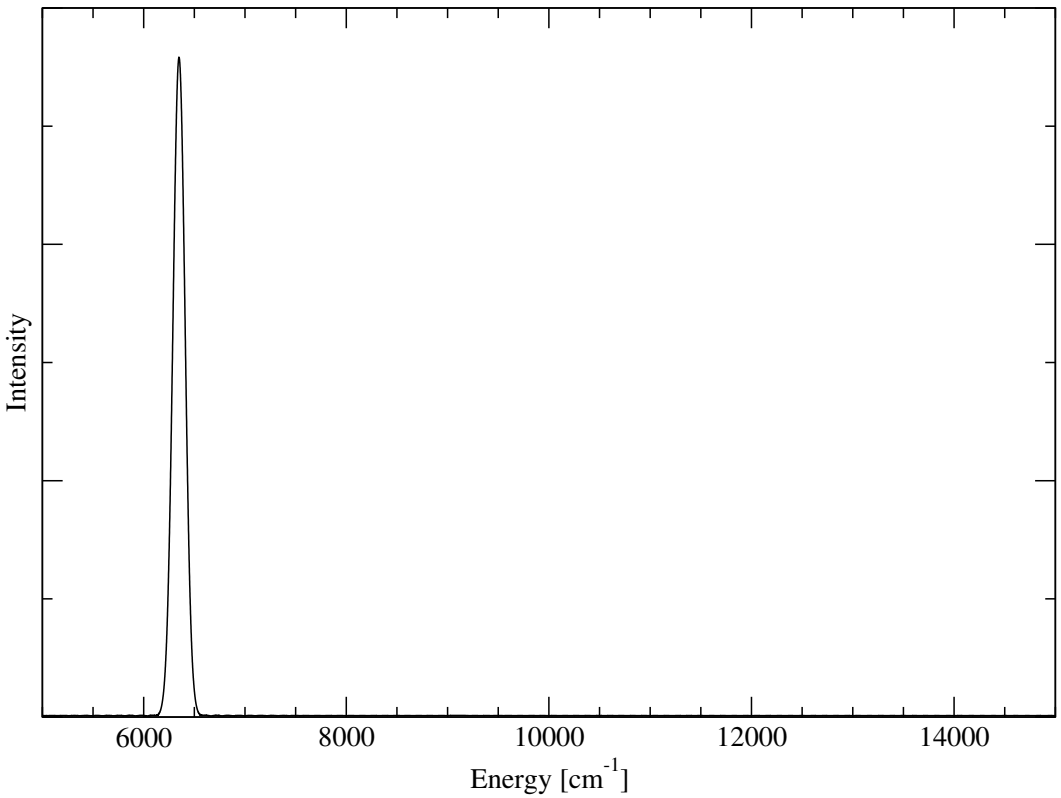

Figure 5.10: Power spectrum of a single-trajectory SC-IVR calculation with a single quanta displacement in mode ν_4 and a reference wavefunction $|\mathbf{p} = 0, \mathbf{q} = \text{eq}\rangle$. The spectrum shows the single highly-resolved ZPE peak.

Fig. 5.7 shows that the power spectra may be fairly dependent on the trajectory chosen. Within a particular mode displacement, there appears to be some trend, especially for displacement energies lower than the total zero point energy. For example, ν_2 remains relatively constant. The other modes have somewhat linear and decreasing trends, with ν_3, ν_4 and ν_6 being fairly similar. However, it is unclear why there is a turnaround at higher energies. More strikingly is that with increasing energies, the values become divergent. At around $x = 3250$ cm^{-1}, where 3 different displacements coincide, it is very near the "exact" zero point.

Ψ_{ref} may also be be chosen to extract states of higher energy. Analogous to the displacement of the Gaussian along normal modes in Chapter 4, we employed displaced reference wavefunctions and were able to easily extract the fundamentals

and first overtones. Fig. 5.11 shows power spectra where both the trajectories and reference wavefunctions were Gaussians displaced along a normal mode by an amount $E = \frac{1}{2}\hbar\omega_j$. As can be seen, all simulations were able to determine the zero point energy, with a similar discrepancy to that of Fig. 5.7. A trajectory with a displacement along ν_j with an equivalently-displaced Ψ_{ref} will produce peaks of the variety $(\cdots n \cdots)$. For instance, the first fundamental peak is (000100) from a trajectory and reference wavefunction of displacement along ν_4. These power spectra are much more resolved and easier for assignment compared to the standard SC-IVR spectra. Table 5.2 compiles all the SC-IVR vibrational state calculations in Chapter 4 with those of Chapter 5 (Figs. 5.7 and 5.11) as well as TA-SC-IVR of eight trajectories by Ceotto *et al.* [129], which is discussed in the next section. Ceotto undershoots the exact energies, which is of interest, as that means that method is finding more anharmonicity than the "exact" results. On the other hand, our single-trajectory SC-IVR energies are larger (closer to harmonic) than that of the standard SC-IVR.

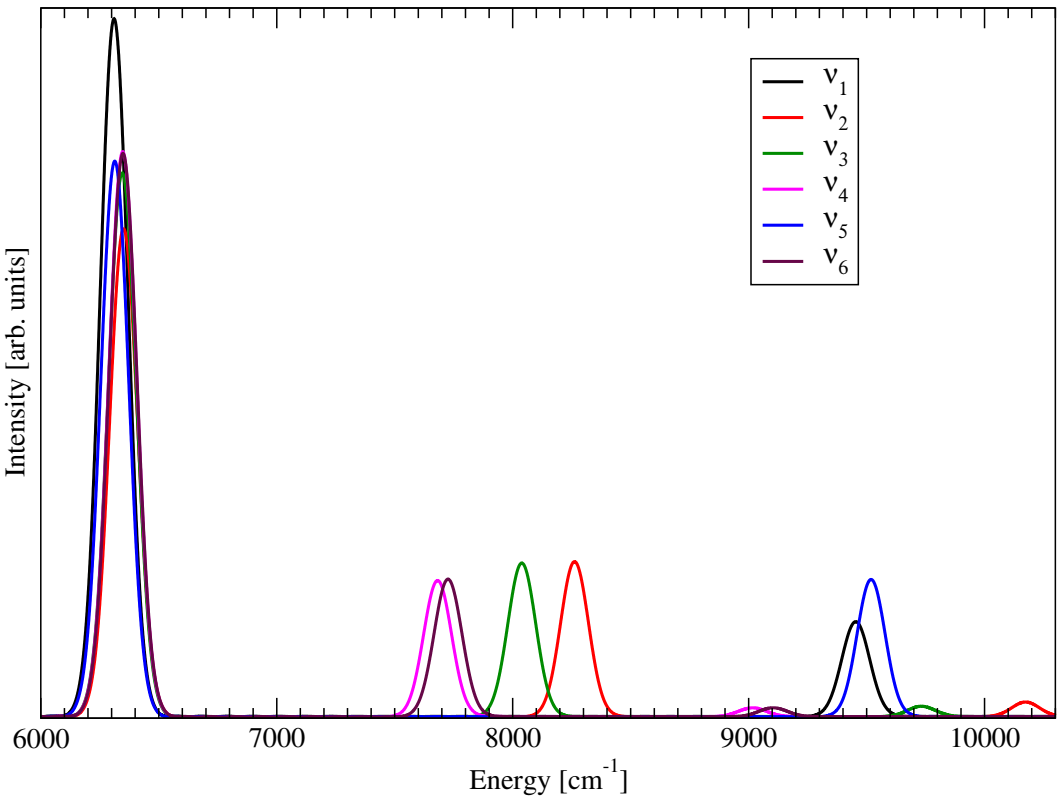

Figure 5.11: Power spectra of H_2CO determined by trajectory and reference wavefunction displacements along modes ν_j Each peak represents a single-mode excitation of the form $(\cdots n \cdots)$. Up to 2-quanta excitation is achieved from these particular trajectories.

Table 5.2: Fundamental and overtone vibrational state energies of H_2CO at the HF/3-21G level. Units are in cm^{-1}.

State	Harmonic	Exact [130]	SC-IVR [130]	TA(1)-SC-IVR	TA(8)-SC-IVR [129]
(000000)	6360	6309	6311	6336*	6258
(000100)	7697	7640	—	7682	—
(000001)	7738	7672	—	7726	—
(001000)	8053	7980	8013	8039	7911
(010000)	8276	8198	8208	8262	8152
(100000)	9522	9320	9303	9454	9300
(000010)	9593	9384	—	9519	—
(000200)	9034	8987	—	9018	—
(000002)	9117	9037	—	9103	—
(002000)	9745	9650	9587	9732	9598
(020000)	10191	10074	10089	10174	10020
(200000)	12685	12232	12297	12595	12352
(000020)	12827	12418	—	12724	—

5.3 Time-Averaging: Equivalent Ensembles?

The Monte Carlo estimate of the phase space as shown in Eq. 4.9 is a distribution centred upon a given position and momentum. This is a canonical distribution. While we account for this non-uniform sampling in Eq. 4.10, in a single-trajectory time-averaged SC-IVR, the canonical distribution is intrinsically eliminated. In fact, since segments $(\mathbf{p}_1, \mathbf{q}_1)$ are obtained from the single trajectory, the distribution actually sampled is microcanonical (that is, it is a constant energy ensemble). This becomes a concern for the integral in the correlation function. In the extreme limit where the integral over $(\mathbf{p}_0, \mathbf{q}_0)$ reduces to a single value, the phase space SC-IVR and time-averaged SC-IVR are not equivalent.

Thinking along that line, we look back at the original time-averaged SC-IVR equation (Eq. 5.5). Here, in addition to time-averaging, there is still the integral over phase space. If we take the (unaveraged) correlation functions from multiple single-trajectory calculations, which all have a different total energy, we conjecture that

we will recover some of the phase space average. In single-trajectory time-averaged SC-IVR, the "final" correlation function is an average of all the correlations in each segment. Each segment is a single NVE trajectory. Now, taking these correlations and *then* averaging them with other segments from a different (energy) trajectory, it would be an approximation to making a proper phase space average. It could provide a more accurate power spectrum (cf. Ref. [129]). We take the average of 6 different trajectories ($E = \frac{1}{2}\hbar\omega_j$ for each ν_j) and the result for the ZPE is 6336 cm^{-1}. Contrast this between the reference VSCF/VCIPSI-PT2 calculation (6309 cm^{-1}) and the full SC-IVR calculation (6311 cm^{-1}). It is between these results and the harmonic value. It is necessary to compare numerous single trajectories and see whether they produce consistent results or determine the outliers. Further investigation into whether a single-trajectory calculation is equivalent is warranted, as it is found in literature without much explanation.

Of recent interest [60, 103, 129, 130] has been the informed construction of the reference state. As said before, the correlation is highest when the coherent state of the trajectory is similar to that of the reference state. A reference state is a representation (guess) of the true wavefunction. So, when the reference wavefunction is a Gaussian at equilibrium, it represents the true ground state wavefunction, and a high overlap with this state will produce a strong signal for the ground vibrational state. Similarly, reference wavefunctions similar to the true wavefunction of other vibrational states will allow for the determination of those vibrational states in the power spectrum. Of course, all wavefunctions overlap in some manner with each other unless forbidden by symmetry. Generally, the issue with SC-IVR is the overlap with *too* many states, making for a very indeterminate spectrum. In Ref. [62], the reference state was expressed in a symmetry-adapted form. For H_2CO, there are four symmetric states: A_1, A_2, B_1 and B_2. In our previous study in Chapter 4, we used this concept (see Eq. 4.11) to extract states of A_1 symmetry. Most recently, Ceotto

et al. [60] reported a "multiple coherent" states method, where the reference state is of the form:

$$\Psi_{\text{ref}} = \sum_{i=1}^{states} |p^i q^i\rangle. \tag{5.10}$$

The "states" they consider are points on the $(p, 0)$ or $(0, q)$ phase space surface that are located at the peaks of the harmonic power spectrum. For maximum overlap, they also suggest using trajectories that are on the same phase space orbit. They state that the trajectories are "close to the modes associated with the desired vibrational energy peaks." This appears to mean imparting either momenta or displacement along all the normal modes with a total energy equal to that of the (harmonic) vibrational states. Therefore, multiples of quanta are imparted to each vibrational mode. Their results show that multiple trajectories (i.e., time-averaged SC-IVR not at the single-trajectory limit) produces energies that are more anharmonic than single-trajectory SC-IVR. In terms of their multiple coherent reference states, they are effective at producing a wide range of peaks yet they show that selecting reference states favouring a single vibrational state will produce more precise (higher, sharper peak) states. Using symmetric combinations of this multiple coherent state, choosing peaks with specific symmetries is possible as well. Another modification to the correlation function that they used (originally found in Ref. [61]) is the separable approximation. In this approximation, the HK prefactor is assumed to be separable. The prefactor contains two time variables (t_1 and t_2) and assuming it can be factored, would be of form:

$$R(t_1, t_2) \approx f(t_1)g(t_2). \tag{5.11}$$

It can be shown then, that one only needs to calculate the phase of R. The integrand becomes positive definite and improves the prefactor accuracy at long time. For H_2CO, they note that the separable approximation makes for a smoother power spectrum and does not affect peak location. While it is possible to implement, we have not found the need to use this approximation, given that we already use the

Johnson approximation of the prefactor.

From our results of the ZPE calculation, it is evident that the choice of trajectory affects the location of the ZPE. While the choice of reference state may affect the strength of the spectral density, it appears that the choice of trajectory may be critical for a single-trajectory calculation. For a very low energy trajectory, one seems to approach the harmonic zero point. Fig. 5.7 shows that as the energy of the trajectory increases, the calculated ZPE diverges. It would be useful to know the exact trajectories used in previous studies, whether the spectra are hand-picked from select trajectories or whether a single trajectory with significant spectral peaks was chosen. Further investigations into model systems would be beneficial. The higher vibrational states, when considered individually, give very resolved peaks, considerably easier to assign than for the standard SC-IVR calculation. If the location of the peaks can be reproduced with other trajectories, then the existing prescription is successful. If not, then the reason for the discrepancies due to trajectory choice will have to be examined.

The analysis of our implementation of the single-trajectory SC-IVR reveals that the approach is practical and can yield useful results with much reduced computational effort, providing a very efficient *ab initio* SC-IVR option.

Chapter 6

Conclusion and Future Outlook

6.1 Conclusions

The ultimate goal of theoretical chemistry is the ability to find solutions to describe nature at its most accurate, yet, as with all things, there is compromise. The real world is inherently quantum mechanical in nature, i.e., following the rules of quantum mechanics. The mathematics used to solve its equations are fairly simple. Yet, the solutions for most systems are computationally intractable. So, it is the job of the theoretical chemist to find ways to make these problems easier to solve. This involves creating an acceptable model for the molecular system and using a good approximation/representation of the Schrödinger equation. The former involves determining the subsystem of interest (or of importance) and the latter finding ways to circumvent the "brute force" method. One of the far-reaching areas of quantum dynamics is semiclassical dynamics. Semiclassical mechanics lies in between quantum and classical mechanics, in that it proceeds to solve the quantum mechanical equations in such a way that it takes information from classical mechanics. Specifically, we can utilize information from a classical (molecular dynamics) trajectory and use it in semiclassical forms of quantum mechanical equations in order to describe quantum mechanical effects, e.g., tunnelling, zero point energy, scattering, etc.

In this thesis, we have endeavoured to develop tools for and investigate problems

with the semiclassical initial value representation (SC-IVR). The first part of the work (Chapter 3) involved developing the ability to perform *ab initio* molecular dynamics in the software package MMTK. An interface between electronic structure programs (e.g., Molpro, GAMESS) and MMTK means that one can do on-the-fly molecular dynamics simulations in the simple and powerful framework of MMTK. With this tool established, we investigated the electronic ground and excited state dynamics of the CH_3OCl molecule. It is an important molecule in atmospheric chemistry and we have laid the groundwork for an intensive investigation into its photodissociation dynamics. Next, we began the primary focus of our research, which was creating a method to compute molecular vibrational state energies using the *ab initio* SC-IVR. With the tools developed in MMTK, we were able to conduct molecular dynamics simulations (and obtain second derivatives) which provided the classical inputs for our semiclassical algorithm (in Python, with some integration into the MMTK code), which is entirely in Cartesian coordinates. We determined the vibrational state energies of H_2CO and these were shown to be very accurate when compared to benchmark results (see Chapter 4). The final part of this thesis (Chapter 5) details similar calculations using *time-averaged* SC-IVR, a more computationally efficient technique. Our findings show that the energies obtained via this method are comparable to those obtained with full phase space SC-IVR.

6.1.1 *Ab initio* Molecular Dynamics

Methyl hypochlorite (CH_3OCl) has two low-lying electronic excited states from which the resulting dissociation products are known to contribute to the atmospheric chlorine cycle. Photoexcited CH_3OCl primarily goes into two dissociative excited states that produce the $Cl^{\cdot}$ radical. We have modelled the distribution of the ground state molecule which would be vertically excited into one of two excited states. Transition probabilities were computed from equilibrium and a preliminary excited

state analysis was done. The primary purpose of this study was to test the integration of *ab initio* dynamics in MMTK.

6.1.2 Semiclassical Initial-Value Representation of H_2CO

H_2CO is a well-studied molecule in terms of its vibrational states, including highly accurate PES surfaces [132]. Use of methods such as vibrational self-consistent field or vibrational configuration interaction to determine its vibrational energies including anharmonicity (for a certain electronic method/basis set) makes it a good system for observing the accuracy of vibrational states calculated using SC-IVR. With the *ab initio* tools established, we applied it to the SC-IVR technique and have reported on the numerous intricacies involved in such simulations (e.g., reference state selection). The fundamental, overtone and two-mode coupled vibrational states of H_2CO were determined. Finally, we examined the time-averaged variant of SC-IVR and performed similar calculations on the same system.

6.2 Future Outlook

6.2.1 Immediate Questions and Discussions

The immediate questions to be addressed are the validity and accuracy of time-averaged SC-IVR calculations. A full comparison of the results for standard SC-IVR with time-averaged SC-IVR calculations would be desired, and an analysis of whether any trends in the spectra with respect to trajectory selection should be done. As well, examining the use of a combination of reference states would be beneficial to see if any artifacts due to dynamics along a single mode remain. This could show whether the tradeoff between using single trajectories over multiple (time-averaged) trajectories is worth the extra scrutiny the single trajectory chosen must be. Choice of an inappropriate single trajectory may skew results. In fact, the exact prescription for each trajectory should be reported in any SC-IVR results.

Time-averaging over multiple trajectories has been shown to be more accurate [61] than single-trajectory SC-IVR. Unless the *ab initio* energy and Hessian evaluations are extremely computationally costly, there is most likely little reason not to use multiple-trajectory time-averaging.

In the meantime, it would be very beneficial to examine the phase space distribution between a full SC-IVR integral (NVT) and a time-averaged (NVE) integral. A weighting procedure of the trajectories similar to Eq. 4.10 would ensure the phase space distribution is uniform (i.e., a uniform grid). Then, the two methods would be mathematically equivalent. The simplest model is the 1-D harmonic oscillator (HO). Because the diagonalization of the Hessian for a harmonic system will just give the frequency of the HO, its power spectrum is actually analytic, and has been derived in Ref. [129]. Then, the most immediate models to investigate would be the single 1-D Morse oscillator, which is an ideal model system with actual anharmonicity. Ref. [129] has looked at uncoupled Morse oscillators. However, the determination of the equivalency of these systems with full phase space integrals is desired.

Other than work by Roy and co-workers [56–59, 114], the approximate Johnson WKB prefactor [54, 55] has not been used in the literature except for when it was originally proposed. Others have used the original prefactor and its alternate but equivalent form, the log-derivative. To that end, we have started implementing the log-derivative form for the 1-D models. Any discrepancies between that and the WKB approximation can then be precisely identified.

6.2.2 Ultimate Aim

Ultimately, SC-IVR would show its power not through small systems, but through large and/or strongly anharmonic systems such as small clusters, complexes in water or proteins. Surface chemistry using SC-IVR is also possible [133]. Smaller systems can already be analyzed relatively computationally efficiently using vibrational SCF

methods. So, ways to improve SC-IVR to be more advantageous than these methods would be of immediate interest to examine. Ensuring that, notwithstanding SC-IVR's natural slow convergence [134], these chemically-interesting systems can be accessible. We know that despite increasing degrees of freedom, SC-IVR can take advantage of using geometric constraints [56]. Then, for example, parts of a system (say, an amino acid of interest in a protein, or the active region of proton transfer) may treated with all degrees of freedom while the "unimportant" parts may be constrained. Geometric constraints in MTTK is a straightforward process. SC-IVR also requires the Hessian in this limited degree of freedom frame, so employing projection techniques is necessary [56]. Also, it would be worth to take advantage of some of the force fields that are natively built into MMTK. A force field such as AMBER [135] has many atomic parameters for bio-molecular systems readily usable in MMTK.

Another way to realize the full potential of SC-IVR is to reduce the number of Hessian calculations. The improvement of integrators through the use of Hessians is not new [136, 137]. However, bringing Hessians into an integrator (we only use gradient data in Velocity-Verlet, for example) means those calculations have to be efficient or sparse. Bringing this idea into SC-IVR would be highly-desirable, as Hessian information is already required. Barring efficiencies in the integrator algorithm that would make the number of timesteps more sparse, there is the technique called *Hessian updating* [105, 138], where while the dynamics integration timestep doesn't change, the need for a Hessian at each timestep is not necessary. For example, compact finite difference schemes are stepwise ways to determine the Hessian using other data (e.g., gradients). Therefore, a "true" Hessian is only obtained after a few timesteps, while the interim points are numerically obtained through an updating scheme. Ceotto and co-workers have shown that *ab initio* MD calculations can be two orders of magnitude more efficient [138]. He and other co-workers applied this

scheme to *ab initio* time-averaged SC-IVR on the CO_2 molecule. As the number of timesteps before a real Hessian calculation increases, the accuracy of the power spectrum remains surprisingly good. Only after about 20 steps of approximate Hessians does the spectra start to show a significant degradation in the lower-intensity peaks. This is encouraging news for studying larger systems.

6.3 Other Applications of SC-IVR

Vibrational states are only a single type of information which can be obtained from SC-IVR. In fact, SC-IVR has been used to determine a variety of molecular information. The quantum propagator is the root of many quantum-mechanical equations, so having a semiclassical propagator allows for an analysis of other properties provided the observable (or eigenstate) can be expressed in semiclassical variables. For instance, we have referred to the survival amplitude $C(t)$ as the "correlation" function. In several applications, one is interested in studying the effects of temperature, T, on the correlation between two physical quantities, A and B, for a system with Hamiltonian $\hat{H}$. This is achieved by computing the so-called canonical time correlation function defined as [139]:

$$\langle AB(t)\rangle = \frac{1}{Z}\text{Tr}\left\{e^{-\beta\hat{H}}\hat{A}\hat{B}(t)\right\}, \tag{6.1}$$

where $\beta = 1/(k_B T)$, k_B is Boltzmann's constant, and $Z = \text{Tr}\left\{\exp(-\beta\hat{H})\right\}$ is the canonical partition function of the system. Note that the $\hat{B}(t)$ represents the time dependence of the operator $\hat{B}$. More specifically,

$$\hat{B}(t) = e^{i\hat{H}t/\hbar}\hat{B}e^{-i\hat{H}t/\hbar} \tag{6.2}$$

is the Heisenberg representation of the operator $\hat{B}$ and defines the time dependence. Note that both the forward and backward propagators appear in the definition of $\hat{B}(t)$. This means that in a SC-IVR implementation, two sets of integrals over phase space

must be inserted. This can lead to serious sampling issues and various approximate methods have been developed to overcome these problems [140].

There are a variety of problems that can benefit from our SC-IVR for vibrational states. Most related to vibrational states would be the determination of vibrational eigenfunctions. Ceotto *et al.* [104] have determined the eigenstates of H_2CO with an equation very similar to that of the survival amplitude. Quantum thermal correlation functions such as vibrational relaxation [115] can be studied. Vibronic transitions of H_2CO [102] via *ab initio* SC-IVR have also been investigated.

Overall, *ab initio* semiclassical techniques are promising and have been shown to be another effective tool in the arsenal of a quantum dynamicist.

Bibliography

[1] J. S. Francisco, *International Journal of Quantum Chemistry* **73** 29 (1999).

[2] D. A. McQuarrie and J. D. Simon, *Physical Chemistry: A Molecular Approach*, University Science Books, Sausalito, CA (1997).

[3] Rayleigh, Baron (J. W. Strutt), *Nature* **72** 54 (1975).

[4] A. Einstein, *Ann. Phys. (Berlin)* **17** 132 (1905).

[5] C. J. Cramer, *Essentials of Computational Chemistry: Theories and Models*, Wiley, West Sussex (2004).

[6] T. Helgaker, P. Jørgensen, and J. Olsen, *Molecular Electronic-Structure Theory*, Wiley, West Sussex (2000).

[7] J. K. Cullum and R. A. Willoughby, *Lanczos Algorithms for Large Symmetric Eigenvalue Computations*, Birkhäuser, Boston (1985).

[8] W. H. Miller, *Proc. Natl. Acad. Sci.* **102** 6660 (2005).

[9] B. Balzer, S. Dilthey, G. Stocka, and M. Thoss, *J. Chem. Phys.* **119** 5795 (2003).

[10] R. P. Feynman and A. R. Hibbs, *Quantum Mechanics and Path Integrals*, McGraw-Hill, New York (1965).

[11] K. G. Kay, *J. Chem. Phys.* **100** 4377 (1994).

[12] H.-W. Lee and M. O. Scully, *J. Chem. Phys.* **73** 2238 (1980).

[13] F. Jensen, *Introduction to Computational Chemistry, 2nd Ed.*, Wiley, West Sussex (2007).

[14] C. C. J. Roothaan, *Rev. Mod. Phys.* **23** 69 (1951).

[15] P. Hohenberg and W. Kohn, *Phys. Rev.* **B136** 864 (1964).

[16] W. Kohn and L. J. Sham, *Phys. Rev.* **A140** 1133 (1965).

[17] M. W. Schmidt, K. K. Baldridge, J. A. Boatz, S. T. Elbert, M. S. Gordon, J. H. Jensen, S. Koseki, N. Matsunaga, K. A. Nguyen, S. J. Su, T. L. Windus, M. Dupuis, and J. A. Montgomery, *J. Comput. Chem.* **14** 1347 (1993).

[18] H.-J. Werner, P. J. Knowles, R. Lindh, F. R. Manby, M. Schütz, P. Celani, T. Korona, G. Rauhut, R. D. Amos, A. Bernhardsson, A. Berning, D. L. Cooper, M. J. O. Deegan, A. J. Dobbyn, F. Eckert, C. Hampel, G. Hetzer, A. W. Lloyd, S. J. McNicholas, W. Meyer, M. E. Mura, A. Nicklass, P. Palmieri, R. Pitzer, U. Schumann, H. Stoll, A. J. Stone, R. Tarroni, and T. Thorsteinsson, Molpro, version 2006.1, a package of ab initio programs (2006), see http://www.molpro.net.

[19] M. J. Frisch, G. W. Trucks, H. B. Schlegel, G. E. Scuseria, M. A. Robb, J. R. Cheeseman, G. Scalmani, V. Barone, B. Mennucci, G. A. Petersson, H. Nakatsuji, M. Caricato, X. Li, H. P. Hratchian, A. F. Izmaylov, J. Bloino, G. Zheng, J. L. Sonnenberg, M. Hada, M. Ehara, K. Toyota, R. Fukuda, J. Hasegawa, M. Ishida, T. Nakajima, Y. Honda, O. Kitao, H. Nakai, T. Vreven, J. A. Montgomery, Jr., J. E. Peralta, F. Ogliaro, M. Bearpark, J. J. Heyd, E. Brothers, K. N. Kudin, V. N. Staroverov, R. Kobayashi, J. Normand, K. Raghavachari, A. Rendell, J. C. Burant, S. S. Iyengar, J. Tomasi, M. Cossi, N. Rega, J. M. Millam, M. Klene, J. E. Knox, J. B. Cross, V. Bakken, C. Adamo, J. Jaramillo, R. Gomperts, R. E. Stratmann, O. Yazyev, A. J. Austin, R. Cammi, C. Pomelli, J. W. Ochterski, R. L. Martin, K. Morokuma, V. G. Zakrzewski, G. A. Voth, P. Salvador, J. J. Dannenberg, S. Dapprich, A. D. Daniels, . Farkas, J. B. Foresman, J. V. Ortiz, J. Cioslowski, and D. J. Fox, Gaussian 09 Revision A.1, Gaussian Inc. Wallingford CT 2009.

[20] TURBOMOLE V6.3 2011, a development of University of Karlsruhe and Forschungszentrum Karlsruhe GmbH, 1989-2007, TURBOMOLE GmbH, since 2007; available from http://www.turbomole.com.

[21] P. Atkins and R. Friedman, *Molecular Quantum Mechanics, 5th Ed.*, OUP, Oxford (2011).

[22] D. J. Tannor, *Introduction to Quantum Mechanics - A Time-Dependent Perspective*, University Science Books, Sausalito, California (2007).

[23] B. M. Austin, D. Y. Zubarev, and W. A. Lester, Jr., *Chem. Rev.* **112** 263 (2012).

[24] J. B. Anderson, *J. Chem. Phys.* **63** 1499 (1975).

[25] D. C. Clary, D. M. Benoit, and T. van Mourik, *Acc. Chem. Res.* **33** 441 (2000).

[26] P. J. Reynolds, D. M. Ceperley, B. J. Adler, and W. A. Lester, *J. Chem. Phys.* **77** 5593 (1982).

[27] H.-D. Meyer, F. Gatti, and G. A. Worth, *Multidimensional Quantum Dynamics: MCTDH Theory and Applications*, Wiley-VCH, Weinheim (2009).

[28] P. R. Holland, *The Quantum Theory of Motion*, Cambridge University Press, Cambridge (1993).

[29] M. Brack and R. K. Bhaduri, *Semiclassical Physics*, Addison-Wesley, Don Mills, Ontario (1997).

[30] W. C. Swope, H. C. Andersen, P. H. Berens, and K. R. Wilson, *J. Chem. Phys.* **76** 637 (1982).

[31] D. A. Case, T. E. Cheatham, III, T. Darden, H. Gohlke, R. Luo, K. M. Merz, Jr., A. Onufriev, C. Simmerling, B. Wang, and R. Woods, *J. Comput. Chem.* **26** 1668 (2005).

[32] H. J. C. Berendsen, D. Van Der Spoel, and R. Van Drunen, *Comp. Phys. Comm.* **91** 43 (1995).

[33] W. Smith, T. R. Forester, and I. T. Todorov, *The DLPOLY Classic User Manual*, Daresbury Laboratory, Cheshire, UK (2010).

[34] W. L. Jorgensen, J. Chandrasekhar, J. D. Madura, R. W. Impey, and M. L. Klein, *J. Chem. Phys.* **79** 926 (1983).

[35] B. R. Brooks, R. E. Bruccoleri, B. D. Olafson, D. J. States, S. Swaminathan, and M. Karplus, *J. Comput. Chem.* **4** 187 (1983).

[36] P. Cvitanović, R. Artuso, R. Mainieri, G. Tanner, and G. Vattay, *Chaos: Classical and Quantum*, Niels Bohr Institute, Copenhagen (2010), ChaosBook.org.

[37] J. H. van Vleck, *Proc. Nat. Acad. Sci.* **14** 178 (1928).

[38] M. C. Gutzwiller, *J. Math. Phys.* **8** 1979 (1967).

[39] M. F. Herman and E. Kluk, *Chem. Phys.* **91** 27 (1984).

[40] M. F. Herman, *Annu. Rev. Phys. Chem.* **45** 83 (1994).

[41] E. J. Heller, *J. Chem. Phys.* **94** 2723 (1991).

[42] W. H. Miller, *J. Chem. Phys.* **95** 9428 (1991).

[43] E. J. Heller, *J. Chem. Phys.* **75** 2923 (1981).

[44] C. Cohen-Tannoudji, B. Diu, and F. Laloë, *Quantum Mechanics*, John Wiley & Sons and Hermann, Paris (1977).

[45] W. H. Miller, *J. Phys. Chem. A* **105** 2942 (2001).

[46] W. H Miller, *Mol. Phys.* **100** 397 (2002).

[47] S. A. Deshpande and G. S. Ezra, *J. Phys. A* **39** 5067 (2006).

[48] K. G. Kay, *Chem. Phys.* **322** 3 (2006).

[49] E. J. Heller, *Acc. Chem. Res.* **39** 127 (2006).

[50] E. J. Heller, *J. Chem. Phys.* **62** 1544 (1975).

[51] R. J. Glauber, *Phys. Rev.* **130** 2529 (1963).

[52] Y. Li and J. S. Francisco, *J. Chem. Phys.* **111** 8384 (1999).

[53] J. N. Crowley, F. Helleis, R. Müller, G. K. Moortgat, and P. J. Crutzen, *J. Geophys. Res* **99** 20683 (1994).

[54] R. Gelabert, X. Giménez, M. Thoss, H. Wang, and W. H. Miller, *J. Phys. Chem. A* **104** 10321 (2000).

[55] B. R. Johnson, *Chem. Phys.* **381** 1973 (1973).

[56] B. B. Issack and P.-N. Roy, *J. Chem. Phys.* **123** 84103 (2005).

[57] B. B. Issack and P.-N. Roy, *J. Chem. Phys.* **126** 24111 (2007).

[58] B. B. Issack and P.-N. Roy, *J. Chem. Phys.* **127** 054105 (2007).

[59] B. B. Issack and P.-N. Roy, *J. Chem. Phys.* **127** 144306 (2007).

[60] M. Ceotto, S. Atahan, G. F. Tantardini, and A. Aspuru-Guzik, *J. Chem. Phys.* **130** 234113 (2009).

[61] A. L. Kaledin and W. H. Miller, *J. Chem. Phys.* **118** 7174 (2003).

[62] A. L. Kaledin and W. H. Miller, *J. Chem. Phys.* **119** 3078 (2003).

[63] Y. Scribano and D. M. Benoit, *Chem. Phys. Lett.* **458** 384 (2008).

[64] Y. Scribano, D. M. Lauvergnat, and D. M. Benoit, *J. Chem. Phys.* **133** 94103 (2010).

[65] G. C. Carney, L. L. Sprandel, and C. W. Kern, *Adv. Chem. Phys.* **37** 305 (1978).

[66] J. M. Bowman, *J. Chem. Phys.* **68** 608 (1978).

[67] K. Yagi, K. Hirao, T. Taketsugu, M. W. Schmidt, and M. S. Gordon, *J. Chem. Phys.* **121** 1383 (2004).

[68] G. M. Chaban, J. O. Jung, and R. B. Gerber, *J. Chem. Phys.* **111** 1823 (1999).

[69] J. M. Bowman, K. M. Christoffel, and F. L. Tobin, *J. Phys. Chem.* **83** 905 (1979).

[70] K. M. Christoffel and J. M. Bowman, *Chem. Phys. Lett.* **85** 220 (1982).

[71] S. Carter, J. M. Bowman, and N. C. Handy, *Theor. Chem. Acc.* **100** 191 (1998).

[72] E. R. Davidson, *J. Comput. Phys.* **17** 87 (1975).

[73] E. R. Davidson, *Comp. Phys. Commun.* **53** 49 (1989).

[74] C. W. Murray, S. C. Racine, and E. R. Davidson, *J. Comput. Phys.* **103** 382 (1992).

[75] K. Hinsen, *J. Comput. Chem.* **21** 79 (2000).

[76] T. P. W. Jungkamp, U. Kirchner, M. Schmidt, and R. N. Schindler, *J. Photochem. Photobiol. A* **91** 1 (1995).

[77] S. Nanbu and S. Iwata, *J. Phys. Chem.* **96** 2103 (1992).

[78] M. J. Krisch, L. R. McCunn, K. Takematsu, L. J. Butler, F. R. Blase, and J. Shu, *J. Phys. Chem. A* **108** 1650 (2004).

[79] R. N. Schindler, M. Liesner, S. Schmidt, U. Kirchner, and T. Benter, *J. Photochem. Photobiol. A* **107** 9 (1997).

[80] M. Mühlhäuser, M. Schnell, and S. D. Peyerimhoff, *Mol. Phys.* **100** 509 (2002).

[81] E. Drougas, A. M. Kosmas, M. Schnell, M. Mühlhäuser, and S. D. Peyerimhoff, *Mol. Phys.* **100** 2653 (2002).

[82] T. J. He, D. M. Chen, F. C. Liu, and L. S. Sheng, *Chem. Phys. Lett.* **332** 545 (2000).

[83] D. Jung, C. J. Chen, and J. W. Bozzelli, *J. Phys. Chem. A* **104** 9581 (2000).

[84] J. S. Rigden and S. S. Butcher, *J. Chem. Phys.* **40** 2109 (1964).

[85] T. H. Dunning, *J. Chem. Phys.* **90** 1007 (1989).

[86] D. E. Woon and T. H. Dunning, *J. Chem. Phys.* **98** 1358 (1993).

[87] R. A. Kendall, T. H. Dunning, and R. J. Harrison, *J. Chem. Phys.* **96** 6796 (1992).

[88] H.-J. Werner and P. J. Knowles, *J. Chem. Phys.* **82** 5053 (1985).

[89] P. J. Knowles and H.-J. Werner, *Chem. Phys. Letters* **115** 259 (1985).

[90] H.-J. Werner and W. Meyer, *J. Chem. Phys.* **74** 5794 (1981).

[91] H.-J. Werner and P. J. Knowles, *J. Chem. Phys.* **89** 5803 (1988).

[92] P. J. Knowles and H.-J. Werner, *Chem. Phys. Lett.* **145** 514 (1988).

[93] E. R. Davidson and D. W. Silver, *Chem. Phys. Lett.* **52** 403 (1977).

[94] W. J. Hehre, R. Ditchfield, and J. A. Pople, *J. Chem. Phys.* **56** 2257 (1972).

[95] M. M. Francl, W. J. Pietro, W. J. Hehre, J. J. Binkley, M. S. Gordon, D. J. Defrees, and J. A. Pople, *J. Chem. Phys.* **77** 3654 (1982).

[96] P. C. Harihara and J. A. Pople, *Theor. Chim. Acta* **28** 213 (1973).

[97] T. Clark, J. Chandrasekhar, G. W. Spitznagel, and P. V. Schleyer, *J. Comp. Chem.* **4** 294 (1983).

[98] S. Nosé, *Mol. Phys.* **52** 255 (1984).

[99] M. Thoss and H. Wang, *Annu. Rev. Phys. Chem.* **55** 299 (2004).

[100] K. G. Kay, *Annu. Rev. Phys. Chem.* **56** 255 (2005).

[101] W. H. Miller, *J. Chem. Phys.* **125** 132305 (2006).

[102] J. Tatchen and E. Pollak, *J. Chem. Phys.* **130** 041103 (2009).

[103] M. Ceotto, S. Atahan, S. Shim, G. F. Tantardini, and A. Aspuru-Guzik, *Phys. Chem. Chem. Phys.* **11** 3861 (2009).

[104] M. Ceotto, S. Valleau, G. F. Tantardini, and A. Aspuru-Guzik, *J. Chem. Phys.* **134** 234103 (2011).

[105] M. Ceotto, Y. Zhuang, and W. L. Hase, *J. Chem. Phys.* **138** 054116 (2013).

[106] H.-D. Meyer, U. Manthe, and L. S. Cederbaum, *Chem. Phys. Lett.* **165** 73 (1990).

[107] J. M. Bowman, T. Carrington, and H.-D. Meyer, *Mol. Phys.* **106** 2145 (2008).

[108] J. M. Bowman, S. Carter, and X. Huang, *Int. Rev. Phys. Chem.* **22** 533 (2003).

[109] D. M. Ceperley and B. J. Adler, *J. Chem. Phys.* **81** 5833 (1984).

[110] I. R. Craig and D. E. Manolopoulos, *J. Chem. Phys.* **121** 3368 (2004).

[111] W. H. Miller, *J. Chem. Phys.* **53** 3578 (1970).

[112] X. Sun and W. H. Miller, *J. Chem. Phys.* **110** 6635 (1999).

[113] W. H. Miller, *J. Phys. Chem. A* **113** 1405 (2009).

[114] B. B. Harland and P.-N. Roy, *J. Chem. Phys.* **118** 4791 (2003).

[115] J. M. Moix and E. Pollak, *J. Chem. Phys.* **129** 064515 (2008).

[116] G. Tao and W. H. Miller, *J. Chem. Phys.* **130** 184108 (2009).

[117] N. Makri and W. H. Miller, *J. Chem. Phys.* **116** 9207 (2002).

[118] E. Bukhman and N. Makri, *J. Phys. Chem. A* **111** 11320 (2007).

[119] X. Sun and W. H. Miller, *J. Chem. Phys.* **108** 8870 (1998).

[120] M. Ovchinnikov, V. A. Apkarian, and G. A. Voth, *J. Chem. Phys.* **114** 7130 (2001).

[121] R Ianconescu and E. Pollak, *J. Chem. Phys.* **134** 234305 (2011).

[122] Y. Tawada, T. Tsuneda, S. Yanagisawa, Y. Yanai, and K. Hirao, *J. Chem. Phys.* **120** 8425 (2004).

[123] J. P. Perdew, K. Burke, and M. Ernzerhof, *Phys. Rev. Lett.* **77** 3865 (1996).

[124] J. O. Jung and R. B. Gerber, *J. Chem. Phys.* **105** 10332 (1996).

[125] L. Pele, B. Brauer, and R. B. Gerber, *Theo. Chem. Acc.* **117** 69 (2007).

[126] J. S. Binkley, J. A. Pople, and W. J. Hehre, *J. Am. Chem. Soc.* **102** 939 (1980).

[127] G. H. Peslherbe and W. L. Hase, *J. Chem. Phys.* **104** 7882 (1996).

[128] Y. Elran and K. G. Kay, *J. Chem. Phys.* **110** 8912 (1999).

[129] M. Ceotto, G. F. Tantardini, and A. Aspuru-Guzik, *J. Chem. Phys.* **135** 214108 (2011).

[130] S. Y. Y. Wong, D. M. Benoit, M. Lewerenz, A. Brown, and P.-N. Roy, *J. Chem. Phys.* **134** 094110 (2011).

[131] Private correspondence with M. Ceotto.

[132] K. Yagi, C. Oyanagi, T. Taketsugu, and K. Hirao, *J. Chem. Phys.* **118** 1653 (2003).

[133] M. Ceotto, D. Dell'Angelo, and G. F. Tantardini, *J. Chem. Phys.* **133** 054701 (2010).

[134] J. C. Burant and V. Batista, *J. Chem. Phys.* **116** 2748 (2002).

[135] R. Salomon-Ferrer, D. A. Case, and R. C. Walker, *WIREs Comput. Mol. Sci.* **3** 198 (2013).

[136] U. Lourderaj, K. Song, T. L. Windus, Y. Zhuang, and W. L. Hase, *J. Chem. Phys.* **126** 044105 (2007).

[137] J. M. Millam, V. Bakken, W. Chen, W. L. Hase, and H. B. Schlegel, *J. Chem. Phys.* **111** 3800 (1999).

[138] Y. Zhuang, M. R. Siebert, W. L. Hase, K. G. Kay, and M. Ceotto, *J. Chem. Theo. Comp.* **9** 54 (2013).

[139] D. A. McQuarrie, *Statistical Mechanics*, University Science Books, Sausalito, CA (2000).

[140] N. Makri and K. Thompson, *Chem. Phys. Lett.* **291** 101 (1998).

Appendix A

van Vleck's Semiclassical Propagator

The propagator is assumed to be in this general form:

$$e^{-i\hat{H}t/\hbar} \equiv A(x, x', dt)e^{\frac{i}{\hbar}S(x,x',\delta t)}. \tag{A.1}$$

S is now the time-dependent form of the action (integral of Lagrangian) as found in the Hamilton-Jacobi equation. Through some algebra, one gets:

$$e^{-i\hat{H}t/\hbar} \approx \left(\frac{m}{2\pi i\hbar\delta t}\right)^{3N/2} e^{\frac{i}{\hbar}\left(\frac{m(q-q\prime)^2}{2\delta t}-V(q)\delta t\right)}. \tag{A.2}$$

As can be seen, the amplitude and phase are entirely classical quantities. Van Vleck's final form is:

$$e^{-i\hat{H}t/\hbar} = \sum_{\text{roots}} \int dx_f \int dx_i \Psi_f^*(x_2)\Psi_i(x_1) \left[(2\pi i\hbar)^{3N} \left|\frac{\partial x_2}{\partial p_1}\right|\right]^{-1/2} e^{iS_t(x_2,x_1)/\hbar}. \tag{A.3}$$

In terms of an initial value representation, it can be written as

$$e^{i\hat{H}t/\hbar} = \int d\mathbf{x}_0 \int d\mathbf{p}_0 \left[\left|\frac{\partial \mathbf{x}_t(\mathbf{x}_0,\mathbf{p}_0)}{\partial \mathbf{p}_0}\right| /(2\pi i\hbar)^{3N}\right]^{1/2} e^{iS_t(\mathbf{x}_0,\mathbf{p}_0)/\hbar} |\mathbf{x}_t\rangle\langle\mathbf{x}_0|. \tag{A.4}$$

This form has also been rederived by Gutzwiller [38].

Appendix B

Electronic Structure Methods Used - Overview

Further information about electronic structure methods may be found in Refs. [5, 6, 13].

B.1 Hartree-Fock

The simplest electronic structure method used in this work is the Hartree-Fock (HF) method [14]. Molecular orbitals (MOs) are expressed as linear combinations of atomic orbitals. For each molecular orbital, the coefficients are determined through a self-consistent field procedure. These molecular orbitals linear combinations are a result of a single Slater determinant (single configuration). The product of these single-particle orbitals make up the total wavefunction. HF is approximate at best for determining the ground state of a molecule but it can be a first step for the application of more complex electronic structure methods.

B.2 Density Functional Theory

Density Functional Theory (DFT) [15, 16], instead of working with the electronic coordinates directly, uses a functional of the electron density. It includes some electron correlation (missing in HF). Like HF, it is an independent-particle model so scales in time similarly to it.

B.3 Configuration Interaction

The HF method is a starting point for many investigations and its self-consistent field orbitals are used as a basis for advanced methods. Most systems consist of electronic states that are a combination of a number of configuration states. Instead of solely occupying the lowest MOs, the virtual orbitals may also be populated. Each configuration is represented by a determinant. The total wavefunction is a summation of all these excited Slater determinants; in the case of an infinite number of excitations, it is called a full CI (configuration interaction).

B.4 Complete Active Space Self-Consistent Field

In addition to determining the wavefunction coefficients, each MO may be optimized. This becomes a huge computational effort, so the MOs are split into *active* and *inactive* types. The active space generally contains the upper occupied orbitals and lower unoccupied orbitals where excitations occur to/from. This restricts the total number of configuration state functions involved in the calculation. The active space, taken from an HF reference calculation, is chosen as small as possible while ensuring an accurate description of the system. If multiple states are optimized in the CASSCF at the same time, it is state-averaged [90].

B.5 Multi-Reference Configuration Interaction

If the reference wavefunction does not come from a HF calculation but rather from CASSCF, then the configuration state functions are generated from these orbitals (multiple determinants). Because of the number of configurations generated, the choice of which functions to include into calculations is also important.